AN ABSTRACT OF THE DISSERTATION OF

Reina Nakamura for the degree of Doctor of Philosophy in Atmospheric Sciences presented on February 4, 2005.

Title: Observational Studies of Stable Nocturnal Boundary Layers: Intermittent Turbulence, Sensible Heat Budgets and Observational Errors.

Abstract approved: Redacted for Privacy

Larry Mahrt

Atmospheric boundary layers become stably stratified at night over land when the surface becomes colder than the air layer above. In stable nocturnal boundary layers (SNBL), turbulence becomes weak and intermittent, terrain-induced phenomena such as drainage currents or gravity-waves emerge and the surface heterogeneity is enhanced. Because of their complexity and insufficient observations, a comprehensive understanding of SNBLs is not yet achieved.

In the first study of this dissertation, characteristics of intermittent turbulence in SNBLs are investigated with data collected from a network of towers. Toward this goal, turbulence kinetic energy budget, predictability and spatial extent of intermittent turbulence patches are examined. A series of analyses suggests intermittent turbulence evolves and decays as it is advected between two adjacent towers separated by 100 m or more.

In the second study, systematic observational errors of air temperature due to radiative forcing and ambiguity of the standardized measurement height over non-uniform vegetation are quantified and contrasted. An empirical formula is developed for correcting the radiatively-induced error. Implications for the systematic errors in

atmospheric boundary layer research, such as estimation of horizontal temperature advection, are discussed.

In the third study, the structure of SNBLs is investigated in terms of the sensible heat budget. As opposed to previous assumptions, the nocturnal heat budget cannot be generally balanced by the storage, vertical heat flux divergence and vertical radiative flux divergence only. An error analysis suggests that instrumental and sampling errors are unable to explain the large imbalance, implying the significance of systematic advection of potential temperature and possibly the mesoscale heat flux divergence in the heat budget.

Advection of intermittent turbulence and potential temperature has been found to be more significant in SNBLs than previously thought. Advection estimates can be challenging due to various observational errors as illustrated with an example of air temperature. Nonetheless, for better understanding of SNBLs, observational strategies or methodologies need to be improved for directly evaluating advection.

Observational Studies of Stable Nocturnal Boundary Layers: Intermittent Turbulence, Sensible Heat Budgets and Observational Errors

by

Reina Nakamura

A DISSERTATION

submitted to

Oregon State University

in partial fulfillment of
the requirements for the
degree of

Doctor of Philosophy

Presented February 4, 2005
Commencement June 2005

Doctor of Philosophy thesis of Reina Nakamura presented on February 4, 2005

APPROVED:

Redacted for Privacy

Major Professor, representing Atmospheric Sciences

Redacted for Privacy

Dean of the College of Oceanic and Atmospheric Sciences

Redacted for Privacy

Dean of the Graduate School

I understand that my dissertation will become part of the permanent collection of Oregon State University libraries. My signature below authorizes release of my dissertation to any reader upon request.

Redacted for Privacy

Reina Nakamura, Author

ACKNOWLEDGMENTS

A special thanks to my M.S. and Ph.D. advisor, Larry Mahrt for his patience and guidance throughout my graduate study. I am very grateful for the opportunity to work with him directly and to discuss a wide variety of research topics with him.

Thanks to the members of the Boundary Layer Group for their support. Scientific discussions with Dean Vickers and technical advice from John Wong were very helpful for conducting my Ph.D. research.

Thanks to all my friends who cheered me up in the course of my long-lasting graduate study.

Finally, many thanks to Mark Matheson for his support both at work and home. Without his encouragement, I would not have made it this far.

TABLE OF CONTENTS

Page

1 INTRODUCTION 1

1.1 References 2

2 A STUDY OF INTERMITTENT TURBULENCE WITH CASES-99 TOWER MEASUREMENTS 4

2.1 Abstract 5

2.2 Introduction 5

2.2.1 Intermittent Turbulence 5
2.2.2 Quantitative Description of Intermittent Turbulence 7

2.3 Data 8

2.4 Defining Intermittent Turbulence Events 9

2.5 Relevant Time-Scales for Fixed-Point Observations 14

2.6 Frequency and Spatial Extent of Intermittent Turbulence Events 16

2.7 Source of Intermittent Turbulence 22

2.7.1 Turbulent Kinetic Energy (TKE) Equation Analysis 22
2.7.2 Richardson Number 24

2.8 Advection 28

2.9 Conclusions 33

2.10 Acknowledgements 35

2.11 References 35

3 AIR TEMPERATURE MEASUREMENT ERRORS IN NATURALLY VENTILATED RADIATION SHIELDS 38

3.1 Abstract 39

TABLE OF CONTENTS (Continued)

Page

3.2 Introduction 39

3.3 Standardizing the Height of Air Temperature Measurements 41

3.4 Instrumentation and Data 47

3.5 Sources of Radiative Errors 51

3.5.1 General Considerations 51
3.5.2 Imperfect Shielding of Shortwave Radiation 52
3.5.3 Shield Surface Warming/Cooling 55

3.6 Correction of Radiatively-Induced Temperature Errors 57

3.6.1 HOBO Radiative Error 59
3.6.2 Similarity Regression Model 61
3.6.3 Robustness of Model 65

3.7 Summary 67

3.8 Acknowledgements 68

3.9 References 69

4 VERTICALLY-INTEGRATED SENSIBLE HEAT BUDGETS WITHIN STABLE NOCTURNAL BOUNDARY LAYERS 72

4.1 Abstract 73

4.2 Introduction 73

4.3 Sensible Heat Flux Budget Equation 74

4.4 Data 78

4.4.1 CASES-99 78
4.4.2 FLOSSII 79
4.4.3 Microfronts 79

TABLE OF CONTENTS (Continued)

Page

4.5 Evaluating the Vertically-Integrated Sensible Heat Budget 80

4.5.1 Storage, Vertical Heat Flux Divergence and Residual 82
4.5.2 Sensible Heat Budget: Field Experiment-Averages 83

4.6 Sources of the Residual 89

4.6.1 Statistical Significance of the Residual 89
4.6.2 Horizontal Heat Flux Divergence 92
4.6.3 Radiative Flux Divergence 92
4.6.4 Advection 94
4.6.5 Mesoscale Heat Flux Divergence 97

4.7 Conclusions 101

4.8 Appendix 103

4.8.1 Error Estimates of the Storage Term 103
4.8.2 Error Estimates of the Vertical Heat Flux Divergence Term .. 105
4.8.3 Instrumentation Problems 105

4.9 Acknowledgements 106

4.10 References 106

5 CONCLUSIONS 109

BIBLIOGRAPHY 112

LIST OF FIGURES

Figure — Page

2.1 Example time series of vertical velocity, w, sampled at 20 Hz during CASES 99. 10

2.2 Example time series of vertical velocity, w. 12

2.3 Percentage of cumulative variance $\overline{w'^2}$ as a function of averaging time scales for all the records selected by the first step of the detection algorithm from the nights analyzed for the main tower in Section 2.6 (solid lines). 13

2.4 Total number of intermittent turbulence events detected at the 5-m level across the network of towers over 15 nights. 17

2.5 Total number of intermittent turbulence events detected on the 60-m main tower over 9 nights. 18

2.6 a) Frequency distribution of the total number of satellite towers accompanying each of the 76 intermittent turbulence events detected at the 5-m level on the main tower. 20

2.7 a) Frequency distribution of total number of levels on the main tower accompanying each of the 52 intermittent turbulence events detected at the 5-m level on the main tower. 21

2.8 Top: Time series of the vertical velocity, w, at 5 m on the main tower. 25

2.9 Composite of 19 time series of the gradient Richardson number around the onset of intermittent turbulence events at main tower 5-m level. 27

2.10 Composited cross-correlation coefficients computed from $\overline{w'^2}$ as a function of pseudo-distance for hours with northerly wind. 31

2.11 a) Maximum value of composited cross-correlation coefficients between two towers in each tower combination as a function of the separation distance between the two towers. 32

3.1 Illustration of an unstable vertical temperature profile in the atmospheric surface layer. 44

Figure Page

3.2 Simulated bin-averaged error in estimated temperature for $z = Z + d_o + d_{o\ error}$ due to non-zero $d_{o\ error}$ as a function of stability for various errors in the displacement height. 46

3.3 Cross section of Davis Instruments multi-plate shield Model 7714 (Onset Computer Radiation Shield RS1). 49

3.4 a) Mean shortwave radiation ratio, $\overline{S^*}$ (%) b) difference between the downward shortwave radiation ratio and the upward shortwave radiation ratio, $S^* \downarrow - S^* \uparrow$ (%) for grass-covered (○), black (△) and white (▽) surfaces. 54

3.5 Bin-averaged deviation of the shield surface temperature from air temperature as a function of net radiation above the grass surface. . . 56

3.6 The original (gray circle) and bin-average values (black circle) of the HOBO radiative errors for all the data. 60

3.7 HOBO radiative error as a function of non-dimensional radiation forcing X. 62

3.8 Bin-averaged HOBO radiative errors for 30-min mean air temperature as a function of a) wind speed, b) shortwave or net radiation and c) non-dimensional radiative forcing, X (Eq. 3.11) for daytime (left column) and nighttime (right column). 64

4.1 The mean layer storage, $\frac{\int_{z_1}^{z_2} \frac{\partial [\theta]}{\partial t} dz}{z_2 - z_1}$ (MLS), mean layer vertical heat flux divergence, $\frac{[\overline{\theta' w'}]_{z_2} - [\overline{\theta' w'}]_{z_1}}{z_2 - z_1}$ (MLH) and mean layer residual, $\frac{R}{z_2 - z_1}$ (MLR) averaged over the entire experiment: a) CASES-99 lower layer b) CASES-99 upper layer c) FLOSSII d) Microfronts. 85

4.2 Same as Fig 4.1 except for the experiment-average of the absolute values of the mean layer storage (MLS), mean layer vertical heat flux divergence (MLH) and mean layer residual (MLR). 86

4.3 Constancy of the mean layer storage (MLS), mean layer vertical heat flux divergence (MLH) and mean layer residual (MLR). 87

LIST OF FIGURES (Continued)

Figure | Page

4.4 Joint distribution of the mean layer vertical heat flux divergence term, $\frac{[\overline{\theta'w'}]_{z_2}-[\overline{\theta'w'}]_{z_1}}{z_2-z_1}$ (MLH) and the mean layer storage term, $\frac{\int_{z_1}^{z_2}\frac{\partial[\theta]}{\partial t}dz}{z_2-z_1}$ (MLS) for all records. 90

4.5 a) Comparison of $\lceil W \rceil$ estimated by a sonic anemometer and from the continuity equation for the main tower 10-m level in CASES-99. . 95

4.6 Frequency distribution of the magnitude of mean layer $[W]$ a) CASES-99 lower layer b) FLOSSII layer and c) Microfronts layer, estimated from the residual of the heat budget. 96

4.7 Frequency distribution of horizontal potential temperature gradient inferred from the residual (Eq. 4.10) for a) CASES-99 lower layer b) CASES-99 upper layer c) FLOSSII and d) Microfronts. 98

4.8 Comparison of the spatial average of turbulence vertical heat flux, $\lceil w'\theta' \rceil$ and that of mesoscale vertical heat flux, $\lceil w^*\theta^* \rceil$ from individual hourly records. 99

4.9 Comparison of the mean layer storage, $\frac{\int_{z1}^{z2}\frac{\partial\overline{\theta}}{\partial t}dz}{z_2-z_1}$, (MLS) in Kh^{-1} estimated by two methods for a) CASES-99 lower layer b) CASES-99 upper layer c) FLOSSII and d) Microfronts. 104

LIST OF TABLES

Table		Page
3.1	Summary of instrumentation	48
3.2	Summary of data collection	50
3.3	Summary of determined coefficients for the similarity regression model for daytime and nighttime periods.	63
3.4	Statistics of the HOBO error before and after correction for the radiative error with Eq. 3.12 for 2002.	66
3.5	Statistics of the HOBO error before and after correction for the radiative error with Eq. 3.12 for summer 2003.	66
4.1	Summary of air-layers considered for heat budget analysis. "Averaging time" corresponds to the time interval over which the temperature data are pre-averaged for analysis.	81
4.2	Statistics of the mean layer storage, mean layer vertical heat flux divergence and mean layer residual terms (Kh^{-1}) over the entire field experiments.	84
4.3	Summary of the sensible-heat budget analysis.	91
4.4	Statistics of the mean layer mesoscale vertical heat flux divergence (Kh^{-1}) over the entire field experiments.	100

1. INTRODUCTION

Atmospheric boundary layers become stably stratified at night over land when the surface becomes colder than the air layer above. A comprehensive understanding of physical phenomena in stable nocturnal boundary layers (SNBL) has not yet been achieved (Nappo and Johnansson, 1999; Poulos et al., 2002). Improved understanding of the SNBL is necessary for various applications. For example, air-quality prediction requires knowledge of turbulence dispersion in the SNBL. Turbulence dispersion becomes suppressed compared to daytime convective conditions and exhaust or pollution emissions build up near the ground with strong stable stratification. Parameterization of SNBLs is also necessary for climate modeling and meteorological forecasting.

Past field observations have revealed that flows in SNBLs are complex. For example, turbulence becomes weak and intermittent with increasing stability (e.g. Nappo, 1991; Howell and Sun, 1999). Gravity waves and other mesoscale motions coexist and interact with the turbulence field (Finingan and Einaudi, 1981; Finnigan, 1988). Highly nonstationary phenomena such as shear flow instabilities, overturning Kelvin-Helmholtz billows (Thorpe, 1973) and terrain generated phenomena such as intermittent drainage currents can emerge (Sun et al., 2002). The impact of the surface heterogeneity is enhanced in the SNBL flows. Finally, the definition of the boundary layer height becomes ambiguous (Mahrt and Vickers, 2004). No theories and parameterizations are currently available for simulating the very stable nocturnal boundary layers adequately (Poulos et al., 2002). We need improved

understanding of physical processes of the SNBL from analyses of observational data.

The present dissertation consists of three manuscripts: 1) A study of intermittent turbulence with CASES-99 tower measurements, 2) Air temperature measurement errors in naturally ventilated radiation shields and 3) Vertically-integrated sensible heat budget within stable nocturnal boundary layers. These manuscripts 1) examine physical characteristics of the flow field in the SNBL from observations and 2) attempt to identify problems with the strategies or methodologies for collecting improved data in the SNBL.

In the first manuscript, the physical nature of intermittent turbulence in the SNBL is investigated. More specifically, sources, spatial scales and predictability of intermittent turbulence patches are examined. In the second manuscript, systematic errors of air temperature measurements are quantified and an empirical error-correction model is proposed. Implications for the observational errors in studies of atmospheric boundary layers are also discussed. In the third manuscript, the sensible heat budget within the SNBL is evaluated using three independent data sets. This study assesses each term in the sensible heat budget and examines the validity of a common assumption that the SNBL can be described reasonably well with a one-dimensional approach.

1.1. References

Finnigan, J.J., 1988: Kinetic energy transfer between internal gravity waves and turbulence, *J. Atmos. Sci.* **45**, 486-505.

Finnigan, J.J., and F. Einaudi, 1981: The interaction between an internal gravity wave and the planetary boundary layer. Part II: Effect of the Wave on the Turbulence Structure, *Quart. J. Roy. Meteorol. Soc.* **107**, 807-832.

Howell, J.F., and J. Sun, 1999: Surface-layer fluxes in stable conditions, *Boundary-Layer Meteorol.* **90**, 495-520.

Nappo, C. J., 1991: Sporadic breakdowns of stability in the PBL over simple and complex terrain, *Boundary-Layer Meteorol.* **54**, 69-87.

Nappo, C.J., and P-E Johansson, 1999: Summary of the Lövånger international workshop on turbulence and diffusion in the stable planetary boundary layer, *Boundary-Layer Meteorol.*, **90**, 345-374.

Poulos, G.S., W. Blumen, D.C. Fritts, J.K. Lundquist, J. Sun, S.P. Burns, C. Nappo, R. Banta, R. Newsom, J. Cuxart, E. Terradellas, B. Balsley, and M. Jensen, 2002: CASES-99: A comprehensive investigation of the stable nocturnal boundary layer, *Bull. Amer. Meteor. Soc.*, **83**, 555-581

Sun, J., S.P. Burns, D.H. Lenschow, R. Banta, R. Newsom, R. Coulter, S. Frasier, T. Ince, C. Nappo, J. Cuxart, W. Blumen, X. Lee, and X-Z Hu, 2002: Intermittent turbulence associated with a density current passage in the stable boundary layer, *Boundary-Layer Meteorol.* **105**, 199-219.

Thorpe, S.A., 1973: Turbulence in stably stratified fluids: a review of laboratory experiments, *Boundary-Layer Meteorol.* **5**, 95-119.

Vickers, D., and L. Mahrt, 2004: Evaluating formulations of stable boundary-layer height. *J. Appl. Meteor.*, **43**, 1736-1749.

2. A STUDY OF INTERMITTENT TURBULENCE WITH CASES-99 TOWER MEASUREMENTS

Reina Nakamura and Larry Mahrt

Boundary Layer Meteorology,

Kluwer Academic Publishers, Utrecht, The Netherlands.

Vol. 114 Issue 2

2.1. Abstract

Characteristics of intermittent turbulence events in stably stratified nocturnal boundary layers are investigated with data collected in the CASES-99 tower array of 300-m radius. The array consists of a central 60-m tower with eddy covariance measurements at 8 levels and 6 satellite towers with eddy covariance measurements at 5 m. A significant increase in the magnitude of vertical wind velocity (σ_w^2) and spectral information are used to define the onset of an intermittent turbulence event. Normally, only a subset of 5m-levels in the tower network experience an intermittent turbulence event concurrent with one at the 5m-level on the main tower. This behaviour reveals the small horizontal extent of most events. Intermittent turbulence events at the main tower 5m-level are normally confined to a layer much thinner than the 60-m tower height.

The turbulent kinetic energy (TKE) budget is evaluated for intermittent turbulence events observed at the 5-m level on the main tower. Generally, the onset of an intermittent turbulence event is not closely related to the reduction of the gradient Richardson number below 0.25, the critical Richardson number of turbulence generation for linear instability. Possible explanations including the influence of advected turbulence patches are discussed.

2.2. Introduction

2.2.1. Intermittent Turbulence

In stably stratified nocturnal boundary layers, turbulence often becomes weak and intermittent. Intermittency has been defined in different ways. In the present study, intermittency requires that the turbulence is partially suppressed below some

small threshold for periods much longer than the time-scale of the individual main eddies. This global intermittency is quite different from microscale intermittency of dissipation being confined primarily to small subregions of large eddies (Mahrt, 1989).

Intermittent turbulence may be generated by interaction between turbulence and the mean shear, nonstationary drainage flows, gravity waves and modulation of the shear by meandering motions. Sun et al. (2002) observed large-eddy overturning above a fast propagating density current. Thermal instability and subsequent intermittent turbulent patches developed aloft as well as close to the ground. A drainage flow advancing against the ambient flow also produces intermittent turbulence due to shear at the interface of the two flows (Mahrt, 1985). Blumen (1984) observed breakdown of Kelvin-Helmholtz (K-H) billows into turbulence at the interface of the drainage and ambient flows behind drainage fronts propagating against the ambient flows. Intermittent turbulence in the presence of K-H instabilities were also observed in Kondo et al. (1978) and Coulter (1990). Thorpe (1973) examined development of turbulence by K-H instability in a laboratory experiment.

Gravity waves induce turbulence by significant energy transfer from wave to turbulence modes depending on the phase difference between the wave-modified Reynolds stress and the wave-induced shear (Finnigan and Einaudi, 1981; Finnigan, 1988) . In addition, amplifying gravity waves can lead to overturning and microscale thermal instability, thus generating turbulence (Atlas et al., 1970; Nappo, 2002). As three dimensional turbulence decays in strongly stratified flow, its energy can be partitioned into gravity waves and quasi-two-dimensional turbulence or meandering flow (Riley et al., 1981; Lilly, 1983). The former propagates away from the generation region while the latter can lead to upscale energy transfer possibly due

to vortex merging. Through shear instability, part of the energy of the meandering flow may be transferred back into three-dimensional turbulence.

2.2.2. Quantitative Description of Intermittent Turbulence

Nappo (1991) considered each period of horizontal wind speed-temperature covariance, defined by digital bandpass filtering, to be in an intermittent turbulent period when it exceeds 10% of the nighttime average. Katul et al. (1994) defined intermittent bursts of sensible heat flux in terms of a threshold value, which was determined from the standard deviation of the heat flux. In Howell and Sun (1999), the degree of intermittency of the vertical sensible heat flux within a 10-min record is defined by counting the number of 1.25-min sub-periods, which accumulatively account for 90% of the total 10-min flux; the lower the number of sub-periods, the higher the degree of intermittency. In Coulter and Doran (2002), 1-min vertical heat fluxes within a night are ordered according to their magnitudes. An individual period of heat flux is identified to be in an intermittent turbulence event if it is one of the periods which makes up the first 50% of the total integrated flux of the night. With increasing intermittency of turbulence, fewer periods are identified as intermittent turbulence events.

In neutrally stratified surface layers of laboratory flows, sudden increases of flow velocity and turbulent fluxes are also observed (e.g. Blackwelder and Kaplan, 1976). These phenomena occur as streaks of low-speed fluid formed between two of the vortices are lifted away from the surface, oscillate and eventually break down into chaotic motion. For isolating such events, the Variable Interval Time Averaging (VITA) technique of Blackwelder and Kaplan (1976) with prescribed threshold values is frequently used. Narasimha and Kailas (1990) applied the VITA technique

for investigating turbulent bursts in the neutral atmospheric boundary layer. The VITA method is not optimal for our goal of identifying sudden changes of turbulent intensity because the VITA method seeks deviations from the mean of the entire record and thus assumes stationarity for the entire record.

2.3. Data

The Cooperative Atmosphere-Surface Exchange Study-99 (CASES-99) was conducted near Leon, Kansas in October 1999 and provided an unprecedented observational network for investigating the vertical and horizontal structure of the nocturnal boundary layer (Poulos et al., 2002). The data analyzed in the present study were collected on the 60-m scaffolding main tower, a 10-m tower adjacent to the main tower and six surrounding 10-m satellite towers (see Fig. 2.4).

On the 60-m main tower, sonic anemometers (Campbell CSAT and Applied Technologies, Inc.) were deployed at 6 levels (10 m, 20 m, 30 m, 40 m, 50 m and 55 m) for wind and flux measurements. On the same tower, thermocouples were deployed at 32 levels with 1.8-m intervals between 2.3 m and 58.1 m height (Sun et al, 2002). In addition, a nearby 10-m tower was equipped with sonic anemometers at 1.5 m and 5 m and thermocouples at 0.23 m and 0.63 m. Because the sonic anemometer at 1.5 m was moved to 0.5 m on 22 October, 1999, the notation for the combined data will appear as 1.5 m (0.5 m) hereafter. The 10-m tower was located 10 m away from the main tower to avoid flow distortion by the bottom of the main tower. The measurements on the 10-m tower will be analyzed as if they had been made on the main tower. Sonic anemometers were mounted at 5 m above the ground on the six satellite towers.

All the sonic anemometers measured the u, v and w components of wind speed and the virtual temperature θ at 20 Hz. The thermocouple data were collected at 5 Hz. Generally, the observational site was considered to be flat although the surface elevations of the towers differed by as much as 6 m over a horizontal distance of a few hundred metres. The mean sunset and sunrise at the site were 1750 and 0635 local standard time, respectively. In the present study, 1900 - 0700 local standard time is considered to be the time period of the stable nocturnal boundary layer.

2.4. Defining Intermittent Turbulence Events

Well-defined and isolated intermittent turbulence events, as in Fig. 2.1 a - b, are relatively rare in the geophysical records, which we have examined. Less well-defined intermittent patches of turbulence are much more common as in Fig. 2.1 c - g. Except for relatively rare well-defined events, the definition of geophysical intermittent turbulence is not straightforward or unique.

Here, two factors are required as identifiers of the onset of intermittent turbulence events. First, the increase in the magnitude of the vertical turbulence velocity needs to occur rapidly. Secondly, the magnitude of the vertical turbulence velocity needs to exceed a threshold value. Toward this goal, a two-step algorithm is developed for detecting the onset of an intermittent turbulence event. In the first step, $\overline{w'^2}$ is computed with a forward-moving pair of non-overlapping consecutive windows applied to vertical velocity. The time series of vertical velocity is linearly detrended within each window to partially remove the influence of waves and other nonturbulent motions on the computed perturbation flow. The ratio of increase of $\overline{w'^2}$ between the two windows with respect to the variance of the first window is referred to as turbulence enhancement index (TEI):

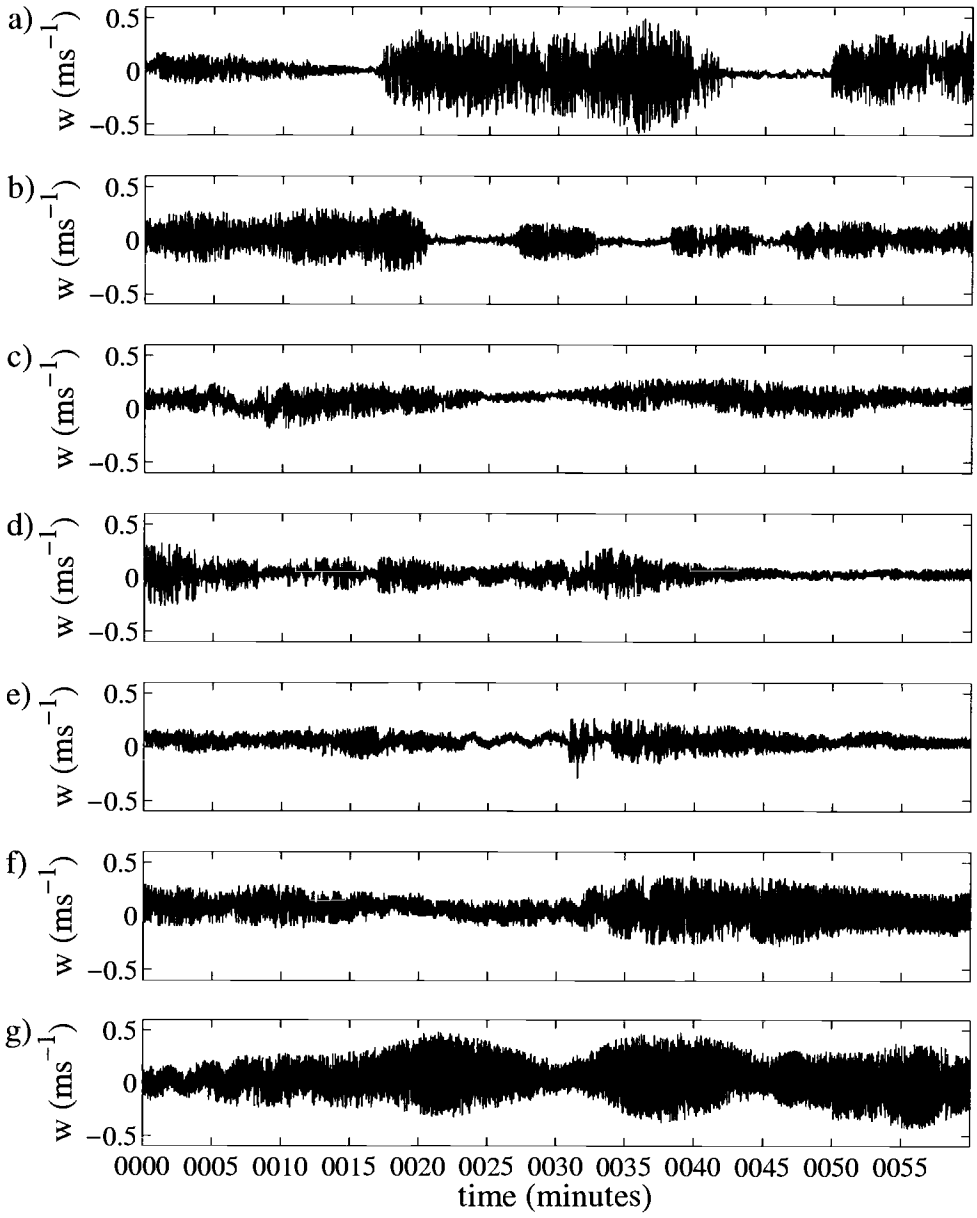

FIGURE 2.1. Example time series of vertical velocity, w, sampled at 20 Hz during CASES 99. a) - b) Periods of intermittent turbulence are well-defined between two quiescent periods; c) - g) periods of intermittent turbulence are not as clearly defined compared to those in a) - b).

$$TEI = \frac{\overline{w_2'^2} - \overline{w_1'^2}}{\overline{w_1'^2}} \tag{2.1}$$

where $\overline{w_1'^2}$ and $\overline{w_2'^2}$ indicate variances of vertical velocity computed for each of the two consecutive windows. A window width of 300 seconds is chosen as it is sufficiently short to exclude most of the wave-like motions. This window width is also considered long enough for the investigation of sources of intermittent turbulence (Section 2.7). The set of filtering windows is sequentially moved forward by 10 seconds. For defining the onset of intermittent turbulence events, TEIs are examined in descending order each night. The onset of an intermittent turbulence event is defined if the TEI is greater than the threshold value and not within $\pm 300s$ of a previously defined onset. The threshold value is set to 3 in the present investigation. In addition, a minimum threshold value of 0.001 $m^2 s^{-2}$ is set for $\overline{w_2'^2}$ to eliminate cases where turbulence may not be adequately measured.

The above procedures are sometimes insufficient to isolate turbulent motions from low frequency motions (Fig. 2.2). To remove records with large TEI due to increasing low frequency motions not associated with turbulent motions, an additional step is introduced for the detection algorithm. The multi-resolution (MR) spectra analysis (Howell and Mahrt, 1997) is performed on the vertical velocity in the records qualified as potential onsets of intermittent turbulence in the first step. The MR analysis requires 2^m data points where m is an integer. To avoid interpolation to a finer grid, the vertical wind velocity data of only the first 204.8 seconds ($m = 12$) of the 300-second-window are considered. In Fig. 2.3, the scale of motions contributing to the variance $\overline{w_2'^2}$ in each record is illustrated in terms of a percentage of the cumulative variance with respect to the total variance as a function of averaging time scale. Composited w spectra indicate that the spectral peak associated with turbulent motions typically occurs at time scales of a few seconds.

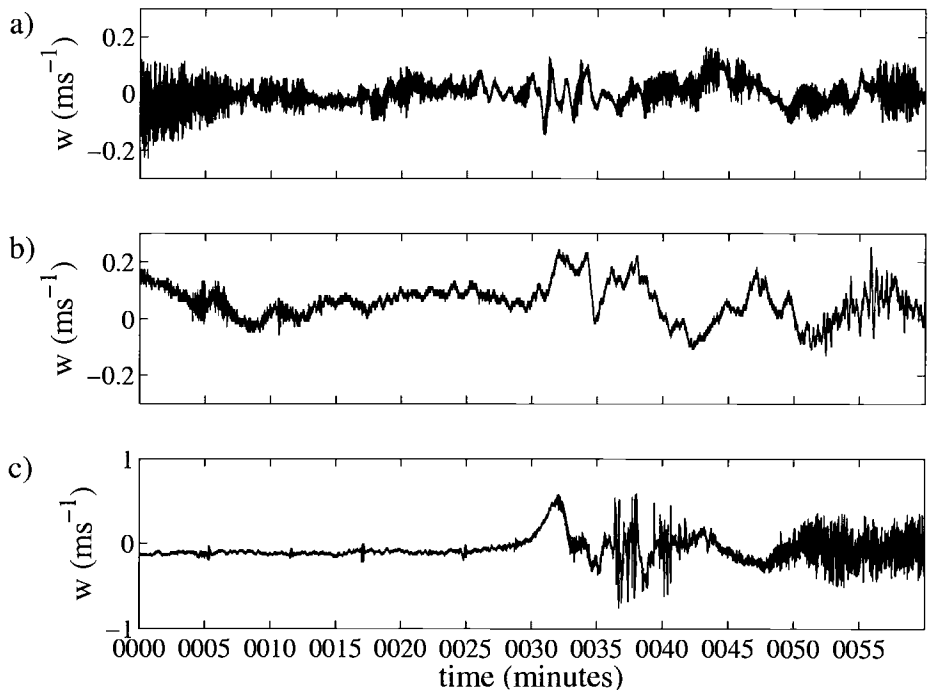

FIGURE 2.2. Example time series of vertical velocity, w. The Turbulence Enhancement Index (TEI) between two consecutive 300-second windows centered at 0030 remains large despite linear-detrending within each window. In this case, the vertical motion modulated by wave-like motion, occurring at a lower frequency than turbulent motions, is responsible for the large TEI.

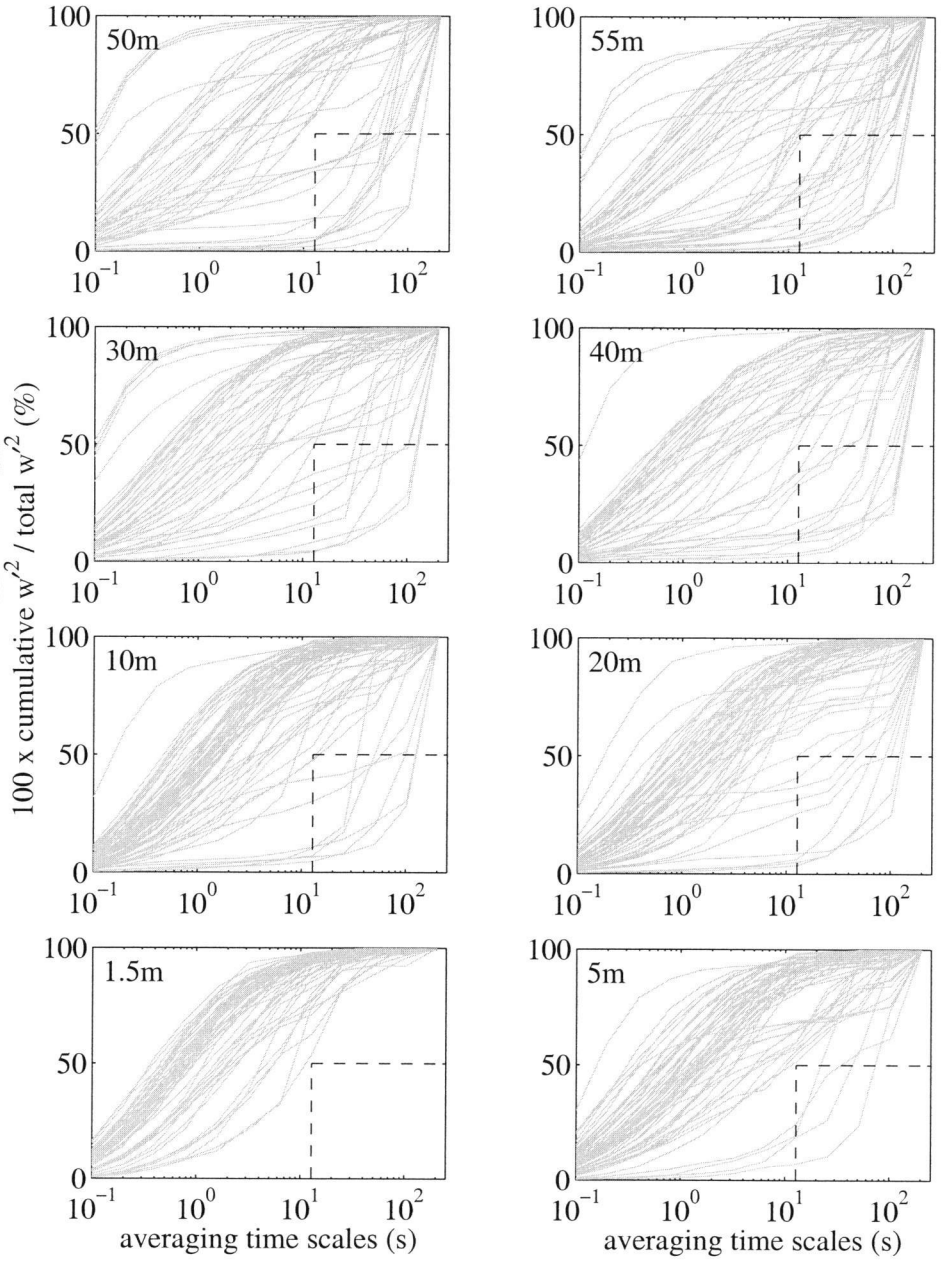

FIGURE 2.3. Percentage of cumulative variance $\overline{w'^2}$ as a function of averaging time scales for all the records selected by the first step of the detection algorithm from the nights analyzed for the main tower in Section 2.6 (solid lines). Records falling in the rectangle areas in dashed-lines will not be considered as onsets of intermittent turbulence events.

Based on inspection of all the w spectra, we require that the cumulative variance at the dyadic averaging time scale of 12.8 seconds ($m = 8$) is greater than 50% of the total variance. Otherwise, the record is removed, as the increase of vertical velocity variance with time in the record is due more to lower frequency phenomena than turbulence. This requirement is weaker than establishment of an inertial subrange. The percentage of removed records increases monotonically with height from 0 % at 1.5m (0.5m) to 42% at 55m. Lower-frequency vertical velocity fluctuations are more prevalent at higher levels, as also verified by visual inspection of Fig. 2.3. The majority of the cumulative spectra show a similar shape containing significant negative curvature. The eliminated records generally correspond to a cumulative spectra with positive curvature for the range of scales expected for turbulence in stable conditions.

Since intermittent turbulence events occur with a variety of amplitudes and durations and are frequently not confined by abrupt changes in intensity, the number of captured events is sensitive to selection criteria. This sensitivity reflects the variety of signatures in stratified turbulent geophysical flows. The total number of detected onsets of intermittent turbulence increases by 65% when decreasing the threshold value from 3 to 2. Similarly, the total number of onsets of intermittent turbulence events decreases by 32% when increasing the threshold value from 3 to 4. The qualitative conclusions of the present study did not change over this range of threshold values.

2.5. Relevant Time-Scales for Fixed-Point Observations

We recognize three time-scales for interpreting intermittent turbulent motions observed at fixed points in space such as towers. The lifetime of a patch of

turbulence, τ, is determined by the evolution and decay of the patch. The time required for the patch of turbulence to travel between two towers due to advection by the mean flow is

$$\tau^* = \frac{\Delta x}{U} \tag{2.2}$$

where Δx and U denote the separation distance between the two towers and the mean horizontal wind speed along the axis of the towers, respectively. The time-scale for the patch of turbulence to pass by a tower is defined as

$$\tau' = \frac{L_p}{U} \tag{2.3}$$

where L_p is the horizontal length scale of a patch of turbulence traveling with the mean flow. This advective time-scale determines the "perceived" duration of the patch of turbulence at a fixed tower, sometimes mistakenly interpreted as the lifetime of the patch of turbulence, τ.

If the between-tower advective time-scale τ^* is not small compared to the lifetime τ, then intermittent turbulent motions observed at the two towers are in different phases of development or decay. The patch of turbulence evolves or decays significantly as the patch is advected between the two towers. In this case, tracing turbulent patches between towers becomes tenuous.

In order to study the structure of the turbulent patch from an individual tower, the time for a patch of turbulence to pass the tower must be small compared to the evolution time scale of the patch ($\tau' << \tau$). This is a necessary but not sufficient condition since individual eddies within the patch may have shorter life times than the patch itself. If this condition holds, a patch of turbulence observed at a tower is considered to advect past the tower rather than locally generated. Note that approximate validity of Taylor's frozen turbulence hypothesis is the opposite

asymptotic limit of the assumption that the evolution and decay of turbulence can be studied from an individual tower.

2.6. Frequency and Spatial Extent of Intermittent Turbulence Events

Only the nights during which data are available at all locations of interest for 70% of the time, are considered. Time periods are considered only when data are available at all levels or all spatial locations. These criteria are applied separately for the 5-m levels across the tower array and for the 8 levels of sonic anemometers on the main tower. A total of 15 nights fulfill the data selection criterion for the 5-m levels and 9 nights satisfied the criterion for all levels on the main tower.

On average, events are detected 4 to 7 times a night at each instrument location, with between-night standard deviation of 2 - 5 events, depending on the location (Fig. 2.4). Fewer events occur on windy nights and fewer are detected on the northeast side of the array. The northeast part of the tower array is situated at higher elevation than the rest of the array. On average, $\overline{w'^2}$ observed at the 5-m level is greater at the towers located at higher elevations (not shown). The stronger average turbulence corresponds to less frequent quiet periods and therefore fewer events.

The frequency of turbulence events decreases with height (Fig. 2.5). On average, intermittent turbulence events occur 5 - 6 times a night at and below 20 m and 3 - 4 times a night above 20 m. When wave-like motions are present aloft at the main tower, intermittent turbulence is sometimes induced near the surface in phase with the wave-like motions.

The spatial extent of intermittent turbulence events observed at the main tower 5-m level is estimated in terms of concurrent intermittent turbulence events

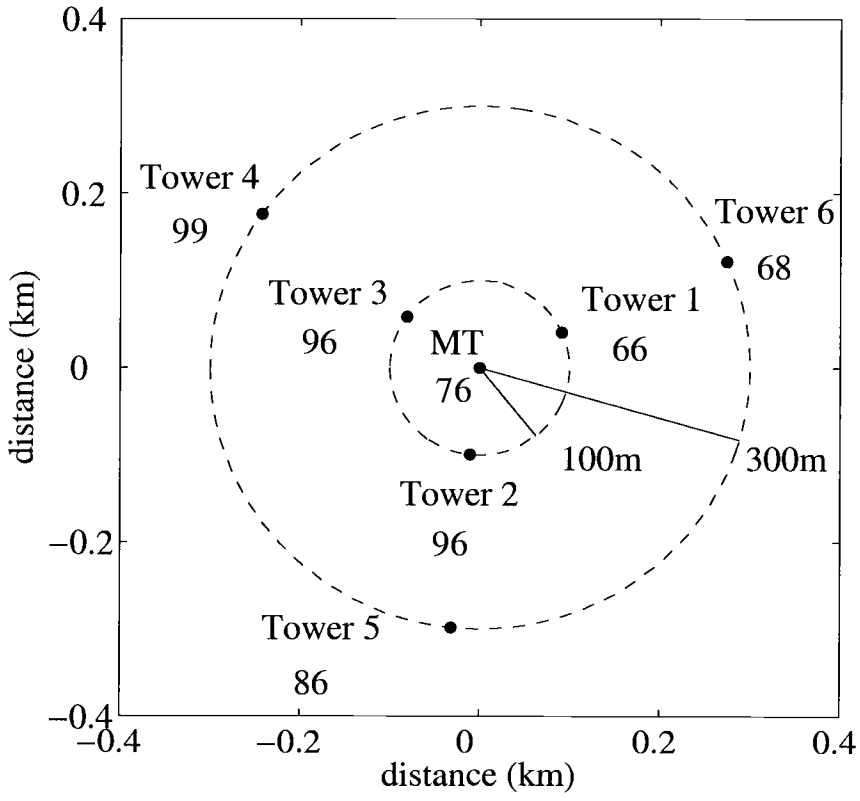

FIGURE 2.4. Total number of intermittent turbulence events detected at the 5-m level across the network of towers over 15 nights.

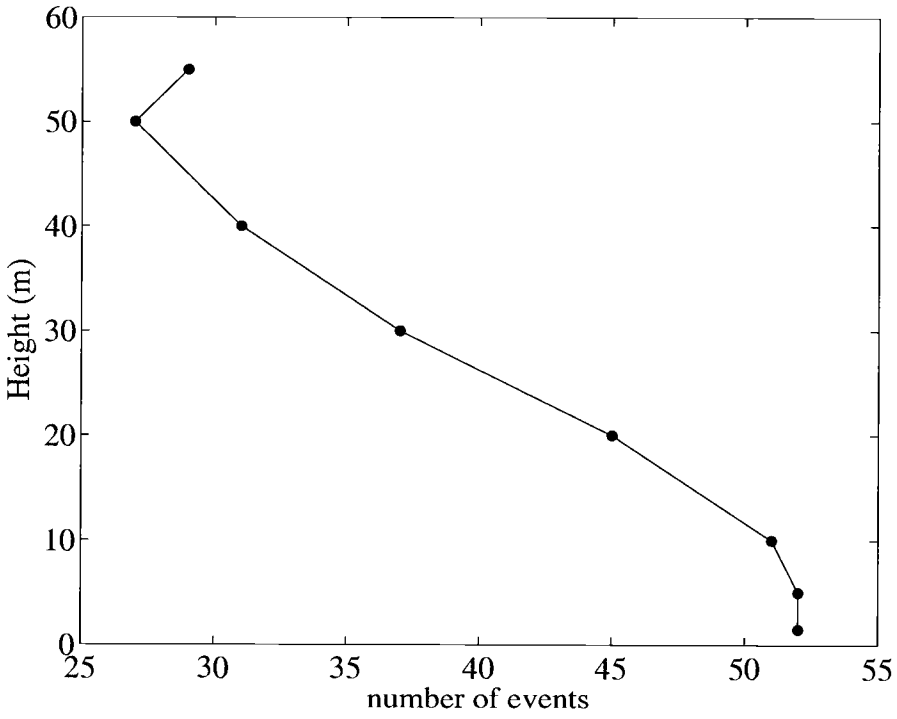

FIGURE 2.5. Total number of intermittent turbulence events detected on the 60-m main tower over 9 nights.

observed at the other towers within a specified time interval. The choice of the cut-off time interval must allow the intermittent turbulence event to advect through the observational domain; that is, be larger than the between-tower advective time τ^*. However, if the cut-off time interval is too large, turbulence unrelated to the one observed at the main tower 5-m level may be inadvertently included. One choice of the cut-off time-scale is τ^*, but the patches sometimes propagate with a different speed and direction from the mean wind. Animated motions of turbulence events in the observational domain and inspection of time series of the turbulence suggest that $\pm$ 100 seconds and $\pm$ 300 seconds are reasonable choices for the cut-off time intervals for the towers on the inner circle and on the outer circle, respectively.

The frequency distribution of the total number of towers which experience intermittent turbulence events concurrent with events at the main tower 5-m level (Fig. 2.6a), indicates that most events affect only a small subset of the towers, revealing the small horizontal extent of most of the events. The northwest side of the tower array accompanies events at the main tower 5-m level less frequently compared to the other part of the domain for reasons unknown.

A similar analysis of the vertical frequency distribution (cut-off time-scale $= \pm$ 100 s) shows that intermittent turbulence events at the main tower 5m-level are accompanied by one or more additional observational levels for only 38% of the events even without a vertical contiguity requirement (Fig. 2.7). 80% of these multi-level events extend to only one or two adjacent levels. In general, the vertical extent of an intermittent turbulence event is confined to a layer substantially thinner than the tower height.

The above results depend on the choice of time-scale for defining turbulence events. Parent disturbances on larger space and time scales may spawn intermittent

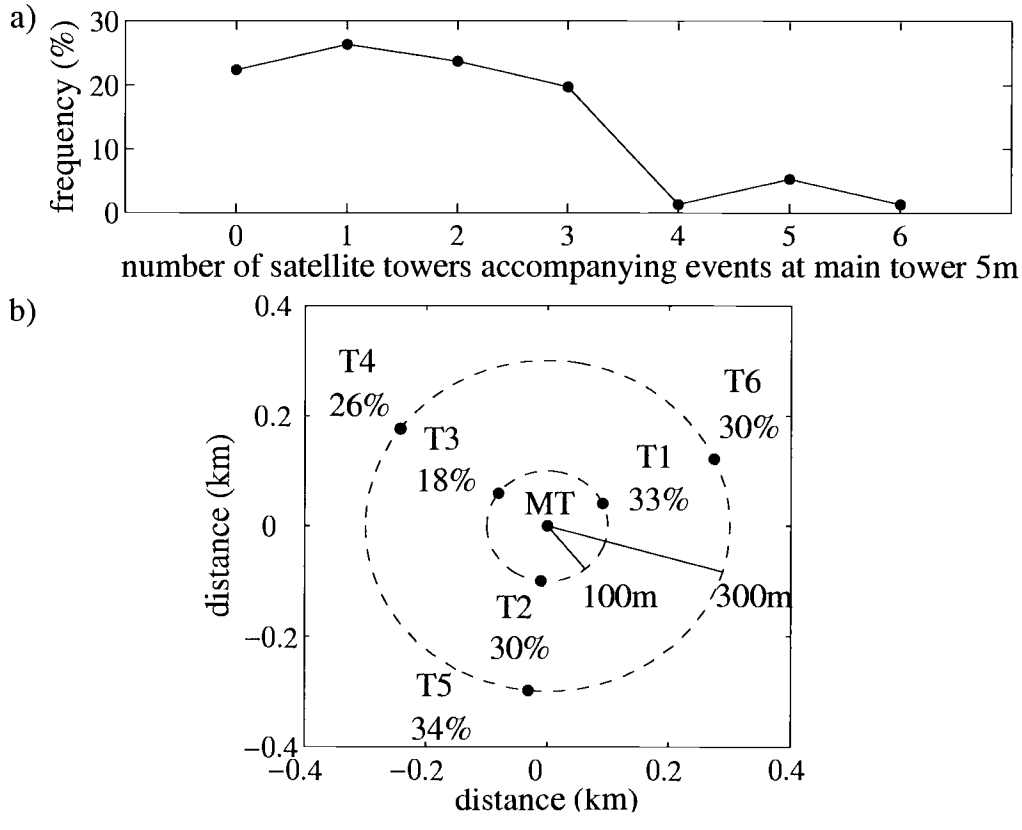

FIGURE 2.6. a) Frequency distribution of the total number of satellite towers accompanying each of the 76 intermittent turbulence events detected at the 5-m level on the main tower. b) Percentage of events detected at each of the satellite towers when an event is observed at the 5-m level on the main tower.

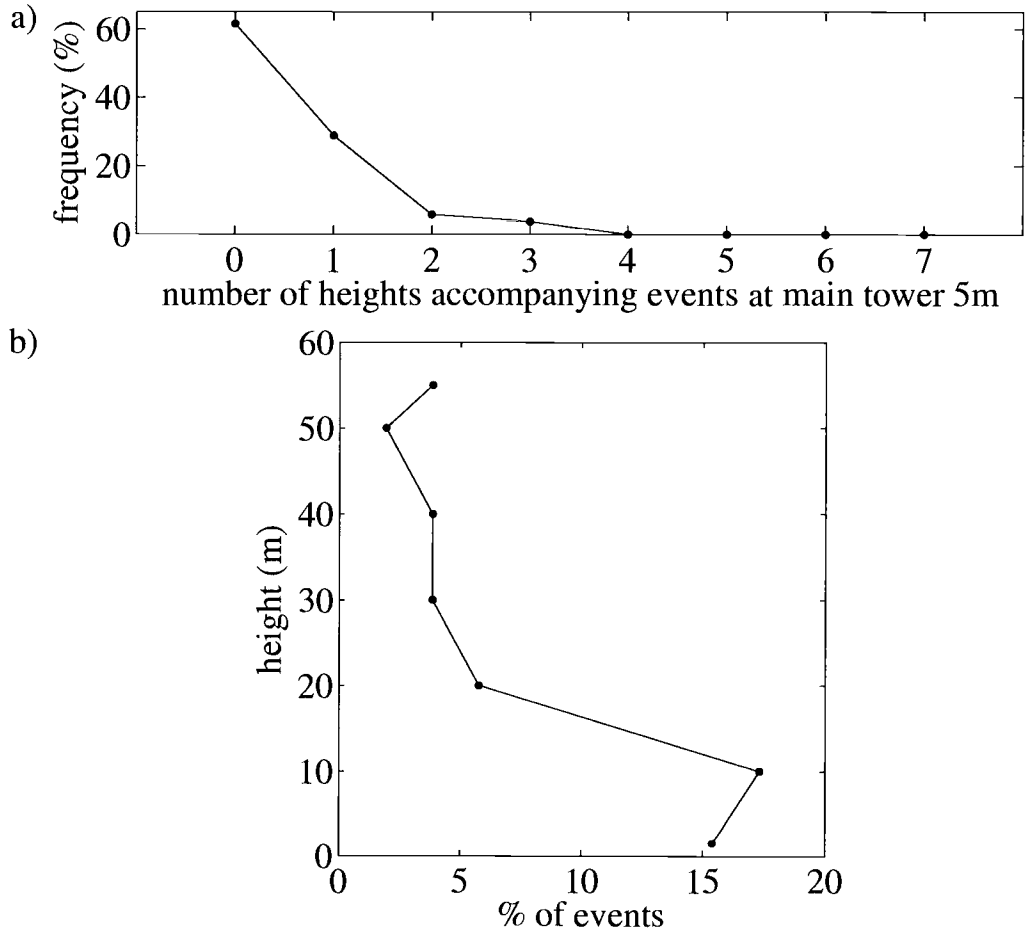

FIGURE 2.7. a) Frequency distribution of total number of levels on the main tower accompanying each of the 52 intermittent turbulence events detected at the 5-m level on the main tower. b) Percentage of events detected at each level on the main tower when an event is detected at the 5-m level on the same tower.

turbulence events (Sun et al., 2002). Such parent disturbances can occupy the entire tower layer (60 m) and extend across the entire surface network (600 m in diameter).

2.7. Source of Intermittent Turbulence

2.7.1. Turbulent Kinetic Energy (TKE) Equation Analysis

The TKE equation is evaluated to help identify the source of the intermittent turbulence events. With intermittent turbulence, the definition of the mean and fluctuating motion is to some degree ambiguous. Since the random flux errors are large for individual turbulent patches, our goal here is to assess only the order of magnitude of the terms in the TKE equation.

To include horizontal transport, the TKE equation is evaluated only at the main tower 5-m level where data are available for the tower network. As an additional constraint, the wind must be flowing from one of the inner circle towers to the main tower continuously before and during the intermittent turbulence event. The permitted wind direction sectors are 65° (± 15°) and 185° (± 15°), corresponding to the wind coming from Towers 1 and 2 to the main tower, respectively (Fig. 2.4). Since the sonic anemometers were deployed on booms facing east on all towers, the wind direction sector of 305° (± 15°) is not considered, which includes the wind direction from Tower 3 to the main tower.

In Einstein notation, the TKE equation can be written as

$$\frac{\partial \overline{e}}{\partial t} = -\overline{U_j}\frac{\partial \overline{e}}{\partial x_j} + \delta_{i3}\frac{g}{\overline{\theta}_v}\overline{u_i'\theta_v'} - \overline{u_i'u_j'}\frac{\partial \overline{U_i}}{\partial x_j} - \frac{\partial \overline{u_j'e}}{\partial x_j} - \frac{1}{\overline{\rho}}\frac{\partial \overline{u_i'p'}}{\partial x_i} - \varepsilon \qquad (2.4)$$

From left to right, the terms in the equation indicate the storage, advection, buoyant production or destruction, shear production or loss, turbulent transport, pressure correlation and dissipation of TKE. For evaluating the TKE terms, covariances and

triple correlations are calculated in the coordinate system where the x-direction is aligned with the mean wind. A running window of 100 seconds width is adopted for defining turbulent motions based on Vickers and Mahrt (2003). The beginning of the non-overlapping 100-second-windows coincides with the beginning of the intermittent turbulence event to be investigated. The calculated covariances and triple correlations are then averaged with a running mean window of 300-second width sequentially moved forward 100 seconds per calculation. This two-step methodology is chosen to minimize the influence of mesoscale motions on the computed fluxes and to reduce the random flux error although random errors are still large.

All the gradients appearing in the TKE equation except the vertical wind shear are evaluated with finite differencing. The vertical wind shears for the along- and cross-wind directions are estimated from a log-linear curve fit to the mean of the total horizontal wind at 1.5 m (0.5 m), 5 m and 10 m. For the fit, the wind speed is assumed to vanish at the aerodynamic roughness length, which is 0.03 m for this site according to the vertical wind profiles in near neutral conditions. If the R-square value of the log-linear curve fit to the vertical wind speed profile is less than 0.95, the fit is considered to be inadequate and the shear-production term (the 3rd term in RHS of Eq. 2.4) is not computed. The dissipation rate of turbulence is calculated from the inertial subrange of the horizontal wind velocity spectra according to Edson and Fairall (1998). Terms in the TKE equation, which involve pressure, the mean vertical velocity, and gradients in the cross-wind direction are not evaluated due to inadequate or unavailable data. The term $\overline{u'u'}\frac{\partial \overline{U}}{\partial x}$ can be evaluated with the present data, however it is not included in the analysis as the term $\overline{v'v'}\frac{\partial \overline{V}}{\partial y}$ (not evaluated) can be the same order of magnitude and opposite in sign.

The existing data set allows evaluation of the TKE equation for a total of 4 intermittent turbulence events on the main tower 5-m level for the wind directions

of 65° and 4 events for 185°. In 5 of the 8 cases, local generation by the vertical shear is the primary source of turbulence and residuals are smaller than or at the same order of other TKE terms, as in the examples in Fig. 2.8. Event 1 and Event 2 are the intermittent turbulence events with the smallest and largest residuals of the 5 events. The dissipation term is the major sink of turbulence, the same order of magnitude of the shear-generation term. Subject to the difficulties of estimating advection, the horizontal advection of TKE sometimes reaches about half of the shear-generation term and contributes to local reduction of TKE. The buoyancy destruction of TKE is on the order of 20 - 30% of the shear-generation term. The vertical and horizontal turbulent transport of TKE are negligible for all the cases and are not plotted in Fig. 2.8. Mahrt and Vickers (2002) found that downward transport of turbulence is significant in the upper part of the tower layer, but usually becomes small near the surface.

In 3 out of the 8 cases, for which the TKE equation is evaluated, the vertical shear-generation term is unable to balance larger sink terms, and the residual becomes significantly larger than any evaluated terms. Possible reasons for the large residual include large random flux errors and contributions of unevaluated terms in the TKE budget.

2.7.2. Richardson Number

Generation of intermittent turbulence is often associated with reduction of the gradient Richardson number (Kondo et al., 1978; Mahrt and Larsen, 1982; Blumen, 1984). In the present study, evolution of the gradient Richardson number before and after onsets of intermittent turbulence events at the main tower 5-m level is evaluated.

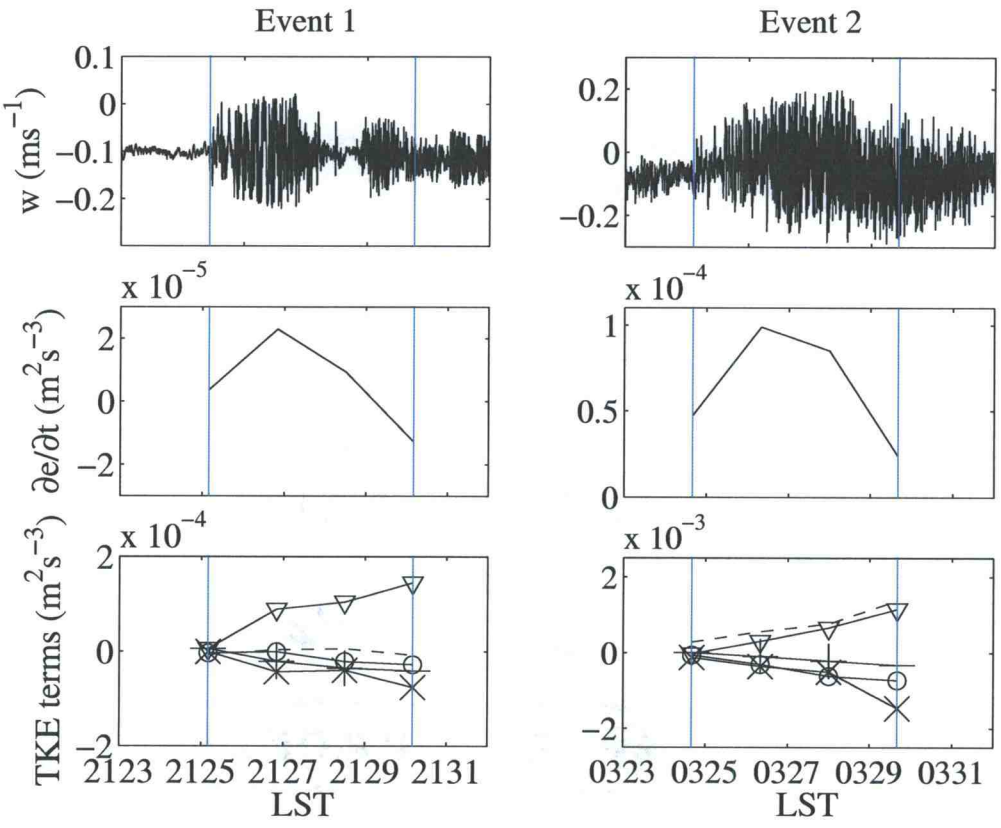

FIGURE 2.8. Top: Time series of the vertical velocity, w, at 5 m on the main tower. Vertical lines enclose turbulence events detected at 21:25:10 on 17 Oct, 1999 (Event 1) and 03:24:40 on 26 Oct, 1999 (Event 2). Middle: Local temporal change of turbulent kinetic energy. Bottom: Terms of the turbulent kinetic energy (TKE) equation evaluated for the intermittent turbulence events. $\circ : -U\frac{\partial e}{\partial x}$, $+ : \frac{g}{\theta_v}\overline{w'\theta'}$, $\bigtriangledown : -\overline{w'u'}\frac{\partial U}{\partial z} - \overline{w'v'}\frac{\partial V}{\partial z}$, $\times : -\varepsilon$, dashed line (- -): +residual. Time on the horizontal axis corresponds to the end time of a forward moving 300-second window discussed in the text.

The present analysis does not require the wind direction to coincide with the alignment of the main tower and another tower upwind. The mean wind speed and temperature are computed from averaging over a width of 100 seconds. A series of non-overlapping 100-second-windows, within which the Richardson number is calculated, is generated such that the beginning of a window coincides with the beginning of an intermittent turbulence event. A total of 31 turbulence events qualified for the Richardson number analysis after discarding cases with flow through the tower. The vertical gradients of the mean wind speed and temperature are calculated from regressed log-linear curves in the same way as in the estimate of the TKE shear-production term. For estimating the temperature gradient, the thermocouple data at 7 levels between 0.23 m and 9.5 m are fitted. Again, if the R-square value of either the wind speed or temperature profile before and after an intermittent turbulence event is less than 0.95, no Richardson number is calculated. This condition eliminates 12 events because of emerging ragged mean wind speed and temperature profiles. The computation of mean vertical gradients for such non-stationary events is often unreliable.

The vertical resolution for temperature data is finer than that for the wind speed data. Degrading the resolution of the temperature data to that for the wind speed causes little quantitative and qualitative changes in the estimated Richardson number. This result probably attributes to the fit to a log-linear curve instead of the use of a simple finite-difference for estimating the vertical gradients of temperature and wind speed.

The composite of a 600-second time series which engulfs each of the 19 turbulence events (Fig. 2.9) indicates that the Richardson number tends to decrease only after a part of the intermittent turbulence event is within the averaging window. In 16 of the 19 cases, the Richardson number decreases between the 100-second window

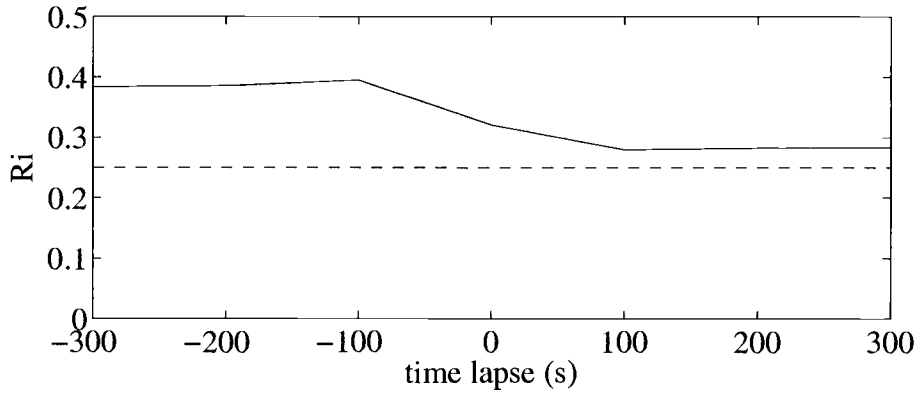

FIGURE 2.9. Composite of 19 time series of the gradient Richardson number around the onset of intermittent turbulence events at main tower 5-m level. The time on the horizontal axis indicates the start time of the 100-second-window with respect to onsets of intermittent turbulence events. The dashed line indicates Ri = 0.25.

immediately prior to the onset of an intermittent turbulence event and the window, which contains the first 100 seconds of the intermittent turbulence event. Because the Richardson number decreases simultaneously with the initiation of the intermittent turbulence event, it is difficult to distinguish if the reduction of Richardson number is the cause or the consequence of the turbulence event.

In 12 of the 19 cases, the Richardson number remains above 0.25, the critical gradient Richardson number for linear instability, even in the last 100 seconds of the intermittent turbulence event. A few possible reasons may be considered for the observed high Richardson number at the commencement of the mixing. First, the computed Richardson number could be larger than the gradient Richardson number at the observational level if the turbulence is generated over a layer that is thinner than the layer of calculation (Lyons et al., 1964; Woods, 1969; Kunkel and Walters, 1982; Kim and Mahrt, 1992). For the present data, intermittent turbulence

events are often confined to thin layers (Section 2.6). Second, if the assumption of infinitesimally small initial perturbation is relaxed, turbulence may develop at a higher Richardson number than 0.25 (Drazin, 1977; Majda and Shefter, 1998). Pre-existing weak turbulence or mesoscale motions seem to be always present. Third, the critical Richardson number becomes larger or smaller than 0.25 according to the vertical curvature of the wind profile (Abarbanel et al., 1984; Grisogono, 1994). Finally, the composite appears to include some cases of large Richardson number where the turbulence patch is advected past the tower (Section 2.8) and therefore was generated upwind. In the later stage of turbulence events, the Richardson number could be large due to the reduction of shear by turbulent mixing. In other terms, the original generation of the turbulence patch may have occurred upwind when the Richardson number was smaller.

The Richardson number decreases monotonically in the three 100-second periods prior to the onset of an intermittent turbulence event in only 4 out of the 19 cases. In 12 cases, the Richardson number increases between the two 100-second periods prior to the onset of an intermittent turbulence event. In only 2 cases, the Richardson number is below 0.25 in the last 100-second-period prior to the onset. The behaviour of the Richardson number is not a good predictor of turbulence events at a given location in the present analysis.

2.8. Advection

For evaluating the advection of TKE in Section 2.7, the local horizontal gradient was calculated from linear finite-difference using two adjacent towers. Fitting data from the towers to a two-dimensional function of x and y was determined to be questionable due to the limited number of stations and the influence of small

local variations of terrain. The estimated horizontal gradient is accurate only if the quantity of interest increases or decreases roughly linearly between the two locations. Therefore, when the length of a patch of turbulence, L_p, is less than the minimum tower spacing of 100 m, or when the patch is passing through the downwind tower into the direction that does not coincide with the alignment of the two adjacent towers, the finite difference calculation of the horizontal gradient of TKE is unreliable and could even yield the wrong sign. For the same reasons, the advection calculations in the TKE analysis in Section 2.7 must be interpreted with caution.

To statistically reexamine the potential influence of advection, the time-lag cross-correlation coefficients of the vertical velocity variance between two 5-m levels in the tower array are computed. For this purpose, we recompute $\overline{w'^2}$ from a short running mean window of 10 seconds, sequentially advanced 1 second between calculations. The choice of the 10-second window width for computing $\overline{w'^2}$ is based on a typical time-scale of turbulence eddies and the minimum between-tower advective time-scale (τ^*) based on the mean hourly wind speed. Recall that the peak of composited w spectra occurs at time scales of a few seconds (Section 2.4). The mean hourly wind speed becomes as high as 8 ms^{-1} at the 5-m level, which translates into the advective time τ^* of 12.5 seconds for the minimum tower separation distance of 100 m. Increasing the window width beyond 12.5 seconds for including contribution of larger turbulence eddies in the computed $\overline{w'^2}$ would allow eddies to simultaneously encompass both towers, in which case advection no longer controls the computed cross-correlation coefficients.

The cross-correlation coefficients of $\overline{w'^2}$ are calculated every qualifying hour for 5-m levels on pairs of towers among the 3 sets of aligned towers: Towers 1, 6 and main tower; Towers 2, 5 and main tower; Towers 3, 4 and main tower. We consider only data when the wind direction is $\pm 22.5^\circ$ with respect to the axis of

the towers for 80% of the time within an hour. The number of hours in which the wind direction aligned with the third tower group (Towers 3, 4 and main tower) is small, thus no further analysis is performed for this tower group. Note that only wind direction centered at 65° is considered for the first tower group to avoid flow through the tower.

The time lag is converted to pseudo-distance by multiplying by the hourly mean wind speed. The variation of the composited cross-correlation coefficients for the combination of Towers 2, 5 and the main tower 5-m level in the northerly wind direction (5°) plotted against the pseudo-distance (Fig. 2.10) indicates that the sign of the maximum cross-lag correlation coefficient occurs in the sense consistent with advection of $\overline{w'^2}$. Here, the sign of the pseudo-distance originates from the time lag applied between a given pair of towers shown on each panel. The positive (negative) sign indicates that the signature at the first (second) tower lags at the the second (first) tower. A similar result occurs for the wind directions of 65° and 185° (Fig. 2.11). The maximum cross-lag correlation coefficient between a pair of towers is relatively small, and decreases with their separation distance. This result could imply significant evolution or decay of turbulent eddies as the eddies are advected across the domain. Referring to the time-scales discussed in Section 2.5, the between-tower advective time-scale τ^* appears to be larger or the same order of magnitude compared to the lifetime of a patch of turbulence, τ. Therefore, tracking such turbulent patches with data collected at separation distances of 100 m or more generally becomes ambiguous.

The peak of the cross-correlation coefficients occurs systematically at a pseudo-distance shorter than the physical separation distance between each pair of towers. There are a few possible reasons for inapplicability of the Taylor's frozen turbulence hypothesis. First, turbulence evolves or decays significantly as it is ad-

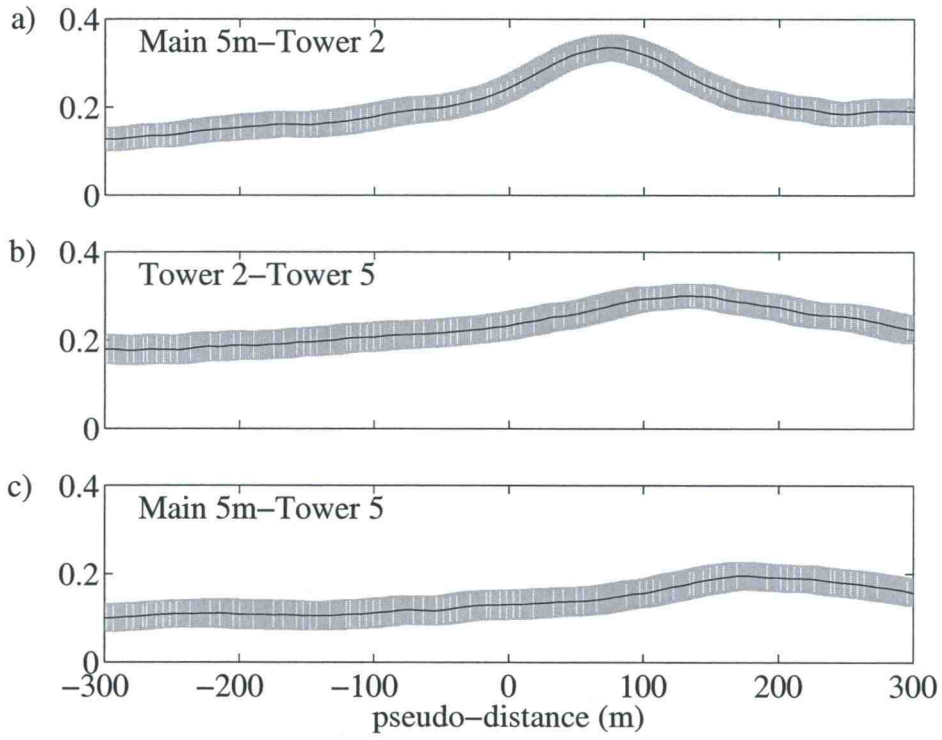

FIGURE 2.10. Composited cross-correlation coefficients computed from $\overline{w'^2}$ as a function of pseudo-distance for hours with northerly wind. The grey area below and above the dark lines indicate the standard error. The total number of hours included for the composites are 45, 46 and 45 hours for a), b) and c), respectively.

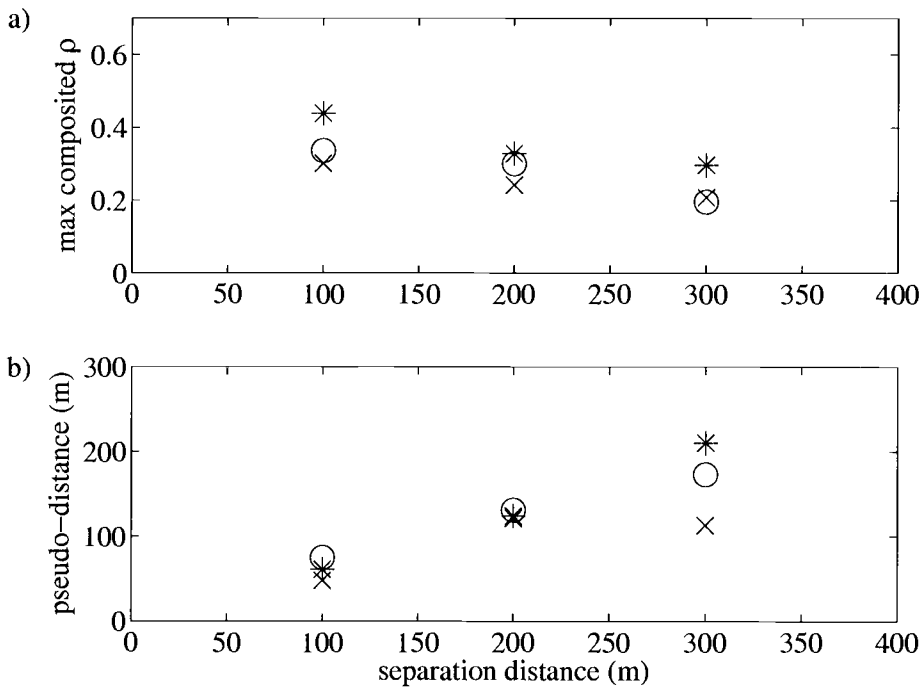

FIGURE 2.11. a) Maximum value of composited cross-correlation coefficients between two towers in each tower combination as a function of the separation distance between the two towers. ○: MT 5m-Tower 2-Tower 5 (wind direction: 5 °), ×: MT 5m-Tower 2-Tower 5 (185 °), ∗: MT 5m-Tower 1-Tower 6 (65 °) b) Pseudo-distance at which the maximum value of composited cross-correlation coefficient occurs as a function of the actual separation distance of the two towers.

vected from one tower to the next. Second, turbulence might have propagated horizontally by different means than advection such as a propagation of a parent disturbance, which continuously generates new turbulence. Third, the time-lag was converted to distance with the hourly mean wind speed so that the conversion to distance assumes that wind direction and speed are constant during the hour.

Finally, the same cross-correlation analysis above is repeated by decreasing the window width to smaller than 10 seconds for computing $\overline{w'^2}$. Reducing the window width decreases the maximum of the composite cross-correlation coefficients, indicating more rapid evolution and decay of smaller turbulence eddies.

2.9. Conclusions

The onset of an intermittent turbulence event was defined in terms of a rapid increase of vertical wind velocity fluctuations with time. When the between-tower advective time-scale (τ^*) is not small compared to the lifetime of a turbulence event (τ), the event cannot be observed at more than one tower, at least in a similar phase of development or decay. This was frequently the case for the present data where the tower spacing was 100 - 300 m. When the time-scale for the turbulent patch to pass by a tower (τ') is smaller than the patch lifetime (τ), a necessary condition for Taylor's frozen turbulence hypothesis, a patch of turbulence observed at the tower is considered to have been advected past the tower. This case is opposite to the assumption that the evolution and decay of turbulence can be studied from an individual tower.

In most cases, none or only a subset of 5m-levels on the satellite towers experience intermittent turbulence events concurrent with ones at the 5m-level on the main tower. While the spatial extent of intermittent turbulence events is generally

small, the intermittent turbulence events could sometimes be associated with larger-scale parent disturbances (Sun et al. 2002). Visual inspection of the present data indicates that turbulence was sometimes induced near the surface in phase with wave-like motions at higher levels on the main tower.

Modest values of the lagged cross-correlation indicates that horizontal advection of turbulence was important but suggests that the turbulence generally evolved or decayed significantly as it was advected from one tower to another. These statistics and animated pictures of the vertical turbulent motions on the tower and across the array suggest that tracing a patch of turbulence across the network was generally ambiguous. A denser tower network may be desirable for investigating evolution of individual intermittent turbulence events.

The gradient Richardson number often did not decrease to near or below 0.25 immediately before or during the onset of intermittent turbulence events for a number of possible reasons outlined in Section 2.7 including horizontal advection. The order of magnitude of the terms in the TKE budget was assessed for individual intermittent turbulence events at the main tower 5-m level. The vertical shear-generation term was the major source of TKE. The dissipation term was the major sink term. The buoyancy destruction of turbulence was typically 20 - 30% of the vertical shear-generation term. The advective term became an important sink term in some cases. The vertical turbulent transport of TKE was negligible.

Based on CASES-99 data and inspection of a number of other data sets not reported here, isolated and well-defined intermittency (Fig. 2.1 a - b) is rather rare. Intermittent geophysical turbulence is complex. Therefore, quantitative results can be sensitive to the mathematical definition and associated thresholds required to extract intermittent turbulence events. The above results also indicate that

very small changes in surface elevation can significantly change the statistics of intermittent turbulence.

2.10. Acknowledgements

The authors to wish to thank Dr. Don Lenschow for his extensive comments and suggestions for improving the original manuscript. The present research is supported by Grant DAAD19-9910249 from the Army Research Office and Grant 0107617-ATM from the Physical Meteorology Program of the National Science Foundation. The first author also wishes to acknowledge the Amelia Earhart Fellowship of the Zonta International Foundation.

2.11. References

Abarbanel, H.D.I., D.D. Holm, J.E. Marsden, and T. Ratiu, 1984: Richardson number criterion for the nonlinear stability of three-dimensional stratified flow, *Phys. Rev. Lett.* **52**, 2352-2355.

Atlas, D., J.I. Metcalf, J.H. Richter, and E.E. Gossard, 1970: The birth of "CAT" and microscale turbulence, *J. Atmos. Sci.* **27**, 903-913.

Blackwelder, R.F., and R.E. Kaplan, 1976: On the wall structure of the turbulent boundary layer, *J. Fluid Mech.* **76**, 89-12.

Blumen, W., 1984: An observational study of instability and turbulence in nighttime drainage winds, *Boundary-Layer Meteorol.* **28**, 245-269.

Coulter, R.L., 1990: A case study of turbulence in the stable nocturnal boundary layer, *Boundary-Layer Meteorol.* **52**, 75-91.

Coulter, R.L., and J.C. Doran, 2002: Spatial and temporal occurrence of intermittent turbulence during CASES-99, *Boundary-Layer Meteorol.* **105**, 329-349.

Drazin, P.G., 1977: On the instability of internal gravity wave, *Proc. R. Soc. Lond. A.* **356**, 411-432.

Edson, J.B., and C.W. Fairall, 1998: Similarity relationship in the marine atmospheric surface layer for terms in the TKE and scalar variance budgets, *J. Atmos. Sci.* **55**, 2311-2328.

Finnigan, J.J., 1988: Kinetic energy transfer between internal gravity waves and turbulence, *J. Atmos. Sci.* **45**, 486-505.

Finnigan, J.J., and F. Einaudi, 1981: The interaction between an internal gravity wave and the planetary boundary layer. Part II: effect of the wave on the turbulence structure, *Quart. J. Roy. Meteorol. Soc.* **107**, 807-832.

Grisogono, B., 1994: A curvature effect on the critical Richardson number, *Croatian Meteorol. J.* **29**, 43-46.

Howell, J.F., and L. Mahrt, 1997: Multiresolution flux decomposition, *Boundary-Layer Meteorol.* **83**, 117-137.

Howell, J.F., and J. Sun, 1999: Surface-Layer fluxes in stable conditions, *Boundary-Layer Meteorol.* **90**, 495-520.

Katul, G.G., J. Albertson, M. Parlange, C-R Chu, and H. Stricker, 1994: Conditional sampling, bursting, and the intermittent structure of sensible heat flux, *J. Geophys. Res.* **99**, 22869-22876.

Kim, J., and L. Mahrt, 1992: Simple formulation of turbulent mixing in the stable free atmosphere and nocturnal boundary layer, *Tellus* **44A**, 381-394.

Kondo, J., O. Kanechika, and N. Yasuda, 1978: Heat and momentum transfers under strong stability in the atmospheric surface Layer, *J. Atmos. Sci.* **35**, 1012 - 1021.

Kunkel, K.E., and D.L. Walters, 1982: Intermittent turbulence in measurements of the temperature structure parameter under very stable conditions, *Boundary-Layer Meteorol.* **22**, 49 - 60.

Lilly, D.K., 1983: Stratified turbulence and the mesoscale variability of the atmosphere, *J. Atmos. Sci.* **40**, 749 - 761.

Lyons, R., H.A. Panofsky, and S. Wollaston, 1964: The critical Richardson number and its implications for forecast problems, *J. Appl. Meteorol.* **3**, 136 - 142.

Mahrt, L., 1985: Vertical structure and turbulence in the very stable boundary layer, *J. Atmos. Sci.* **42**, 2333-2349.

Mahrt, L., 1989: Intermittency of atmospheric turbulence, *J. Atmos. Sci.* **46**, 79-95.

Mahrt, L., and S. Larsen, 1982: Small scale drainage front, *Tellus* **34**, 579-587.

Mahrt, L., and D. Vickers, 2002: Contrasting vertical structures of nocturnal boundary layers, *Boundary-Layer Meteorol.* **105**, 351-363.

Majda, A.J., and M.G. Shefter, 1998: Elementary stratified flows with instability at large Richardson number, *J. Fluid Mech.* **376**, 319-350.

Nappo, C. J., 1991: Sporadic breakdowns of stability in the PBL over simple and complex terrain, *Boundary-Layer Meteorol.* **54**, 69-87.

Nappo, C. J., 2002: *An introduction to atmospheric gravity waves* Academic Press. pp. 276.

Narasimha, R., and S.V. Kailas, 1990: Turbulent bursts in the atmosphere, *Atmos. Environ.* **24A**, 1635-1645.

Poulos, G.S., W. Blumen, D.C. Fritts, J.K. Lundquist, J. Sun, S.P. Burns, C. Nappo, R. Banta, R. Newsom, J. Cuxart, E. Terradellas, B. Balsley, and M. Jensen, 2002: CASES-99: A comprehensive investigation of the stable nocturnal boundary layer, *Bull. Amer. Meteor. Soc.*, **83**, 555-581

Riley, J.J., R.W. Metcalfe, and M.A. Weissman, 1981: Direct numerical simulations of homogeneous turbulence in density-stratified fluids, In *Nonlinear properties of internal waves.*, West, B.J., Editor, American Institute of Physics, New York, 79-112.

Sun, J., S.P. Burns, D.H. Lenschow, R. Banta, R. Newsom, R. Coulter, S. Frasier, T. Ince, C. Nappo, J. Cuxart, W. Blumen, X. Lee, and X-Z Hu, 2002: Intermittent turbulence associated with a density current passage in the stable boundary layer, *Boundary-Layer Meteorol.* **105**, 199-219.

Thorpe, S.A., 1973: Turbulence in stably stratified fluids: a review of laboratory experiments, *Boundary-Layer Meteorol.* **5**, 95-119.

Vickers, D., and L. Mahrt, 2003: The cospectral gap and turbulent flux calculations, *J. Atmos. Oceanic Technol.* **20**, 660-672.

Woods, J.D., 1969: On Richardson's number as a criterion for laminar-turbulent-laminar transition in the ocean and atmosphere', *Radio Science* **12**, 1289 - 1298.

3. AIR TEMPERATURE MEASUREMENT ERRORS IN NATURALLY VENTILATED RADIATION SHIELDS

Reina Nakamura and Larry Mahrt

To appear in *Journal of Atmospheric and Oceanic Technology*,

American Meteorological Society, Boston, U.S.A.

3.1. Abstract

Two sources of systematic errors are considered for estimating air temperature. The first source is ambiguity of the definition of the standardized measurement height over vegetated surfaces of varying height. Without such a standardization evaluation of the horizontal air temperature gradient is contaminated by the vertical variation of air temperature. This error is generally small in daytime unstable conditions, but increases with increasing stability at night. In an attempt to reduce such error, we propose the use of the zero-plane displacement height for standardizing the measurement height.

The second source of systematic errors is radiative forcing on the sensor-shield systems. A series of experiments are performed over a grass field to investigate the radiatively-induced error in the air temperature estimate by the Onset HOBO Pro thermistor in a naturally ventilated multi-plate shield. The magnitude of this error is estimated by comparing with air temperature measurements by a platinum RTD sensor in a mechanically aspirated shield. In contrast to the errors due to the first source, the radiatively-induced error increases with increasing instability. An empirical model is developed for correcting the radiatively-induced temperature error using information on wind speed and net or shortwave radiation. The robustness of the model is examined with independent data.

3.2. Introduction

With advancement in technology, both temperature sensors and data loggers have become less expensive, less-power consuming, portable, robust and reliable for long-term field deployment. To minimize the influence of shortwave radiation and longwave radiative exchange, a temperature sensor needs to be enclosed in a

radiation shield. While an ideal radiation shield would be mechanically aspirated, the cost and power requirements of such systems remain prohibitively high for most long-term network deployments.

A mechanically aspirated radiation shield is often replaced by a naturally ventilated radiation shield in such observational networks. When radiative forcing on the radiation shield is large and the ambient wind is weak, ventilation becomes inadequate to avoid significant radiatively-induced air temperature errors (e.g., Tanner et al., 1996; Anderson and Baumgartner, 1998; Richardson et al., 1999; Lin et al. 2001b; Erell et al., 2005). These errors need to be assessed for correctly interpreting air temperature data collected in a naturally ventilated shield. For example, if sensor-shield systems within a network of air temperature measurements experience different radiative forcing, e.g. due to variable cloudiness or exposure differences, the horizontal temperature gradient may be incorrectly estimated due to spatial variation of errors. In addition, when air temperature measurements are used to evaluate the sensible heat flux from the surface with the bulk-transfer method, the radiative error could cause significant errors in the predicted sensible heat flux and even the wrong sign (Anderson and Baumgartner, 1998; Arck and Scherer, 2001).

The HOBO Pro Data Logger (Model H08-031-08, Manufacturer: Onset Computer Corporation) and its external thermistor (Whiteman et al., 2000) enclosed in a naturally ventilated multi-plate radiation shield is one of the practical and economical systems for long-term air temperature monitoring. The HOBO logger and thermistor are durable for the outdoor environments, require minimal power and operate with relatively high accuracy. In this study, the radiatively-induced error of air temperature measurements (radiative error hereafter) by this thermistor in a multi-plate shield is investigated and a correction formula is constructed. Before examining the radiative error, we first investigate ambiguity of the definition of

the standard measurement height over vegetation of varying height as a source of systematic errors on air temperature.

3.3. Standardizing the Height of Air Temperature Measurements

Even with perfect instrumentation, air temperature measurements are often characterized by a certain degree of ambiguity due to uncertain interpretation of the influence of the upwind heterogeneity of the surface on the temperature measurement and by uncertain choice of measurement height above vegetated surfaces. We examine the ambiguity of air temperature measurements of the latter kind. A standard measurement height may be defined without ambiguity over flat terrain with bare soil or very short uniform vegetation. However, when the ground surface is covered by non-uniform vegetation such as grass, shrubs and trees, the definition of the standard height may become ambiguous. For example, it is not meaningful to compare air temperature at $1m$ above bare ground with a second air temperature at $1m$ above the ground surface, but only slightly above the top of the vegetation.

A representative measurement of air temperature is best made in the surface layer above the influence of horizontal variation of mean temperature on the horizontal scale of the roughness elements; that is, above the roughness sublayer (e.g. Kaimal and Finnigan, 1994). Within the surface layer, the height-dependence of air temperature is governed by turbulent momentum and heat fluxes according to Monin-Obukhov similarity theory such that (Brutsaert, 1982)

$$\overline{\theta} = \overline{\theta}_s - \frac{\overline{w'\theta'}}{\alpha_h \kappa u^*}[ln(\frac{z - d_o}{z_{oh}}) - \psi_h(\frac{z - d_o}{L})] \tag{3.1}$$

where $z, \overline{\theta}, \overline{\theta}_s, \overline{w'\theta'}, \alpha_h, \kappa, u^*, d_o, z_{oh}, \psi_h$ and L are the measurement height above the ground surface, the mean potential air temperature at height z, the aerodynamic surface temperature, sensible turbulent heat flux, the ratio of the eddy diffusivity for

heat to that for momentum (taken to be unity for this study), the von Karman constant, the friction velocity, the zero-plane displacement height, the roughness length for sensible heat, a stability function for sensible heat transfer, and the Obukhov length. The friction velocity is defined as (Stull, 1988)

$$u^* = (\overline{u'w'}^2 + \overline{v'w'}^2)^{\frac{1}{4}} \tag{3.2}$$

where $\overline{u'w'}$ and $\overline{v'w'}$ indicate the vertical turbulent momentum flux in along and cross-wind directions.

The Obukhov length is defined as

$$L = -\frac{\overline{\theta_v} u^{*3}}{\kappa g \overline{w'\theta_v'}} \tag{3.3}$$

We use the ψ-stability function in Brutsaert (1982).

We propose the standard measurement height to be a fixed height above the displacement height d_o, not above the ground surface, in order that the relative vertical variations of the mean temperature do not contaminate the estimation of the horizontal variations. The variable height of the sensor above the ground surface is

$$z = Z + d_o \tag{3.4}$$

where Z is the pre-scribed fixed height of the sensor above the variable displacement height. The displacement height, d_o depends in part, on the way the drag force is distributed through foliage (Kaimal and Finnigan, 1994). The displacement height has been related to the roughness density (Raupach, 1994). At the same time, prediction of the displacement height, d_o based only on the canopy architecture remains uncertain (Monteith and Unsworth, 1990). As a rule of thumb, for uniform vegetation, one might use 2/3 - 3/4 of the vegetation height (Parlange and Brutsaert,

1989; Jones, 1992) although much smaller values may be more suitable for sparse canopies. In practice, the displacement height, d_o must be estimated from profiles and/or eddy-correlation measurements (e.g. De Bruin and Moore, 1985). However, even with such measurements, there is no general agreement on the precise method for estimating the displacement height. In many studies, neither the profiles nor eddy-correlation data are available. The estimated displacement height, $d_{o\ estimated}$ can be expressed as

$$d_{o\ estimated} = d_o + d_{o\ error} \tag{3.5}$$

where $d_{o\ error}$ denotes the uncertainty in the estimated displacement height including failure to account for growing vegetation. The temperature sensor is deployed at

$$z = d_{o\ estimated} + Z = d_o + Z + d_{o\ error} \tag{3.6}$$

Thus, the error in the displacement height, $d_{o\ error}$ directly translates into deviation of the measured temperature from the required temperature at the standard height Z above the true displacement height, d_o (Fig. 3.1).

Using Eq. 3.1, the error in the estimated air temperature measurement for the standard height, Z, can be written as

$$\begin{aligned}\overline{\theta}(Z + d_{o\ estimated}) - \overline{\theta}(Z + d_o) = -\frac{\overline{w'\theta'}}{\alpha_h \kappa u^*}[ln(\frac{Z + d_{o\ error}}{z_{oh}}) - ln(\frac{Z}{z_{oh}}) \\ -\psi_h(\frac{Z + d_{o\ error}}{L}) + \psi_h(\frac{Z}{L})]\end{aligned} \tag{3.7}$$

To illustrate the influence of an inappropriately estimated zero-displacement height on the measured air temperature, a heuristic exercise is performed with sonic anemometer data from the FLux Over Snow Surface II (FLOSS II) (Mahrt and Vickers, 2005). We analyze eddy-correlation data collected at $2m$ above the ground surface where the average height of the sparse brush is $h_{avg} = 0.3\ m$ although the

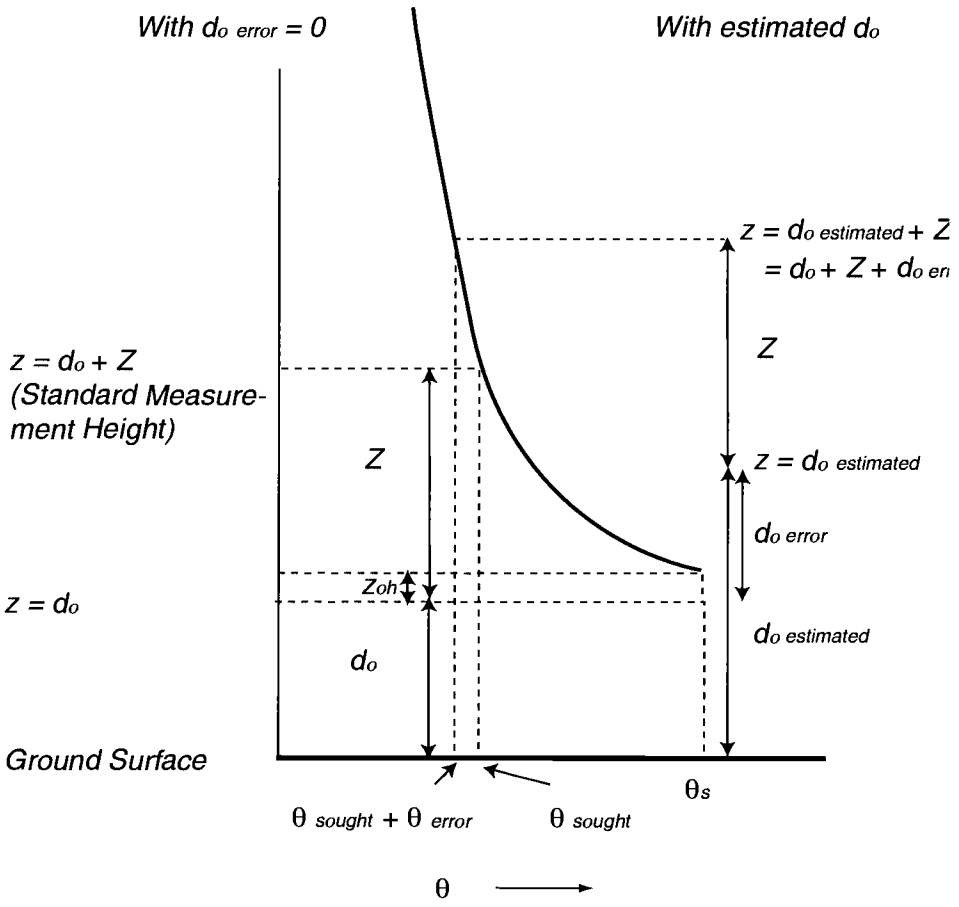

FIGURE 3.1. Illustration of an unstable vertical temperature profile in the atmospheric surface layer. Estimated displacement height $d_{o\ estimated}$ is shown as $d_o + d_{o\ error}$. θ indicates potential temperature. θ_s indicates the aerodynamic surface temperature.

actual height of the brush varies between 0.2 m and 0.6 m. The data were collected at 20 Hz at $2m$ above the ground surface ($z = 2m$). Turbulent heat and momentum fluxes are computed with an averaging window of 150 *secs*. The flux data are averaged over one hour to reduce random flux sampling errors. No data are analyzed for the transition periods (0700-1000 LST, 1500-1800 LST) to avoid the influence of nonstationarity. The thermal roughness length (z_{oh}) is set equal to the momentum roughness length ($z_{om} = 0.039\ m$), where the latter is determined in near-neutral conditions. As with most data sets, we cannot confidently estimate the displacement height, but can only show sensitivity of the measured air temperature at $Z + d_o$, to the estimated displacement height, $d_{o\ estimated}$. As an instructive example, we consider $d_o = \frac{1}{2}h_{avg} = 0.15m$ as a plausible displacement height for a sensitivity calculation.

The air temperature error for a measurement height, $Z = 1.85m$ ($Z + d_o = z = 2m$) is simulated with Eq. 3.7 for a range of errors in the estimated displacement height (Fig. 3.2). For this sensitivity exercise, the maximum positive value of the estimated displacement height is 2/3 of the maximum vegetation height, $h_{max} = 0.6\ m$. This range of the estimated displacement heights changes the temperature measurement as much as 0.2 ^oC in stable conditions, but much less for unstable conditions. This temperature error can, for example, lead to large errors in the horizontal advection computed over small distances (Ha and Mahrt, 2003) or in the surface sensible heat flux computed with the bulk-transfer method. The air temperature measurement error can become even larger if the plausible range of the displacement height estimate increases due to an increase in the range of vegetation height. Because the vertical gradients increase toward the "surface, the problem of the incorrectly estimated displacement height becomes more serious for measurements closer to the surface.

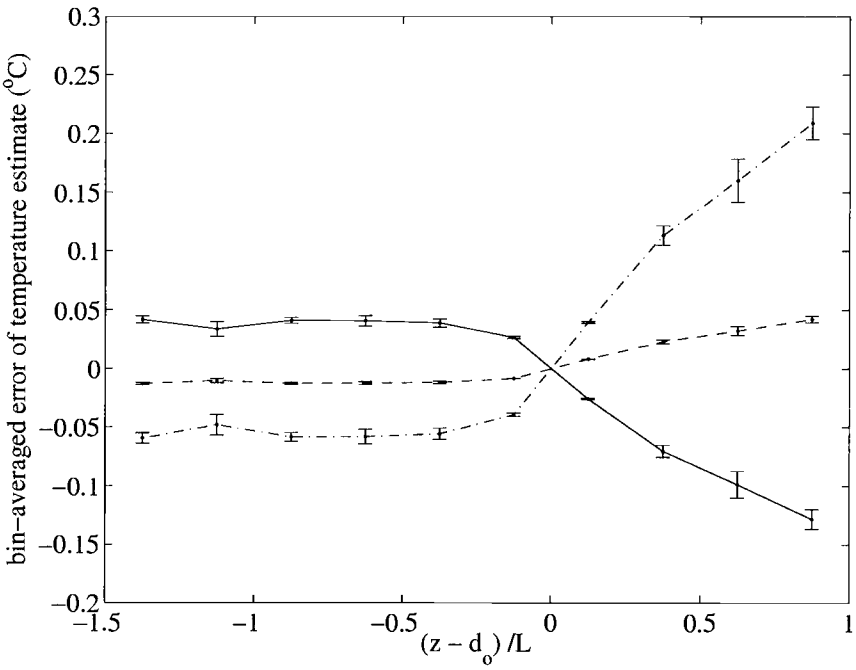

FIGURE 3.2. Simulated bin-averaged error in estimated temperature for $z = Z + d_o + d_{o\ error}$ due to non-zero $d_{o\ error}$ as a function of stability for various errors in the displacement height. Z is set to $1.85m$. The bin width in $(z - d_o)/L$ is 0.25. The vertical bars indicate the standard error within each bin. The true displacement height, d_o, is 0.15 m in this exercise. Solid line: $d_{o\ error}$ = -0.15 m ($d_o + d_{o\ error} = 0m$), dashed line: $d_{o\ error} = 0.05\ m$ ($d_o + d_{o\ error} = 2/3h_{avg} = 0.2m$), dash-dot line: $d_{o\ error} = 0.2\ m$ ($d_o + d_{o\ error} = 2/3h_{max} = 0.45m$)

The air temperature errors due to the height uncertainty limit the advantage of expensive aspirated sensor-shield systems. Thus, an accurate estimate of the displacement height for a vegetated surface is important, which suggests a need for an improved methodology to estimate the displacement height particularly over non-uniform vegetation.

3.4. Instrumentation and Data

The details of instrumentation used in our field experiments are summarized in Table 3.1. The HOBO Pro Data Logger (Model H08-031-08) is a two channel logger equipped with two thermistors: an internal thermistor and an external thermistor connected by the logger unit with a 1.7-m cable. The manufacturer's specification states that the HOBO logger with a replaceable small lithium battery is able to operate continuously for up to 3 years unless operated at very low temperatures. In this study, we use only the external thermistor (the HOBO thermistor hereafter). Our indoor experiments determined the time constant of the HOBO thermistor in still air to be 180 *secs*, between that reported by the manufacturer's specification (270 *secs*) and by Whiteman et al. (112 *sec*). With mechanical aspiration of 3 - 7 ms^{-1}, however, the time constant of the HOBO thermistor improves to approximately 26 *secs*.

The present study investigates radiative errors in the mean air temperature over 30-min periods estimated by the HOBO thermistor operating in a high resolution mode in an outdoor field situation. The thermistor is enclosed in the naturally ventilated multi-plate shield manufactured by Davis Instruments (Model 7714). This multi-plate shield is also known as solar radiation shield RS1 of Onset Computer

TABLE 3.1. Summary of instrumentation

Sensors	Manufacturer and Model #	Manufacturer's Specification
Thermistor and logger	Onset, 08-021-08	*Thermistor* dimension: $5mm$ (dia), $30mm$ (ht) time constant: 270 s accuracy: $\pm$ 0.2 ^oC *Logger* time drift $\pm 100min$ per week at 20 ^oC
Platinum RTD	RM Young, 43347	dimension: $3.2mm$ (dia), $57mm$ (ht) time constant: 42 s with aspiration accuracy: $\pm$ 0.1 ^oC
Aspirated radiation shield	RM Young, 43408	Air flow rate 3 - 7 ms^{-1} depending on sensor size Radiation error: $< 0.2^oC$ at 1100 Wm^{-2}
2-D sonic anemometer	Vaisala, WS425	resolution: 0.1 ms^{-1} accuracy: $\pm$ 0.135 ms^{-1}
Net radiometer	Kipp and Zonen, CNR1	response time: 18 s spectral response: 305-2800 nm (pyranometer), 5,000-50,000 nm (pyrgeometer) pyranometer error: < 25 Wm^{-2}
Silicon pyranometers	Licor, Li-200S	response time: $10\mu s$ spectral response: 400-1100 nm error in natural daylight: $\pm 3\%$
Infrared transducers	Apogee, URTS-P5	response time: < 1 s accuracy: $\pm$ 0.2 ^oC
Type-E thermocouple	Campbell, FW3	0.076 mm respone time: a few ms

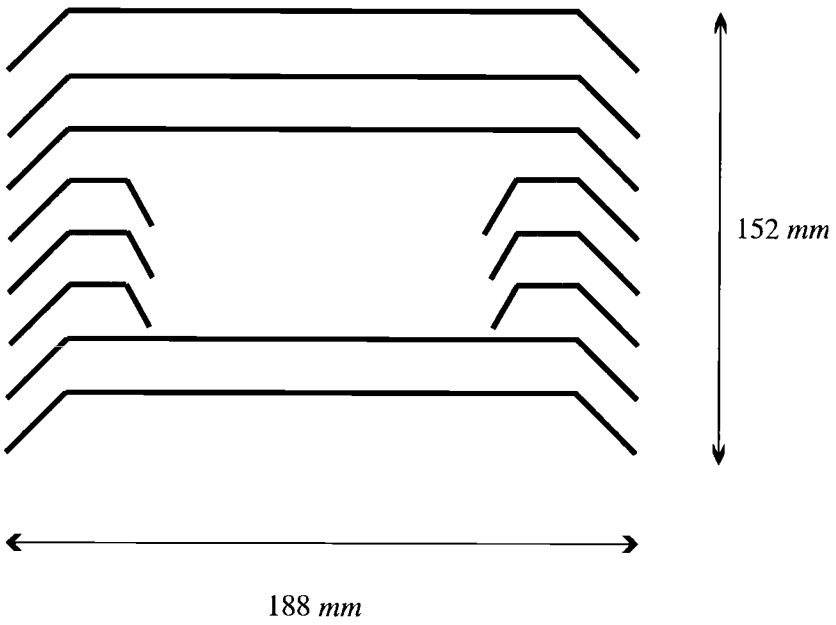

FIGURE 3.3. Cross section of Davis Instruments multi-plate shield Model 7714 (Onset Computer Radiation Shield RS1). Dimension of the shield is $188mm(l) \times 213mm(d) \times 152mm(h)$. Individual plates are $3mm$ thick. All the plates are separated by $15mm$ except for the top two separated by 20 mm. The vertical overlap between a plate and the one underneath is 4 mm.

Corporation (Fig. 3.3). A sampling interval of 300 *secs* is selected for the HOBO thermistor, which allows the logger to collect data for 3 - 4 months.

Data were collected above a flat grassland (latitude: 44′ 38″, longitude: 123 ′12″ west) in the spring and summer of 2002 and in the summer of 2003. As basic datasets (Datasets A and B), air temperature was measured by 1) a HOBO thermistor in the Davis multi-plate shield and 2) a platinum RTD (Resistance Temperature Detectors) sensor in a mechanically aspirated shield (RM Young, Model 43408),

TABLE 3.2. Summary of data collection. Height is above the ground surface unless otherwise noted. MS and MAS stand for multi-plate shield and mechanically aspirated shield, respectively.

Dataset ID	Dates	Data Type		Height(m) /position
A	March 14 - Aug 30, 02	Air temperature	HOBO thermistor in MS	1
			RTD in MAS	1
		Wind speed/direction		1
		4-component radiation		1.5
B	July 15 - Aug 30, 03	Same as Dataset A		
C	July 30, 03	Downward shortwave irradiance in MS	grass	0.025 from MS inner bottom
	Sept 01, 03		black tarp	
	Sept 01, 03		white tarp	
	Aug 13, 03	Upward shortwave irradiance in MS	grass	0.035 from MS inner bottom
	Sept 02, 03		black tarp	
	Sept 02, 03		white tarp	
D	July 15 - Aug 30, 03	MS surface temperature	Infrared transducers	MS outer top and bottom
			thermocouple	MS outer top

both at $1m$ above the ground surface. The horizontal separation distance between the two sensors was approximately 1.5 m. In addition, wind speed, wind direction and upward and downward components of shortwave and longwave radiation were measured. Table 3.2 summarizes these data and other datasets acquired during the field experiment, which are analyzed in later sections.

All the data except for the HOBO thermistor measurements, were logged at 0.5 Hz by Campbell Scientific CR23X data logger in 2002 and CR5000 data logger in 2003. All the temperature sensors were thoroughly intercompared at 0 $^{\circ}C$ in an ice-bath and at room temperature. Small offsets of individual sensors of less than a tenth of a degree Celsius are corrected for all the analyses below.

3.5. Sources of Radiative Errors

3.5.1. General Considerations

The energy balance on a temperature sensor consists of shortwave radiative forcing, longwave radiative exchange and sensible heat transfer between the sensor and the surrounding air. The radiative error can be often reduced by decreasing the sensor size (Campbell, 1969). However, the need for durability and economy in long-term field experiments generally requires the use of larger sensor size.

To minimize the influence of shortwave radiation and longwave radiative exchange with the surroundings such as clear sky and ground surface, the sensor is deployed within a radiation shield. An ideal naturally ventilated shield should prevent shortwave radiation from penetrating into the interior. The ray tracing study of Richardson et al. (1999) showed that shortwave radiation entering a multi-plate shield is mostly absorbed by the shield or sensor rather than exiting the sensor-shield system, thus contributing to the radiative error.

Deviation of the shield temperature from the air temperature can also become a source of radiative error in that it modifies the air temperature inside the shield by sensible heat transfer from the plates and modifies the sensor temperature by longwave radiative transfer. The shield temperature can be maintained closer to the air temperature by choosing appropriate material and coating for the shield (Fuchs and Tanner, 1965).

The sources of radiative error for the shield-sensor system are counteracted by increasing the degree of coupling of the air inside the shield to the ambient air. Unfortunately, increasing coupling requires wider separation distance between the shield plates and therefore more direct shortwave radiation into the shield interior

and possibly more longwave radiative exchange between the sensor and objects outside the shield.

3.5.2. Imperfect Shielding of Shortwave Radiation

The degree of shortwave radiation reaching inside a radiation shield may be represented as the mean shortwave radiation ratio, $\overline{S^*}$ (%), based on Hubbard et al. (2001), defined as

$$\overline{S^*} = 0.5(S^* \downarrow + S^* \uparrow) \tag{3.8}$$

where $S^* \downarrow$ and $S^* \uparrow$ are downward and upward shortwave radiation ratios (%), respectively, defined as

$$S^* \downarrow = \frac{Downward\ shortwave\ irradiance\ inside\ shield}{Downward\ global\ shortwave\ irradiance\ outside\ shield} \times 100 \tag{3.9}$$

and

$$S^* \uparrow = \frac{Upward\ shortwave\ irradiance\ inside\ shield}{Downward\ global\ shortwave\ irradiance\ outside\ shield} \times 100 \tag{3.10}$$

To estimate the downward and upward shortwave irradiance inside the Davis multi-plate shield during the daytime, a pair of Licor Li-200S Pyranometers were deployed inside the multi-plate shields (Dataset C). Since the vertical dimension of the space inside the shield is only 7.0 cm in height, only one pyranometer (2.5 cm height) is deployed within a shield at a time. Thus, downward and upward shortwave radiation within a particular shield was measured on separate days. Downward (upward) shortwave radiation measurements were made by an upward (downward) facing pyranometer situated at 2.5 cm (3.5cm) height above the next lowest plate. It was technically difficult to install a pyranometer at other heights without significantly blocking the path of the shortwave radiation. However, these measurement

heights of the pyranometers fall in the height range over which the HOBO thermistor inside a shield typically extends ($2.5cm$ - $6cm$ above the next lowest plate). The spectral distribution of shortwave radiation inside the multi-plate shield differs from that under direct shortwave radiation. The effect of altered spectral distribution is taken into account for the pyranometer data by adopting the calibration formula determined by Hubbard et al. (2001).

To investigate the influence of shortwave radiation reflected from the ground surface, pyranometers enclosed in the multi-plate shields were deployed over three surface types: the original grass, a black surface and a white surface. The black and white surfaces were created by a single black plastic sheet (0.08 mm thick) and by 8 layers of transparent sheets (each 0.025 mm think), respectively. The size of both sheets was $6m\times$ $6m$. The multi-plate shields were deployed in the center at $1m$ above the ground surface. The individual plates of the present multi-plate shield are rectangular (0.188 m $\times$ 0.213 m) so that the area-based equivalent square would be exactly 0.20 m on a side. Such a plate located at $1m$ above the ground receives 92% of the entire radiation from the ground surface of 6 $m\times$ 6 m if the surface is assumed to be a diffuse surface (Howell, 1982). A diffuse surface is defined as a surface that emits and/or reflects equal radiation intensity in all directions. The measured albedos of the black, grass and white surfaces are 0.08, 0.23 and 0.56, respectively.

Fig. 3.4a illustrates $\overline{S^*}$ over the grass, black and white surfaces. The $\overline{S^*}$ values are computed from $S^* \downarrow$ and $S^* \uparrow$ measured on two different cloudless days. Both ratios $S^* \downarrow$ and $S^* \uparrow$ reach maximum values at large solar zenith angles although the absolute magnitude of the shortwave radiation detected inside the shield at such zenith angles is at a minimum. Richardson et al. (1999) reported a similar finding in a numerical ray tracing study within a Gill multi-plate shield (Gill, 1979).

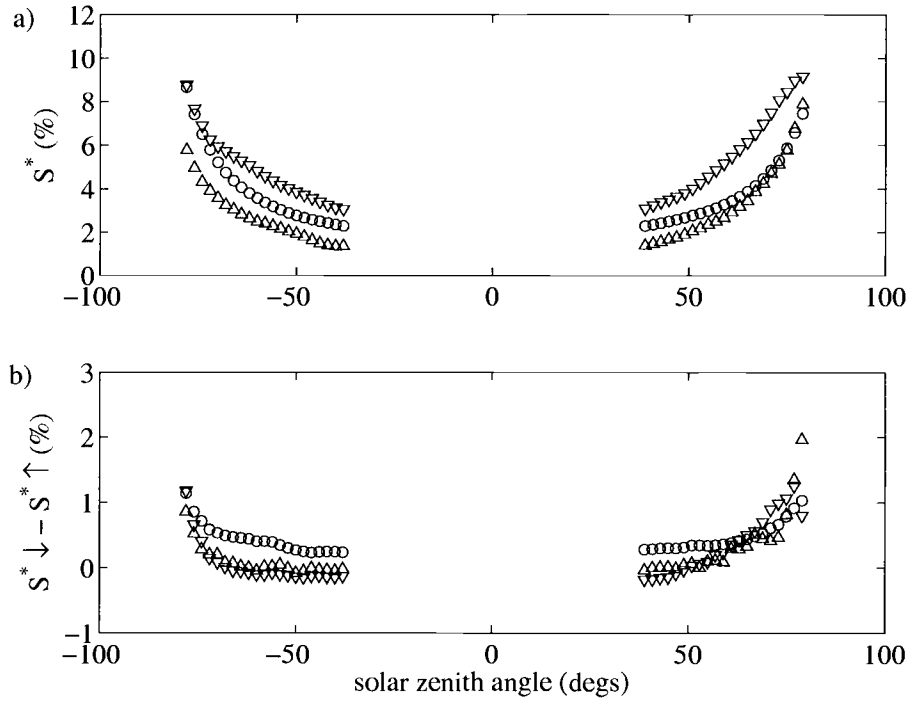

FIGURE 3.4. a) Mean shortwave radiation ratio, $\overline{S^*}$ (%) b) difference between the downward shortwave radiation ratio and the upward shortwave radiation ratio, $S^*\downarrow - S^*\uparrow$ (%) for grass-covered ($\circ$), black ($\triangle$) and white ($\bigtriangledown$) surfaces. Negative (positive) sign in the solar zenith angle indicates before (after) solar noon.

Shortwave radiation reaching inside the shield is positively correlated with surface albedo (Fig. 3.4a). The mid-day value of $\overline{S^*}$ becomes 1.4, 2.3 and 3.1 % for black, grass and white surfaces, respectively. $\overline{S^*}$ over the white surface is typically twice as large as that over the black surface except for high solar zenith angle. This result implies that a significant portion of shortwave radiation reaching inside the shield originates from shortwave radiation reflected from the ground surface. The radiative error due to the heating of the sensor by its absorption of shortwave radiation inside the present multi-plate shield likely increases with increasing albedo.

The difference between $S^* \downarrow$ and $S^* \uparrow$ is generally small except when the solar zenith angle exceeds about 70 ° (Fig. 3.4b). This result may indicate that a large portion of shortwave radiation detected inside the shield during mid-day may be diffuse rather than direct shortwave radiation. Richardson et al. (1999) argues that shortwave radiation reflected from imperfectly smooth shield plate surfaces yields diffuse radiation. A part of the difference between the observed $S^* \downarrow$ and $S^* \uparrow$ may also be attributed to the exact position of the pyranometer with respect to the shield structure (Hubbard et al., 2001).

3.5.3. Shield Surface Warming/Cooling

A shielded thermistor exchanges longwave radiative energy with the inner surface of the shield. However, we were able to measure only the temperature of the outer surface of the Davis multi-shield with existing instrumentation. We assume that the conductivity of the shield material is sufficiently high so that changes of the inner and outer surface temperatures of a given plate are highly correlated. An infrared transducer (Apogee IRTS-P5) is deployed directly above and underneath a multi-plate shield. In addition, a Type-E thermocouple is fixed to the top plate of

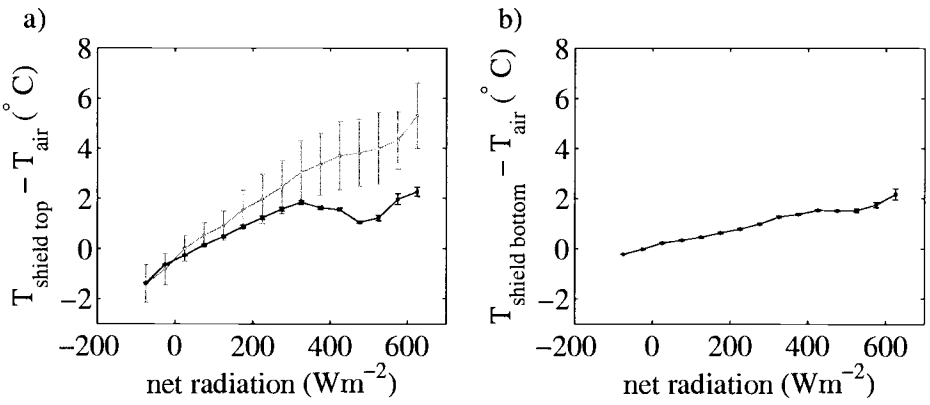

FIGURE 3.5. Bin-averaged deviation of the shield surface temperature from air temperature as a function of net radiation above the grass surface. The shield top temperature was simultaneously monitored by a thermocouple (gray) and an infrared transducer (black). Vertical bars indicate standard errors within bins.

another multi-plate shield located 0.7 m away from the first shield (Dataset D). For the true air temperature estimate, air temperature data from the aspirated RTD sensor of Dataset B are employed.

The shield-top temperature measured by the thermocouple and that measured by the IR transducer agree at night within a few tenths of a degree (Fig. 3.5). However, the thermocouple measurements become significantly larger than the IR transducer measurements during daytime. This difference may be explained by the combination of a self-shadowing effect of the IR transducer at low solar zenith angle and shortwave heating of the thermocouple wires. The actual shield-top daytime temperature is tentatively considered to be somewhere between these two estimates.

Since the outer surface of the shield is directly exposed to external radiation, the thermistor inside the multi-plate shield is expected to be much less influenced by external radiation than the outer surface. Therefore, the radiatively-induced

temperature excess or deficiency of the outer shield is expected to be substantially larger than the radiatively-induced thermistor error as verified in the next section.

3.6. Correction of Radiatively-Induced Temperature Errors

The radiative error due to radiative heating or cooling of the sensor is reduced by air flow past the sensor surface, which enhances sensible heat transfer between the sensor and surrounding air (Section 3.5.1). Rigorous correction of radiative errors may require radiation and air flow measurements inside the shield which are not necessarily linearly correlated with those outside the shield. Richardson et al. (1999) simulated flow in and around the Gill multi-plate shield and found that the flow efficiency, the fraction of the ambient wind speed detected inside, decreases with decreasing ambient wind speed, especially for ambient wind speed less than 1 ms^{-1}. To the contrary, the flow efficiency increased slightly when the ambient wind speed is reduced down to 0.5 ms^{-1} in laboratory and field studies with the Maximum-Minimum Temperature System (MMTS) multi-plate radiation shield (Lin et al., 2001a). The behavior of the flow efficiency as a function of the ambient wind speed appears to be quite complex and depends on the exact design of the multi-plate shield and even on the characteristic of the flow such as steadiness and turbulent intensity (Lin et al., 2001a). In practice, simpler procedures are desirable for routinely correcting the radiative error without explicitly assessing the flow efficiency. We attempt to pragmatically correct for the radiative error using only information on wind speed and shortwave or net radiation measurements made outside the shield.

The radiative error is often modeled in terms of low-Reynolds turbulent heat transfer between the sensor or the shield surface and the ambient atmospheric air

(e.g. Tanner, 1979; Anderson and Baumgartner, 1998; Erell et al., 2005). Unlike in laboratory settings, the turbulence responsible for the heat transfer between an obstacle and the atmosphere is normally strongly influenced by ambient high-Reynolds atmospheric turbulence in addition to turbulence induced by the obstacle, which may not be low-Reynolds turbulence as previously assumed. Atmospheric eddies larger than the length scale of the obstacle act like a time dependent mean wind imposed on the obstacle and its energy exchange with the atmosphere. Such eddies trigger transient internal boundary layers at the surface of the obstacle. The depth of the obstacle internal boundary layer is inversely related to the wind speed (Incropera and De Witt, 1990). Atmospheric eddies of the same size as the obstacle may distort or disrupt the obstacle internal boundary layer. Atmospheric eddies that are small compared to the obstacle have a dissipative influence on the turbulent eddies generated by the obstacle. Therefore, heat transfer between a sensor or shield and the atmosphere in fully developed turbulence cannot be exclusively related to the Reynolds number or molecular properties of the air flow as attempted in the past literature. However, heat transfer between the sensor surface and air within a multi-plate shield may be governed by low-Reynolds turbulence. The low-Reynolds turbulence is generated not only by the sensor itself but also by individual plates and plate spacers. Thus, characteristic length scales of these objects influence the heat transfer between the sensor surface and air inside the shield. We do not attempt to model these complex processes, but rather construct a simpler and more empirical approach.

3.6.1. HOBO Radiative Error

We assume that the radiative error for the RTD sensor in the mechanically aspirated shield is small compared to that for the HOBO thermistor. The difference between the HOBO and the mechanically aspirated RTD temperature measurements is considered to be the HOBO radiative error, which will be related to the ambient radiation and wind speed (Dataset A). An averaging interval of 30 *min* is selected for this study. The manufacturer's specification states that the shortwave radiation measurements by the CNR1 net radiometer (Table 3.1) are unreliable when the solar zenith angle is greater than 80°. Therefore, such data are discarded. We use scalar- rather than vector-averaged wind speeds over 30 *min* because the magnitude of the instantaneous wind speed, regardless of the wind direction, ventilates the sensor-shield system.

During the daytime, the HOBO radiative error becomes systematically positive with shortwave radiation (Fig. 3.6). At night, when the net radiation is negative, the HOBO radiative error generally becomes weakly negative. Thus, we attempt to correct the radiative errors separately for the daytime and nighttime periods. The radiative error is larger during the daytime with an average value of 0.39 $^{\circ}C$; the radiative error becomes larger than 0.5 $^{\circ}C$ and 1.0 $^{\circ}C$ for 22.9 % and 2.6 % of the daytime periods, respectively. The mean nocturnal radiative error is only -0.002 $^{\circ}C$, but the error increases systematically with increasing radiative forcing (Fig. 3.7 , Section 3.6.2). The radiative error becomes larger than -0.5 $^{\circ}C$ for only 4.6 % of the nocturnal periods.

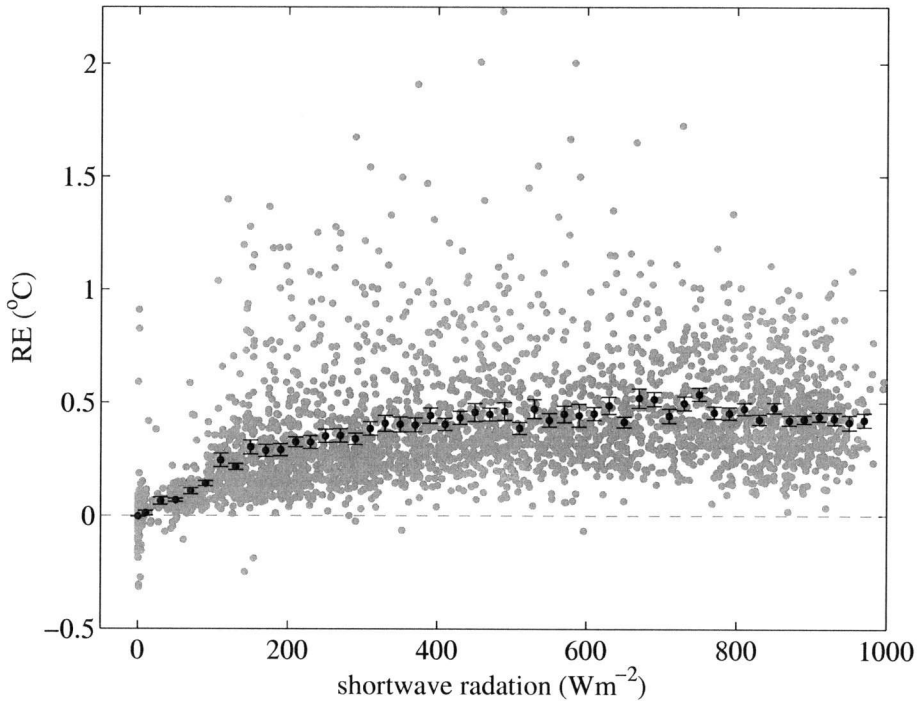

FIGURE 3.6. The original (gray circle) and bin-average values (black circle) of the HOBO radiative errors for all the data. The error bars indicate the standard errors. The bin width is 20 Wm^{-2} except all the HOBO radiative errors in shortwave radiation of 0 Wm^{-2} (nighttime) are averaged together.

3.6.2. Similarity Regression Model

We propose expressing the radiative error in terms of the ratio of the radiative forcing to the natural ventilation represented by the non-dimensional number,

$$X = \frac{Rad}{\rho C_p T_{HB} U} \tag{3.11}$$

where Rad (Wm^{-2}) indicates shortwave radiation and net radiation for the daytime and nocturnal periods, respectively. U is the wind speed (ms^{-1}); ρ is the density of air, taken to be 1.2 kgm^{-3} and C_p is the specific heat capacity of air at constant pressure, taken as 1004 $JK^{-1}kg^{-1}$. T_{HB} is the HOBO air temperature measurement expressed in K. The relationship between the radiative error, RE, and non-dimensional radiative forcing X is expressed as a polynomial function,

$$RE = C_0 + C_1 X + C_2 X^2 ... \tag{3.12}$$

where C_0, C_1 and C_2 are empirical coefficients that presumably depend on characteristics of the sensor-shield system and those environmental flow characteristics not included in X.

The radiative error correction is most needed when the wind is weak and radiative forcing is strong (Section 3.5.1), that is when X is large (Fig. 3.7). However, such conditions occurred less frequently than conditions with significant wind or cloudiness corresponding to smaller radiative errors. Therefore, to retain appreciable influence of cases with large X in the determination of the coefficients of the model in Eq. 3.12, the original 30-min data of the HOBO error are averaged for intervals or bins of the non-dimensional radiative forcing, X. The width of the bins is set to 1.25×10^{-4} and 2.5×10^{-5} for daytime and nighttime periods, respectively. These bin-widths yield approximately 20 bins. We require at least 5 data points within a bin for the averaging procedure. The result of the analysis

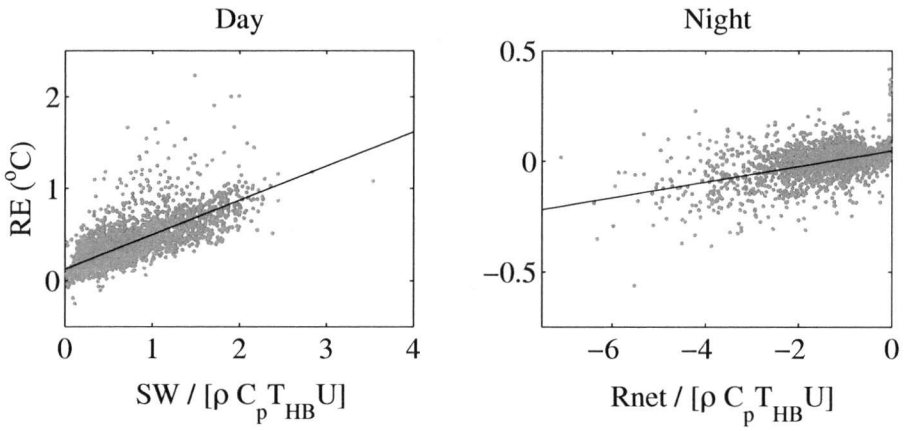

FIGURE 3.7. HOBO radiative error as a function of non-dimensional radiation forcing X. For display, the radiation forcing in the horizontal axes has been multiplied by 10^3 and 10^4 for day and night, respectively. SW and Rnet stand for shortwave and net radiation, respectively. Lines indicate regression lines based on the coefficients in Table 3.3.

below is insensitive to the exact width of the bin. Eq. 3.12 is regressed on the bin-averaged data.

The R-squared value, that is the fraction of variance explained by a model, always improves by adding more terms. Therefore, the statistical significance of the R-squared value is examined with the analysis of variance after each higher order term is added to the model (e.g. Chelton, 1983). The hypothesis that an additional term did not improve the true regression model is tested with the F test at the 95 percent confidence level by assuming that the individual bin-averaged data are statistically independent. The results indicate that adding higher order terms beyond the first order term does not improve the regression model with statistical significance. The R-squared value of the determined model is 0.98 and 0.94 for the daytime and nighttime, respectively. These values are much higher than the 95%

TABLE 3.3. Summary of determined coefficients for the similarity regression model for daytime and nighttime periods.

	Relevant radiation data	C_0	C_1
Day	shortwave	0.13	373.40
Night	net	0.047	355.84

critical values for the R-squared value of the model under the null hypothesis, 0.21 for daytime and 0.19 for nighttime.

The procedure adopted for determining the coefficients maximizes the R-squared value over the entire range of the radiative forcing, X, in terms of a linear fit. For both daytime and nighttime, the coefficients determined from this procedure (Table 3.3) yields a nonzero constant as the radiative forcing, X vanishes. The nonzero correction at $X = 0$ is therefore an artifact of the statistical fit. For nighttime, the nonzero constant is a few hundredths of a degree, sufficiently close to zero so that we apply the determined coefficients for correcting the HOBO air temperature measurements for the entire range of nighttime X. For daytime, Fig. 3.7 indicates that the fit suddenly breaks down for very small values of X less than 1.0×10^{-4} and we suggest that the small corrections for X less than 1.0×10^{-4} be neglected. The percentage of the neglected data corresponds to 3.1% of all the daytime data.

The regression model with the estimated coefficients is used to correct the original HOBO air temperature measurements. The radiative error is substantially reduced after the correction, especially in weak wind and sunny conditions (Fig. 3.8).

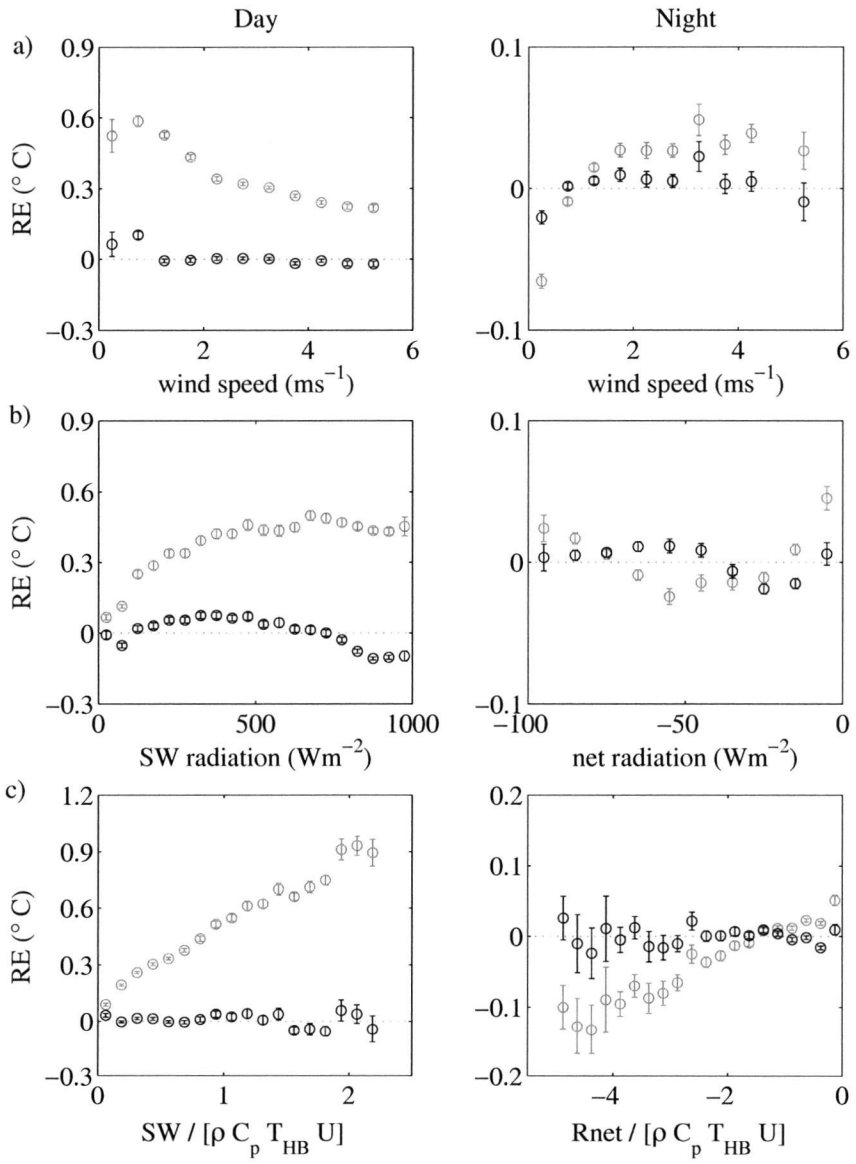

FIGURE 3.8. Bin-averaged HOBO radiative errors for 30-min mean air temperature as a function of a) wind speed, b) shortwave or net radiation and c) non-dimensional radiative forcing, X (Eq. 3.11) for daytime (left column) and nighttime (right column). For display, the radiation forcing in the horizontal axes has been multiplied by 10^3 and 10^4 for day and night, respectively. Gray and black HOBO errors indicate those before and after corrections (Eq. 3.12), respectively. The vertical bars indicate the standard error within each bin.

The correction reduces the mean and the root mean square errors in both periods, particularly in the daytime when the errors are larger (Table 3.4). For nocturnal periods, the model does not lead to significant improvement for the data set as a whole. This is because the nocturnal HOBO errors are dominated by $X > -3\times10^{-4}$ where the errors are random with near zero mean (Fig. 3.7).

The present model does not include all the physical processes affecting the radiative error, which partly accounts for the remaining error. For example, for a given ambient wind speed, the dependence of the flow rate in the shield on characteristics of the ambient wind (e.g. airflow steadiness and turbulence intensity) is not included in the model. As an additional example, change in the cloud-cover within the averaging time is not considered. Finally, the aspirated RTD sensor may also be subject to non-negligible errors.

3.6.3. Robustness of Model

The robustness of the error correction model and coefficients determined with Dataset A are now tested with Dataset B collected at the same site, but in the summer of 2003 (Table 3.2). The radiative errors are effectively reduced for Dataset B, indicated by the reduced mean and root mean square errors (Table 3.5). In spite of the fact that the coefficients are calibrated using the 2002 data, the correction model is effective for 2003 data. Because the intensity of shortwave forcing is influenced by the ground surface albedo (Section 3.5.2), the coefficients determined in this study may not be optimum for surface types other than grass.

TABLE 3.4. Statistics of the HOBO error before and after correction for the radiative error with Eq. 3.12 for 2002.

		Mean ($°C$)	Root mean square error ($°C$)
Day	original	0.39	0.39
	corrected	0.008	0.11
Night	original	-0.002	0.054
	corrected	0.0006	0.047

TABLE 3.5. Statistics of the HOBO error before and after correction for the radiative error with Eq. 3.12 for summer 2003.

		Mean ($°C$)	Root mean square error ($°C$)
Day	original	0.29	0.29
	corrected	-0.08	0.13
Night	original	-0.03	0.05
	corrected	-0.02	0.04

3.7. Summary

We propose that measurements of air temperature be made at a standard measurement height above the zero-plane displacement height. This standardization is necessary for eliminating the ambiguity of definitions of sensor-deployment heights particularly above vegetation of varying height. Otherwise, the estimation of the horizontal variations of air temperature is contaminated with the relative vertical variations of the mean temperature. In addition, the sensible heat flux estimates with the bulk-transfer method are subject to errors. The air temperature measurement error due to incorrectly estimated displacement heights is small in daytime unstable conditions, but increases with increasing stability at night. The error due to incorrectly estimated displacement heights limits the advantage of expensive aspirated sensor-shield systems. An improved methodology to estimate the displacement height is required particularly over non-uniform vegetation.

Within observational networks of air temperature, temperature sensors are often deployed in naturally ventilated shields instead of mechanically aspirated radiation shields due to economical consideration and unavailability of power. This study evaluates the radiative error of air temperature measurements by the HOBO thermistor in the Davis Instruments multi-plate radiation shield, also known as the Onset Computer radiation shield. This sensor-shield system is one of the practical and economical naturally ventilated sensor-shield systems.

Our measurements indicate that shortwave radiation reaching inside the multi-plate shield increases with increasing albedo of the surface. A significant portion of shortwave radiation inside the shield originates from shortwave radiation reflected from the ground surface. Thus, radiatively-induced temperature errors probably increase with increasing surface albedo. The magnitude of the deviation

of the shield surface temperature from the air temperature usually becomes larger during the daytime with shortwave forcing than during the nighttime. With this effect and shortwave radiation reaching inside the shield during the daytime, the radiative error of the air temperature measurement by the sensor-shield system becomes more significant during the daytime than during the nighttime. This diurnal trend is the opposite of that of the error due to inadequately evaluated zero-plane displacement heights. The daytime radiative error becomes large especially in conditions of weak wind and significant shortwave radiation. The radiative error decreases rapidly with increasing wind speed, which ventilates the sensor-shield system.

An empirical correction is proposed based on a nondimensional number that is proportional to the daytime shortwave or nocturnal net radiation and inversely proportional to the wind speed, both measured outside the multi-plate shield. Application of the model substantially reduces both the mean and root mean square of the radiative errors of the sensor-shield system particularly for daytime unstable conditions. Radiative errors for the nighttime stable conditions are much smaller than those for daytime and likely smaller than the errors due to height selection over variable vegetation. The robustness of the radiative error correction model is confirmed from independent data.

3.8. Acknowledgements

The authors wish to thank John Wong for his assistance with the field experiment and Scott Richardson and two anonymous reviewers for their helpful comments on the original manuscript. The authors are grateful to Michael Unsworth for both his assistance in the field and comments on the manuscript. The authors also wish to acknowledge Daryl Ehrensing of the Hyslop Experimental Station for allowing

us to conduct field observations in multiple seasons. This work is supported by the NASA Headquarters under the Earth System Science Fellowship, NASA Terrestrial and Ecology Program Grant NAGS5-11231 and Grant ATM-0107617 from the Physical Meteorology Program of the National Science Foundation.

3.9. References

Anderson, S.P., and M.F. Baumgartner, 1998: Radiative Heating Errors in Naturally Ventilated Air Temperature Measurements Made from Buoys. *J. Atmos. Oceanic Technol.* **15**, 157-173.

Arck, M., and D. Scherer, 2001: A physically based method for correcting temperature data measured by naturally ventilated sensors over snow. *J. Glaciol.* **47**, 665 - 670.

Brutsaert, W., 1982: *Evaporation into the Atmosphere.* Kluwer Academic Publishers, 299pp.

Campbell, G.C., 1969: Measurement of air temperature fluctuations with thermocouples. *ECOM-5273*, Atmospheric Sciences Laboratory, White Sands Missile Range, New Mexico, 10 pp.

Chelton, D.B., 1983: Effects of sampling errors in statistical estimation. *Deep-Sea Res.*, **30**, 1083-1103.

De Bruin, H.A. R., and C.J. Moore, 1985: Zero-plane displacement and roughness length for tall vegetation, derived from a simple mass conservation hypothesis *Boundary-Layer Meteorol.***31**, 39-49.

Erell, E., V. Leal, E. Maldonado, 2004: Measurement of air temperature in the presence of a large radiant flux: an assessment of passively ventilated thermometer screens. *Boundary-Layer Meteorol.*, **114**, 205-231.

Fuchs, M., and C.B. Tanner, 1965: Radiation shields for air temperature thermometers. *J. Appl. Meteor.* **4**, 544-547.

Gill, G.C., 1979: Development of a small rugged radiation shield for air temperature measurements on drifting buoys. NOAA Rep. Contract 01-7-038-827, National Data Buoy Center, Stennis Space Center, MS, 23 pp.

Ha, K.-J., and L. Mahrt, 2003: Radiative and turbulent fluxes in the nocturnal boundary layer. *Tellus* **55A**, 317-327.

Howell, J.R., 1982: *A catalog of radiation configuration factors.* McGraw-Hill Book Company, 243pp.

Hubbard, K.G., X. Lin, and E.A. Walter-Shea, 2001: The effectiveness of the ASOS, MMTS, Gill and CRS air temperature radiation shields. *J. Atmos. Oceanic Technol.* **18**, 851-864.

Incropera, F.P., and D.P. De Witt, 1990: *Fundamentals of Heat and Mass Transfer.* (third edition) John Wiley & Sons, 919pp.

Jones, H.G., 1992: *Plants and microclimate.*, second edition, Cambridge University Press, 299pp.

Kaimal, J.C., and J.J. Finnigan, 1994: *Atmospheric Boundary Layer Flows.* Oxford University Press. 289pp.

Lin, X., K.G. Hubbard, and G.E. Meyer, 2001 a: Airflow characteristics of commonly used temperature radiation shields. *J. Atmos. Oceanic Technol.* **18**, 329-339.

Lin, X., G. Hubbard, and E.A. Walter-Shea, 2001 b: Radiation loading model for evaluating air temperature errors with a non-aspirated radiation shield. *Transactions of the ASAE.* **44**, 1229-1306.

Mahrt, L., and D., Vickers, 2005: Moisture flux over snow with and without protruding vegetation. *Quart. J. Roy. Meteorol. Soc.* in press.

Monteith, J.L., and M. Unsworth, 1990: *Principles of Environmental Physics.* (second edition) Edward Arnold. 291pp.

Parlange, M.B., W. Brutsaert, 1989: Regional roughness of the Landes Forest and surface and shear stress under neutral conditions, *Boundary-Layer Meteorol.*, **48**, 69-80.

Raupach, M.R., 1994: Simplified expressions for vegetation roughness length and zero-plane displacement as functions of canopy height and area index. *Boundary-Layer Meteorol.*, **71**, 211-216.

Richardson, S.J., F.V. Brock, S.R. Semmer and C. Jirak, 1999: Minimizing errors associated with multiplate radiation shields. *J. Atmos. Oceanic Technol.* **16**, 1862-1872.

Stull, R.B., 1988: *An introduction to boundary layer meteorology.* Kluwer Academic Publishers, 666pp.

Tanner, B.D., E. Swiatek, C. Maughan, 1996: Field comparisons of naturally ventilated and aspirated radiation shields for weather station air temperature measurements. Preprints, *22nd Conf. On Agricultural and Forest Meteorology.* Atlanta, GA, Amer. Meteor. Soc., 227 230.

Tanner, C.B., 1979: Temperature: Critique I. *Controlled Environment Guidelines for Plant Research.*, T.W. Tibbitts and T.T. Kozlowski, Eds., Academic Press, 117 130.

Whiteman, C.D., J.M. Hubbe, and W.J. Shaw, 2000: Evaluation of an inexpensive temperature data logger for meteorological applications. *J. Atmos. Oceanic Technol.* **17**, 77-81.

4. VERTICALLY-INTEGRATED SENSIBLE HEAT BUDGETS WITHIN STABLE NOCTURNAL BOUNDARY LAYERS

Reina Nakamura and Larry Mahrt

To be submitted to in *Quarterly Journal of the Royal Meteorological Society*,

The Royal Meteorological Society, Reading, Great Britain.

4.1. Abstract

The stable nocturnal boundary layer is commonly viewed or modelled as a balance between heat storage and vertical heat flux divergence. Sometimes the radiative flux divergence is also included. This perspective has also dictated the design of field experiments for investigating stable nocturnal boundary layers.

Tower-based micrometeorological data from three field campaigns are analyzed to evaluate the vertically-integrated sensible heat budget for nocturnal stable conditions. Our analysis indicates frequent occurrence of large imbalance between the storage and vertical heat flux divergence terms. The values of the radiative flux divergence are generally too small and sometimes of the wrong sign to explain the residual. An extensive error analysis is performed, which suggests that instrumental and sampling errors also cannot explain the large imbalance. The imbalances suggest importance of advection of temperature or possibly the divergence of mesoscale fluxes. It is shown that existing field data do not allow adequate evaluation of these terms.

4.2. Introduction

As the Earth's surface is radiatively cooled and daytime convective turbulence eddies collapse, the atmospheric boundary layer becomes stratified. Physical processes contributing to evolutions of stable boundary layers have been frequently examined with a one-dimensional approach. Most studies (e.g., Wyngaard, 1975; Brost and Wyngaard, 1978) have considered that shear-generated turbulence causes downward heat flux to the cooled surface, leading to development of an inversion layer. A few studies (e.g. Brunt,1934; Anfossi et al., 1976) have explained the evolution of surface inversions based on the vertical radiative flux divergence. In other

studies, both vertical radiative and heat flux divergence are taken into account for evolution of stable boundary layers (Andre and Mahrt, 1982; Nieuwstadt, 1980). The one-dimensional approach assumes advection is negligible and has dictated the design of many field experiments for investigating stable boundary layers. We investigate the validity of the one-dimensional approach from three field programs over weak surface heterogeneity.

4.3. Sensible Heat Flux Budget Equation

It is not useful or even possible to explicitly consider the value of turbulence quantities at every point in space and time. Consequently, turbulence is traditionally described in terms of ensemble averages for random processes and associated Reynolds averaging. Although application of such an approach to the heat budget requires reconsideration with ensemble averaging, a variable of state, ϕ, can be decomposed as

$$\phi = \phi' + [\phi] \tag{4.1}$$

where ϕ' is the turbulent fluctuations and $[\phi]$ is the ensemble-average of ϕ over all of the realizations, where ϕ may be a function of spatial position and time from the beginning of the realization. Theories of turbulence are based on the concept of an ensemble mean and turbulence deviations from that mean, which readily satisfy Reynolds averaging. The sensible heat budget can be written as

$$\frac{\partial[\theta]}{\partial t} = -[V_H]\cdot\nabla[\theta] - [W]\frac{\partial[\theta]}{\partial z} - \frac{\partial[u'\theta']}{\partial x} - \frac{\partial[v'\theta']}{\partial y} - \frac{\partial[w'\theta']}{\partial z} - \frac{1}{\rho C_p}\frac{\partial[F_n]}{\partial z} \tag{4.2}$$

No phase change in water molecules is considered in the equation above. The ensemble averaging-operator [ ] is carried out for each point in space and time relative to the beginning of the realization. From the left, individual terms represent the local

or Eulerian time derivative, hereafter referred to as storage, horizontal advection, vertical advection, heat flux divergence in along-wind direction, heat flux divergence in cross-wind direction, vertical heat flux divergence, and diabatic heating or cooling.

Ensemble averages are not strictly possible in geophysical flows. Therefore, one normally assumes that the flow is sufficiently stationary that the ensemble average can be replaced with a time average. With analysis of aircraft data, one assumes that the flow is sufficiently homogenous that the ensemble average can be replaced with a spatial average. Spatial and time derivatives of the mean flow are still allowed since they are assumed to occur on much larger scales than the turbulence; that is the flow is characterized by a spectral gap between turbulent motions and larger-scale flow.

However, even this approximation of separation of time scales is rarely realized in geophysical flows. Mesoscale motions on scales just larger than turbulence scales are normally present (Mahrt et al., 2001; Vickers and Mahrt, 2003). Nonetheless, useful turbulence statistics can be constructed provided that one carefully selects averaging times to define the perturbations and realizes that nonstationarity degrades the meanings of the useful turbulence statistics depending on the degree of nonstationarity.

One must choose a sufficiently small averaging time, τ, to define turbulence motions, ϕ' and exclude mesoscale motions, ϕ^*. Turbulence statistics are often averaged over a time, τ_F, to reduce the random flux error. Then, the flow is decomposed as

$$\phi = \phi' + \phi^* + [\phi] \tag{4.3}$$

where [ ] is now the averaging operator over time scale τ_F which attempts to approximate an ensemble average. Turbulence and mesoscale fluctuations, ϕ' can also be written as

$$\phi' = \phi - \overline{\phi} \tag{4.4}$$

$$\phi^* = \overline{\phi} - [\phi] \tag{4.5}$$

where $\overline{(\ )}$ is an averaging operator over the time scale τ. The approximated ensemble average will be a poor approximation in strongly nonstationary conditions.

In order to satisfy Reynolds averaging, the time averages must be unweighted simple (block) averages. For example, defining the short time averaging operator $\overline{(\ )}$ with a filter or moving average violates traditional Reynolds averaging and additional terms, such as $\overline{w'\phi^*}$ (Leonard terms) result. However, in approximately stationary conditions, we find these terms to be small. We proceed with nonoverlapping, unweighted averaging windows. We are not claiming that this approach is superior to weighted averaging (filtering). Errors due to nonstationarity are always present with either approach.

With unweighted averaging, the vertical flux of variable ϕ averaged over a record consists of three components:

$$[w\phi] = [\overline{w'\phi'}] + [w^*\phi^*] + [[W][\phi]] \tag{4.6}$$

where the first term on the right hand side is the estimate of the ensemble-averaged turbulence flux, the second term is the ensemble-averaged mesoscale flux, and the third term is the transport due to the mesoscale and synoptic scale motions on scales larger than the record length (τ_F). The third term is normally converted to advection form by applying the incompressible mass continuity equation to all three

momentum equations. Equations for horizontal flux of variable ϕ can be written analogously to Eq. 4.6.

The heat budget equation becomes:

$$\frac{\partial[\theta]}{\partial t} = -[V_H]\cdot\nabla[\theta] - [W]\frac{\partial[\theta]}{\partial z} - \frac{\partial[\overline{u'\theta'}]}{\partial x} - \frac{\partial[\overline{v'\theta'}]}{\partial y} - \frac{\partial[\overline{w'\theta'}]}{\partial z} - \frac{\partial[\overline{u^*\theta^*}]}{\partial x} - \frac{\partial[\overline{v^*\theta^*}]}{\partial y} - \frac{\partial[\overline{w^*\theta^*}]}{\partial z} - \frac{1}{\rho C_p}\frac{\partial[F_n]}{\partial z} \tag{4.7}$$

With a typical record length, $\tau_F \sim 30$ min to 1hr, the record-averaged mesoscale flux is contaminated by large random sampling errors, thus is inadequate for even rough estimates of ensemble-averaged mesoscale flux (Vickers and Mahrt, 2005). Therefore, terms with mesoscale flux in Eq. 4.7 cannot be evaluated for the heat budget over a typical τ_F although their contribution can be potentially significant.

The storage term in Eq. (4.7) is not well defined in that $\frac{\partial[\theta]}{\partial t} = 0$ for the entire record except for the beginning and the end of the record when $\frac{\partial[\theta]}{\partial t} = \infty$. This is an artifact of replacing the ensemble average by the block time-average. Two approaches can be taken to ameliorate this problem:

1. Use a finite differencing method based on the hourly mean temperature records. Numerical models apply this approach to the values at different time steps as in centered finite differencing. The centered differencing leads to an artificial gap in time scale in that motions on time scales between τ_F and $2\tau_F$ are not considered.

2. The time derivative can be estimated by smoothing the original time series of θ before estimating values at the beginning and end of the record. This approach can be viewed as applying filtering only to the storage term.

As an aside, the time derivative can be computed exactly by discarding the concept of an ensemble average, that is

$$\frac{\partial[\theta]}{\partial t} = \frac{\theta(t_2) - \theta(t_1)}{t_2 - t_1} \tag{4.8}$$

where $\theta(t_2)$ and $\theta(t_1)$ are instantaneous measurements. Although mathematically exact, this approach is a poor choice in terms of approximating the ensemble value. The instantaneous values of $\theta(t_2)$ and $\theta(t_1)$ can be strongly influenced by individual eddies. In terms of ensemble averages, this estimate may be dominated by random errors. This method may be adequate for studies where individual records are averaged over many individual records in order to evaluate long term budgets, as in studies of carbon dioxide. In the non-ensemble approach, fluctuations for computing fluxes must be the average over the record length, τ_F so that the turbulence and mesoscale motions are included in the budget.

4.4. Data

4.4.1. CASES-99

The Cooperative Atmosphere-Surface Exchange Study-99 (CASES-99) took place over grassland in south central Kansas, U.S.A. in October 1999 (Poulos et al., 2002). On the 60-m main tower, wind and flux measurements were made at 6 levels (10 m, 20 m, 30 m, 40 m, 50 m, 55 m) at 20 Hz by sonic anemometers (K-probe, ATI and Campbell Csat3). On the same tower, thermocouples measured air temperature at 5 Hz at 32 levels with 1.8-m intervals between 2.3 m and 58.1 m height. To avoid the influence of experiment-related equipment at the bottom of the main tower, near-surface wind and flux measurements were made at a 10-m tower located 10 m away from the main tower. The 10-m tower was equipped with additional sonic anemometers at 1.5 m and 5 m and thermocouples at 0.23 m and 0.63 m. The sonic anemometer at 1.5 m was moved to 0.5 m toward the end of the experiment. The measurements from the 60-m tower and 10-m tower are analyzed together as the main tower data in this study.

In addition to the measurements made at the main tower, turbulence flux measurements were made at 5-m levels by sonic anemometers on two sets of 3 satellite towers surrounding the main tower, situated on circles of 100-m and 300-m radius, respectively. We discard all sonic anemometer data collected between the wind directions of 202° and 337° to avoid flow through the towers.

4.4.2. FLOSSII

Fluxes over Snow Surfaces II (FLOSSII) was conducted over grassland in northern Colorado, U.S.A. from November 2002 to April 2003 (Mahrt and Vickers, 2005). Sonic anemometers (Campbell Csat3) were operated at 50 Hz at 1, 2, 5, 10, 15, 20 and 30 m on a 34-m tower. Aspirated thermistors monitored air temperature at 1 Hz at the same heights as the sonic anemometers. The grass was covered partially or fully by snow for a part of the experiment. We do not analyze flux measurements made in the wind directions between 322.5° and 97.5° to eliminate flow through the tower.

4.4.3. Microfronts

The Microfronts field study was carried out in rangeland in south central Kansas, U.S.A. in March 1995. Micrometeorological measurements were made in two tower groups, and the present study analyzes those from the south tower cluster. The south tower cluster consisted of three 10-m towers separated by 10m in a line from northeast to southwest direction. The first tower was instrumented with sonic anemometers (K-probe, ATI) at 3 m and 10 m height. The sampling rate of the sonic anemometers was 10 Hz. The second tower was equipped with propeller-vane anemometers operating at 5 Hz for wind direction and speed at 3 m, 5 m

and 10 m. On the third tower, air temperature was sampled at 1 Hz at 5 levels (2, 3, 5, 7, and 10 m). Sonic anemometer data obtained between the wind attack angles of 337.5° and 112.5° are eliminated because of flow through the tower. More details of this experiment can be found in Howell and Sun (1999). All the data are quality-controlled according to Vickers and Mahrt (1997).

4.5. Evaluating the Vertically-Integrated Sensible Heat Budget

Table 4.1 summarizes the heights and depths of layers for which the heat budget is analyzed. For CASES-99 and FLOSSII, we have chosen not to include the layer below 5 m because of possible loss of flux due to path-length averaging (see the Appendix) and because of possibly large radiative flux divergence at the surface that is difficult to estimate. For the CASES-99 data set, two sets of vertically-integrated heat budgets (Table 4.1) are investigated to examine variations of the heat budget with height. The CASES-99 upper layer is considered to be in a different regime from the other analyzed layers which were situated closer to the surface. In CASES-99, vertical heat flux frequently vanished between 20 to 30 m above the ground, and nocturnal jets generated turbulence at the upper levels on the main tower (Mahrt and Vickers, 2002), where our CASES-99 upper layer was located.

To identify the period of stable boundary layers, we composite the vertical heat flux for the top and bottom layer as a function of the time of the day. Hours with negative heat flux in the composite except for the first and last hours are defined as the period of stable boundary layers to avoid large nonstationarity. The hours considered for the heat budget analysis are 1800 - 0700, 1700 - 0800, and 1900 - 0700 (all in LST) for CASES-99, FLOSSII and Microfronts, respectively. Here, we

TABLE 4.1. Summary of air-layers considered for heat budget analysis. "Averaging time" corresponds to the time interval over which the temperature data are pre-averaged for analysis.

Field Experiment	Layer Bottom (m)	Layer Top (m)	Temperature Measurement Heights (m)	Averaging Time (s)
CASES-99 (lower)	5	20	5.9, 7.2, 9.5, 11.3, 13.1, 14.9, 16.7, 18.5 (thermocouples)	100
CASES-99 (upper)	30	55	31.1, 33.9, 34.7, 36.5, 38.3, 40.1, 41.9, 43.7, 45.5, 47.3, 49.1, 50.9, 52.7, 54.5 (thermocouples)	100
FLOSSII	5	30	5, 10, 15, 20, 30 (thermistors)	300
Microfronts	3	10	3, 5, 7, 10 (thermistors)	300

will set τ_F to 1 hour and set τ to a variable determined from each individual record using the method of Vickers and Mahrt (2005).

Vertical-integration of Eq. (4.7) yields

$$\begin{aligned}\int_{z_1}^{z_2}\frac{\partial[\theta]}{\partial t}dz = &-\int_{z_1}^{z_2}[V_H]\cdot\nabla[\theta]dz-\int_{z_1}^{z_2}[W]\frac{\partial[\theta]}{\partial z}dz\\ &-\int_{z_1}^{z_2}(\frac{\partial[\overline{u'\theta'}]}{\partial x}+\frac{\partial[\overline{v'\theta'}]}{\partial y})dz-\int_{z_1}^{z_2}\frac{\partial[\overline{w'\theta'}]}{\partial z}dz\\ &-\int_{z_1}^{z_2}(\frac{\partial[\overline{u^*\theta^*}]}{\partial x}+\frac{\partial[\overline{v^*\theta^*}]}{\partial y})dz-\int_{z_1}^{z_2}\frac{\partial[\overline{w^*\theta^*}]}{\partial z}dz\\ &-\int_{z_1}^{z_2}\frac{1}{\rho C_p}\frac{\partial[F_n]}{\partial z}dz\end{aligned} \tag{4.9}$$

where z_1 and z_2 indicate the lower and upper levels of the air layer and F_n is considered to be radiative flux in this case. For all studies, no liquid water was present in any of the layers, thus phase change of water did not contribute to the heat budget. The heat budget analysis is performed for individual qualified nocturnal hours.

4.5.1. Storage, Vertical Heat Flux Divergence and Residual

Because we are interested in the heat budget of individual hours, we adopt the second approach introduced in Section 4.3 for computing the ensemble average of the storage term. We use two methods for smoothing the original record of potential temperature. In the first method, a time-series of vertically-integrated potential temperature is linearly regressed on time for every hour. The values at the beginning and end of the hour are calculated from the estimated regression line. In the second method, the vertically-integrated potential temperature at the beginning and end of the hour is computed by using 10-min averaging windows centered at the boundaries. For generating a time series of vertically-integrated

potential temperature, the measurement of potential temperature at each height is assumed representative of the layer in which it is embedded. The layer boundaries are defined by the mid-level between two temperature measurements. The details of the analyzed temperature data are shown in Table 4.1. For evaluation of the heat budget, the storage term is set to the mean of the storage estimated by the two methods.

The vertical heat flux divergence term is evaluated from the hourly average of the turbulence heat flux. The residual, R, for the evaluated heat budget is defined as

$$R \equiv -(\int_{z_1}^{z_2} \frac{\partial[\theta]}{\partial t} dz + \int_{z_1}^{z_2} \frac{\partial[\overline{w'\theta'}]}{\partial z} dz) = -\int_{z_1}^{z_2} \frac{\partial[\theta]}{\partial t} dz - [(\overline{\theta' w'})_{z_2} - (\overline{\theta' w'})_{z_1}] \quad (4.10)$$

4.5.2. Sensible Heat Budget: Field Experiment-Averages

The characteristics of the storage, vertical heat flux divergence and residual terms over the entire experiment are examined in terms of the constancy of a given term, X defined as

$$constancy \equiv \frac{\frac{\sum_{i=1}^{N} X_i}{N}}{\frac{\sum_{i=1}^{N} |X_i|}{N}} \quad (4.11)$$

where N indicates the number of hourly records, and where X is either $\int_{z_1}^{z_2} \frac{\partial[\theta]}{\partial t} dz$, $\int_{z_1}^{z_2} \frac{\partial[\overline{w'\theta'}]}{\partial z} dz$ or R for the record i. When X occurs randomly with either sign, constancy is 0. When the term X is positive (negative) for all the records, constancy is 1 (-1).

Table 4.2 summarizes the numerator and denominator of Eq. 4.11 and the constancy computed for each investigated layer. The reported values in Table 4.2 are visualized in Figs. 4.1 - 4.3. The experiment-averaged storage term

TABLE 4.2. Statistics of the mean layer storage, mean layer vertical heat flux divergence and mean layer residual terms (Kh^{-1}) over the entire field experiments. "mean" and "abs-mean" correspond to the experiment-averages of each term and of the absolute value of each term, respectively. The first number in parentheses of the "mean" column indicates the standard error of the experiment-average of the term. The second number indicates the experiment-average of the error bars (Err_{stor}, Err_{hfd} or Err_{res} divided by the layer depth) over all the records (Section 4.6.1 and Appendix.)

Field Experiment	$\frac{\int_{z_1}^{z_2} \frac{\partial[\theta]}{\partial t} dz}{z_2 - z_1}$		
	mean	abs mean	constancy
CASES-99 (lower)	-0.700 ($\pm$ 0.077, $\pm 6 \times 10^{-4}$)	0.88	-0.80
CASES-99 (upper)	-0.630 ($\pm$ 0.059, $\pm 5 \times 10^{-4}$)	0.80	-0.79
FLOSSII	-0.230 ($\pm$ 0.029, $\pm 1 \times 10^{-4}$)	0.81	-0.29
Microfronts	-0.443 ($\pm$ 0.078, $\pm 9 \times 10^{-4}$)	0.74	-0.60

Field Experiment	$\frac{\int_{z_1}^{z_2} \frac{\partial[\overline{w'\theta'}]}{\partial z} dz}{z_2 - z_1}$		
	mean	abs mean	constancy
CASES-99 (lower)	0.563 ($\pm$ 0.15, $\pm 8 \times 10^{-3}$)	1.39	0.40
CASES-99 (upper)	-0.655 ($\pm$ 0.11, $\pm 5 \times 10^{-3}$)	0.94	-0.70
FLOSSII	1.03 ($\pm$ 0.046, $\pm 5 \times 10^{-4}$)	1.44	0.72
Microfronts	1.62 ($\pm$ 0.54, $\pm 9 \times 10^{-2}$)	4.26	0.38

Field Experiment	$\frac{R}{z_2 - z_1}$		
	mean	abs mean	constancy
CASES-99 (lower)	0.136 ($\pm$ 0.16, $\pm 8 \times 10^{-3}$)	1.45	0.09
CASES-99 (upper)	1.28 ($\pm$ 0.12, $\pm 5 \times 10^{-3}$)	1.52	0.85
FLOSSII	-0.801 ($\pm$ 0.05, $\pm 6 \times 10^{-4}$)	1.65	-0.49
Microfronts	-1.17 ($\pm$ 0.54, $\pm 9 \times 10^{-2}$)	4.15	-0.28

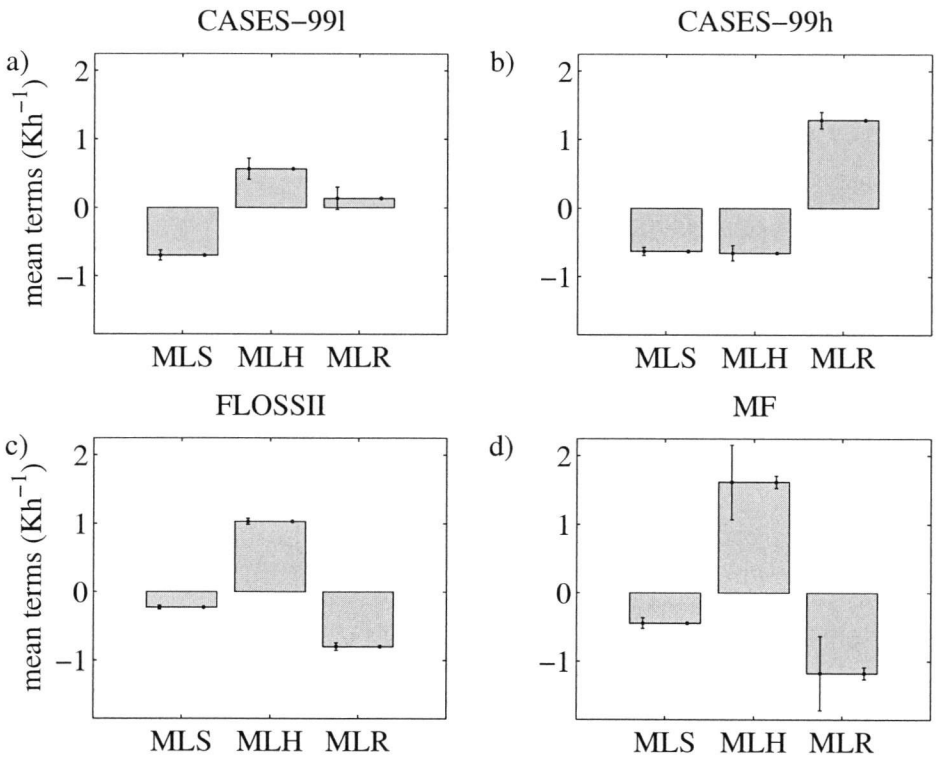

FIGURE 4.1. The mean layer storage, $\frac{\int_{z_1}^{z_2} \frac{\partial [\theta]}{\partial t} dz}{z_2 - z_1}$ (MLS), mean layer vertical heat flux divergence, $\frac{[\overline{\theta' w'}]_{z_2} - [\overline{\theta' w'}]_{z_1}}{z_2 - z_1}$ (MLH) and mean layer residual, $\frac{R}{z_2 - z_1}$ (MLR) averaged over the entire experiment: a) CASES-99 lower layer b) CASES-99 upper layer c) FLOSSII d) Microfronts. The error bar on the left is the standard error of the experiment-averaged value. The error bar on the right is the experiment-averaged mean layer value of Err_{stor}, Err_{hfd} or Err_{res} (Section 4.6.1 and Appendix) divided by the layer depth over all the records. Numerical values of the variables plotted above are found in Table 4.2.

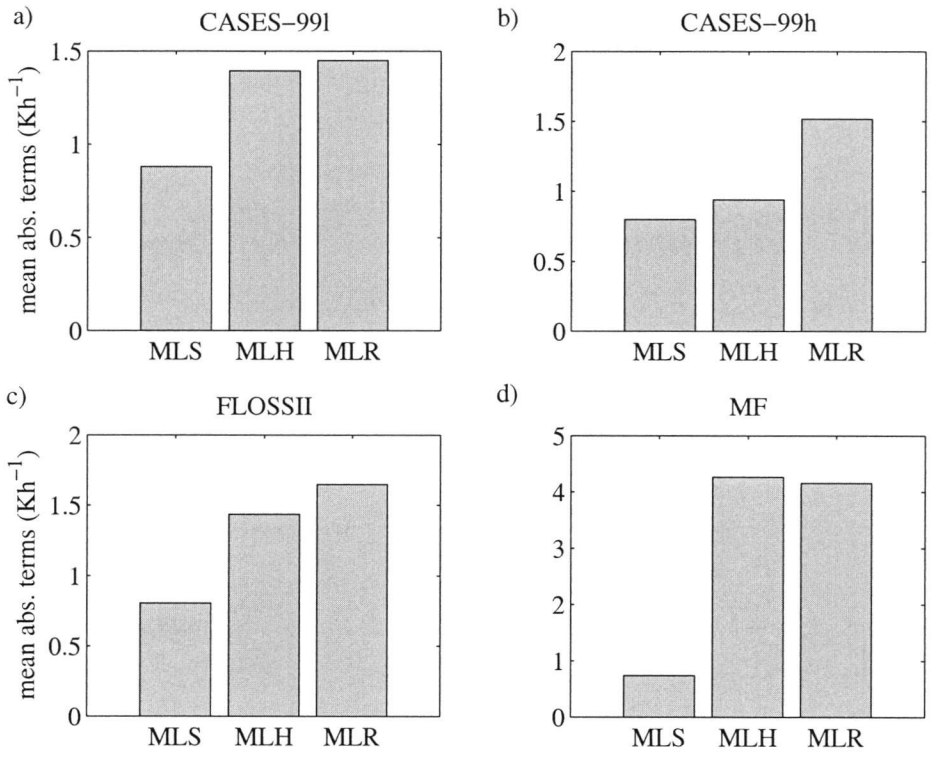

FIGURE 4.2. Same as Fig 4.1 except for the experiment-average of the absolute values of the mean layer storage (MLS), mean layer vertical heat flux divergence (MLH) and mean layer residual (MLR).

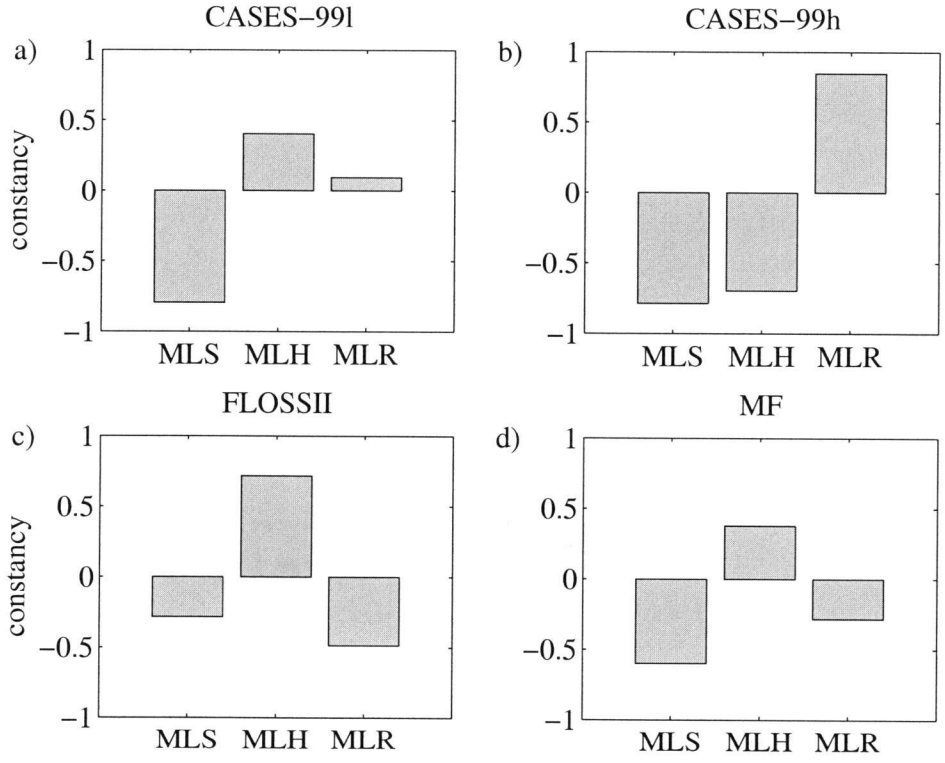

FIGURE 4.3. Constancy of the mean layer storage (MLS), mean layer vertical heat flux divergence (MLH) and mean layer residual (MLR).

is negative for all the data sets although it is small for FLOSSII where frequent warming of air temperature was observed on many of the nights. That is, the sign of the storage term is less systematic between records (Fig. 4.4, Section 4.6). The experiment-averaged vertical heat flux divergence term corresponds to convergence for the CASES-99 upper layer, but divergence for the lower layer as well as the other two sites. The constancy of the vertical heat flux divergence term for the CASES-99 upper layer is large and negative, corresponding to persistent heat flux convergence while the storage term is on average negative (cooling). That is, the heat flux convergence predicts warming, so that the observed cooling must be due to the other unevaluated terms in the heat budget or possibly systematic errors of the storage or heat flux divergence term. For the CASES-99 lower layer, FLOSSII and Microfronts, the observed cooling is the same sign as predicted by the flux divergence; that is the heat flux divergence contributes to the cooling of the air in agreement with the concept of a nocturnal boundary layer.

However, the residual of the individual hourly records (Fig. 4.2) is large for all field programs. The experiment-averaged residual, R, is dominated by "random" variation for the CASES-99 lower layer and is small when averaged over the field program (Fig. 4.3). Such random variation could be due to, for example, transient mesoscale motions. On the other hand, the experiment-averaged residuals for the CASES-99 upper layer, FLOSSII and Microfronts are more systematic, implying systematic errors or systematic contributions from unevaluated terms such as advection.

4.6. Sources of the Residual

In this section, the heat budget is examined for individual hours to identify sources of the observed large residual. The estimated mean layer storage, vertical heat flux divergence, and inferred residual from individual records are illustrated in Fig. 4.4.

4.6.1. Statistical Significance of the Residual

We first investigate the statistical significance of the residual in the hourly heat budgets by evaluating uncertainties associated with the estimated storage and vertical heat flux divergence. Uncertainty of the estimated residual, Err_R, due to the uncertainties of the terms of the right hand side of Eq. 4.10, is estimated as

$$Err_R = Err_{stor} + Err_{hfd} \tag{4.12}$$

where Err_{stor} and Err_{hfd} correspond to error estimates of the storage and vertical heat flux divergence terms (Appendix), respectively. This error estimate for the residual is an overestimate because it assumes the errors on the right hand side have the same sign.

For examining the significance of the residual, two criteria are introduced. First, if the absolute magnitude of the residual is larger than the error, Err_R, we consider the residual to be significant. Second, if $|R_{max}| > |S_{min}|$ or $|R_{max}| > |H_{min}|$, the residual is considered significant, where $|R_{max}|$, $|S_{min}|$ and $|H_{min}|$ are defined as

$$|R_{max}| = |R| + Err_{res} \tag{4.13}$$

$$|S_{min}| = |\int_{z_1}^{z_2} \frac{\partial[\theta]}{\partial t} dz| - Err_{stor} \tag{4.14}$$

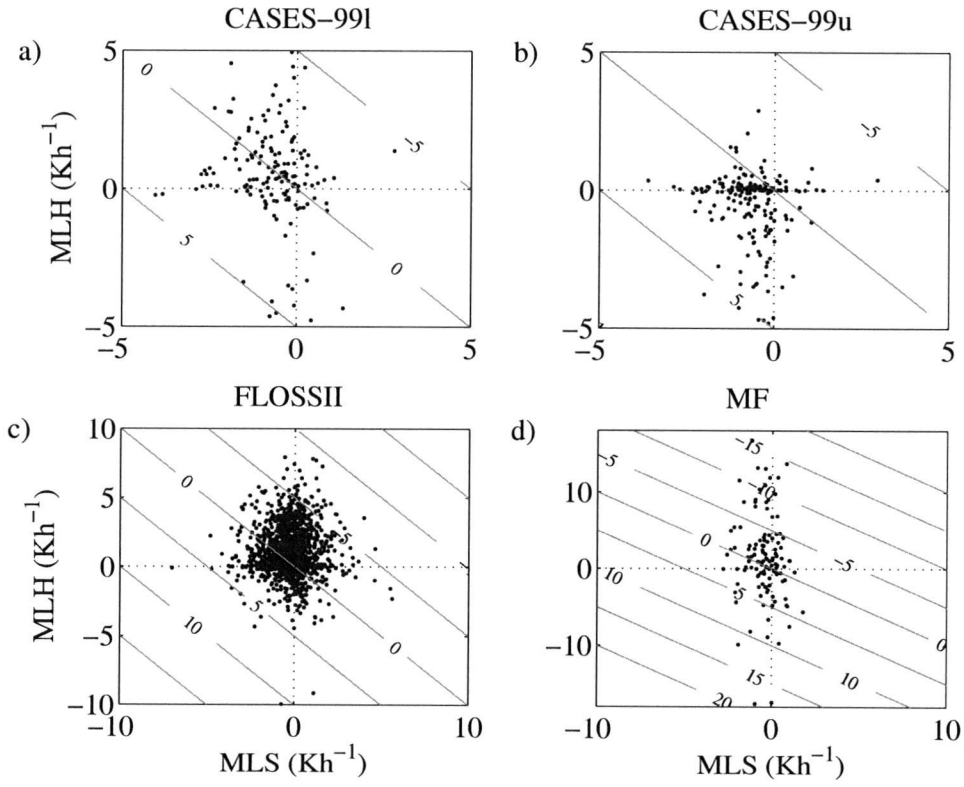

FIGURE 4.4. Joint distribution of the mean layer vertical heat flux divergence term, $\frac{[\overline{\theta' w'}]_{z_2} - [\overline{\theta' w'}]_{z_1}}{z_2 - z_1}$ (MLH) and the mean layer storage term, $\frac{\int_{z_1}^{z_2} \frac{\partial [\theta]}{\partial t} dz}{z_2 - z_1}$ (MLS) for all records. a) CASES-99 lower layer b) CASES-99 upper layer c) FLOSSII d) Microfronts. Contour-lines (interval = $5Kh^{-1}$) indicate the mean layer residual of the heat budget.

TABLE 4.3. Summary of the sensible-heat budget analysis. Second column: total hours for which the layer heat budget analysis is performed. Third column: percentage of total hours for which the residual passes both significance tests (see text). Fourth column: percentage of total hours for which the residual fails both significance test (see text).

Field Experiment	Total hours	Significant residual	Insignificant residual
CASES-99 (lower)	153	59 %	1.3 %
CASES-99 (upper)	188	86 %	0.5 %
FLOSSII	1513	71 %	2.1 %
Microfronts	124	52 %	0.8 %

$$|H_{min}| = |\int_{z_1}^{z_2} \frac{\partial[\overline{w'\theta'}]}{\partial z} dz| - Err_{hfx} \tag{4.15}$$

The percentage of the entire records in which the computed residual fulfills both of the significance criteria varies between 52-86 % of the entire records depending on data set (Table 4.3). The percentage of the entire records in which computed residual, R, fulfills neither of the criteria varies between 0.5-2.1 % (Table 4.3). In these records, the residual is considered insignificant in the heat budget, implying an approximate balance between the storage and vertical heat flux divergence term. The above result suggests that the residual corresponds to a significant portion of the heat budget for almost all of the records.

While we cannot completely rule out problems with instrumentation as a source of the residual, it is unlikely that the large residuals can be explained by sampling and instrumentation problems alone (Appendix). Therefore, the horizon-

tal heat flux divergence, radiative flux divergence, advection and mesoscale flux divergence terms must be estimated.

4.6.2. Horizontal Heat Flux Divergence

The order of magnitude of the horizontal heat flux divergence, $\int_{z_1}^{z_2}(\frac{\partial[\overline{u'\theta'}]}{\partial x} + \frac{\partial[\overline{v'\theta'}]}{\partial y})dz$ is estimated from the CASES-99 data, in which turbulence flux measurements are available at 5-m levels at 7 locations within the tower network (Section 4.4). The horizontal heat flux divergence is estimated at the main tower 5-m level using the linear vector point function method (LVPF) (Zamora et al., 1987). This analysis is first performed using three horizontal heat flux measurements at the 100-m radius and is repeated using those at the 300-m radius. The absolute magnitude of the heat flux divergence term averaged over all records is 0.31 and 0.10 Kh^{-1} for the 100-m and 300-m radius measurements, respectively. The sign of this term varies from one record to another, and the all-record average of the term is -0.03 Kh^{-1} and 0.02 Kh^{-1} for the 100-m and 300-m radius measurements, respectively. Although the above estimates are strictly valid for a single height and not a layer, they suggest that the horizontal heat flux divergence is generally too small to explain the residual.

4.6.3. Radiative Flux Divergence

No adequate radiation measurements are available for estimating the radiative flux divergence, $\int_{z_1}^{z_2}\frac{1}{\rho C_p}\frac{\partial[F_n]}{\partial z}dz$, across the air layers in Table 4.1. Based on radiation measurements, Sun et al. (2003) estimated radiative flux divergence for a deeper CASES-99 tower layer ($2-48m$) and found that the radiative flux divergence typically becomes largest in the early evening. The monthly mean of the radiative

flux divergence in the early evening for their air layer ($z = 2 - 48m$) was on the order of a few tenths of a degree per hour although they reported values as high as $\sim 1Kh^{-1}$ for the radiative flux divergence for one of the early evenings.

The modeling study of Ha and Mahrt (2003) also concluded that the radiative flux divergence becomes large in the early evening and can be the primary contributor to the initial formation of the surface inversion in CASES-99. In the early evening, the cooling rate was typically $\sim 0.5Kh^{-1}$ for the 60-m tower layer except for a few meters closest to the ground surface, where the cooling rate became 1 to 3 Kh^{-1} although the model may be inaccurate close to the ground. Later in the evening, the magnitude of the radiative flux divergence decreased to half of that in the early evening, which was generally substantially smaller than vertical heat flux divergence. Earlier modeling studies (e.g. Garratt and Brost, 1981; Estournel et al., 1986; Andre and Mahrt, 1987) have estimated similar radiative cooling rates.

Based on the radiative flux divergence term in the literature, we estimate the typical radiative flux divergence to be to a few tenths of a degree per hour for all the air layers investigated in the present study although this is probably an overestimation for FLOSSII where the moisture content is generally small. Inclusion of this "typical magnitude" of the radiative flux divergence shifts the clusters of data points in Fig. 4.4 diagonally toward the top right corner by a few tenths of Kh^{-1}. However, inspection of the figure reveals that the radiative flux divergence is generally too small to explain the residual, R, alone and even sometimes has the opposite sign from the residual.

4.6.4. Advection

Evaluation of the vertical advection term requires accurate estimates of the mean vertical wind speed. The vertical mean wind speed decreases toward the surface and is thought to be typically a few cms^{-1} or less in the tower layers. Even a small sensor-tilt relative to the ground can seriously contaminate the true vertical mean wind speed. For example, a tilt angle of 1° induces a spurious vertical mean wind velocity $[W]$ of 8 cms^{-1} if the horizontal mean wind speed is 5 ms^{-1}

The vertical wind velocity $[W]$ at the 10-m level on the CASES-99 main tower is estimated from both the sonic anemometer and from the continuity equation using estimates of the horizontal divergence of the wind vector. The tilt correction is made for all the sonic anemometers as in Mahrt et al. (2000). The divergence of horizontal wind vectors, $\nabla \cdot V_H$ is evaluated at the 5-m level with the LVPF method (Section 4.6.2). $[W]$ at the 10-m level is evaluated in terms of $\nabla \cdot V_H$ at 5 m by assuming that $\nabla \cdot V_H$ varies linearly with height from zero at ground surface. The values of $[W]$ estimated from the continuity equation and the sonic anemometer frequently disagree both in order of magnitude and sign (Fig 4.5a). $[W]$ calculated from the horizontal divergence from the 100-m and 300-m radii agree better with each other in magnitude, but even then, 1/3 of the two divergence estimates disagree in sign. While the estimate from the 300-m radius is less vulnerable to small differences between large numbers, the horizontal divergence based on the 100-m radius may be more relevant to the low-level vertical motions on the tower. Sources of the differences between $[W]$ estimates are concurrently under investigation, and confident estimates of $[W]$ are not yet possible.

As an exercise, we evaluate the order of magnitude of the mean layer $[W]$ by assuming that 1) the entire residual is balanced by the vertical advection term,

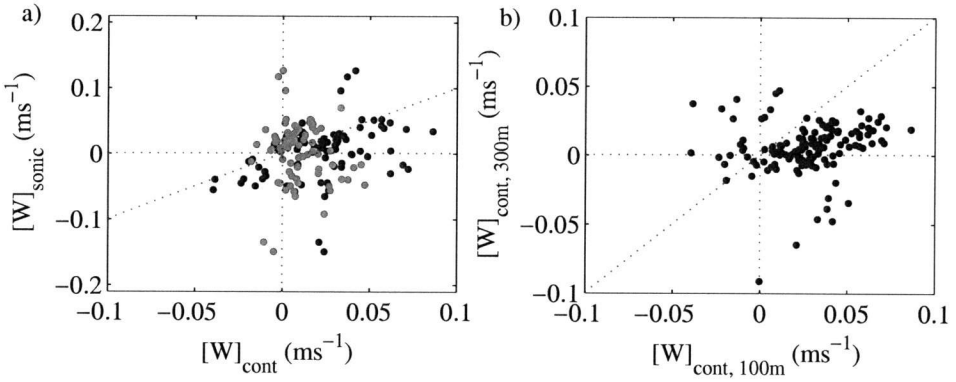

FIGURE 4.5. a) Comparison of $[W]$ estimated by a sonic anemometer and from the continuity equation for the main tower 10-m level in CASES-99. Horizontal divergence is estimated from wind vectors for the 100-m radius (black) and 300-m radius (gray) towers. b) Comparison of $[W]$ computed from the horizontal divergence estimated from wind vectors at 100-m radius and 300-m radius. The diagonal dotted lines correspond to 1:1 lines. Other dotted lines are zero-lines.

2) the finite difference of the potential temperature over the layer represents the vertical potential temperature gradient everywhere across the layer. For all the layers, most of the records yield an absolute value of the mean layer $[W]$ of less than a few cms^{-1} (Fig. 4.6). That is, even a small $[W]$ could theoretically explain the entire residual.

We are unable to estimate the horizontal advection term for the heat budget because none of the present data sets allow calculations of the horizontal temperature gradients. As an exercise similar to that for the vertical advection term, we calculate the horizontal temperature gradient required to balance the residual of the heat budget. For this order of magnitude estimate, we assume that the horizontal temperature gradient remains constant with height across a layer.

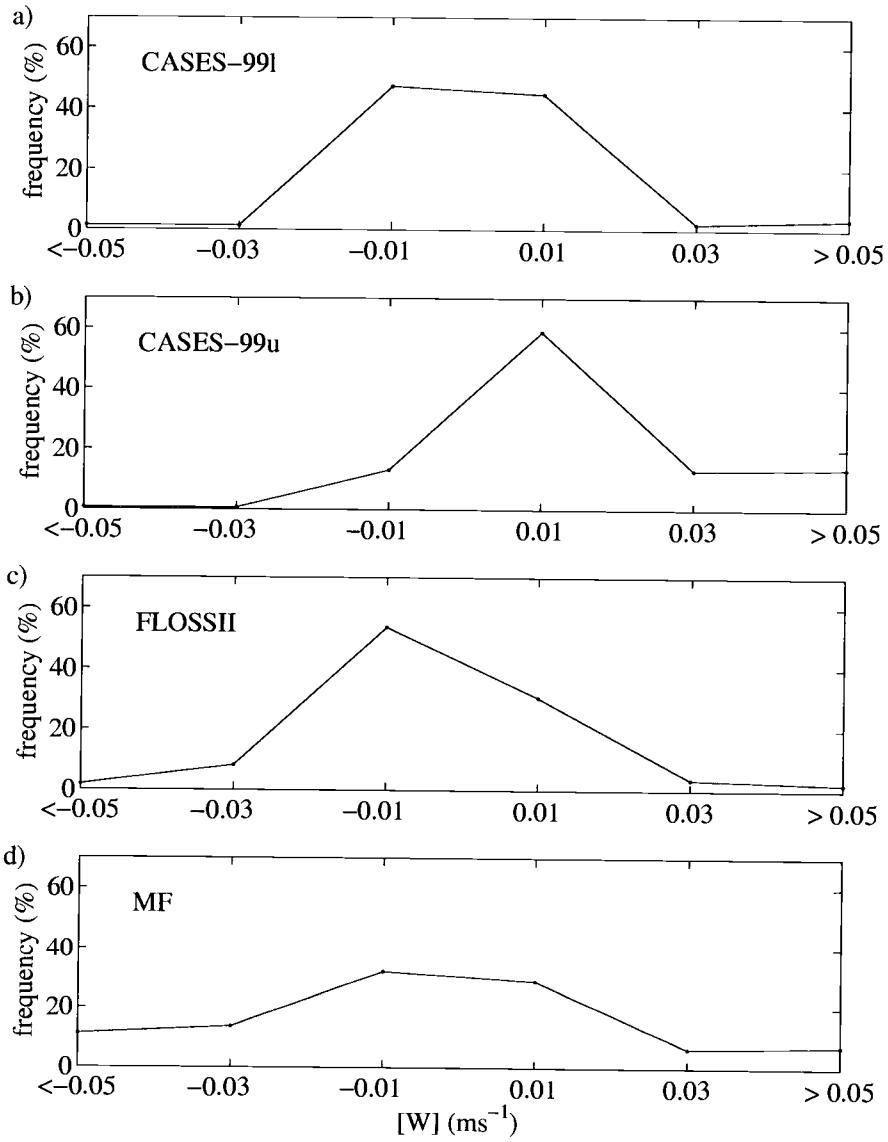

FIGURE 4.6. Frequency distribution of the magnitude of mean layer $[W]$ a) CASES-99 lower layer b) FLOSSII layer and c) Microfronts layer, estimated from the residual of the heat budget.

The mean layer wind speed is computed from sonic anemometers for CASES-99 and FLOSSII. For Microfronts, cup anemometer data are used because they are available at 4 levels instead of 2 levels for sonic anemometer data. The coordinate system is rotated every hour according to the mean wind direction so that the mean cross-wind speed vanishes. If the wind direction changes by more than 20° across the layer, no horizontal temperature gradient is calculated.

The horizontal temperature gradient required to balance the heat budget (Fig. 4.7) translates into temperature difference of a few hundredths of a degree over a horizontal distance of 100 m similar to the results of Ha and Mahrt (2002). While such small horizontal temperature gradients modify the structure of stable boundary layers, they are difficult to measure in field experiments. Difficulties arise from the random sampling error of the estimation of the horizontal temperature gradients, limitation in the accuracy of sensors and ambiguity of the standardized measurement height above vegetation of varying height (Nakamura and Mahrt, 2005). The inferred horizontal temperature gradient shows a weak tendency to increase with stability (not shown).

4.6.5. Mesoscale Heat Flux Divergence

Because the individual hourly-record average of the mesoscale heat flux is subject to large random sampling errors, such estimates are inadequate even as a rough estimate of an ensemble-averaged flux (Section 4.3). With sonic anemometer data from the 5-m level across the CASES-99 tower network, we examine the potential importance of the mesoscale heat flux for a given record by computing the spatial average of mesoscale vertical heat flux. The spatial average of the mesoscale vertical heat flux, $[w^*\theta^*]$ and the spatial average of the vertical turbulence heat flux,

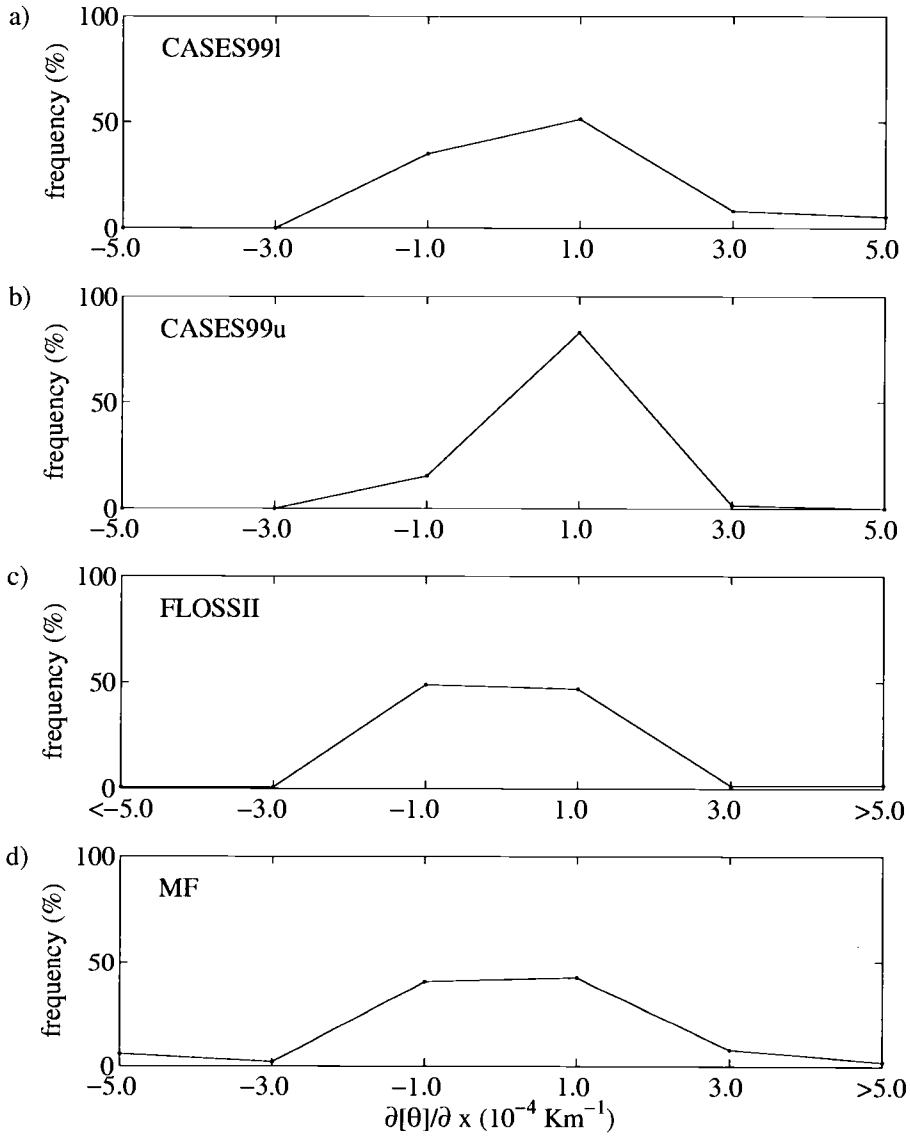

FIGURE 4.7. Frequency distribution of horizontal potential temperature gradient inferred from the residual, R (Eq. 4.10) for a) CASES-99 lower layer b) CASES-99 upper layer c) FLOSSII and d) Microfronts. Positive (negative) $\frac{\partial[\theta]}{\partial x}$ indicates cold (warm) advection.

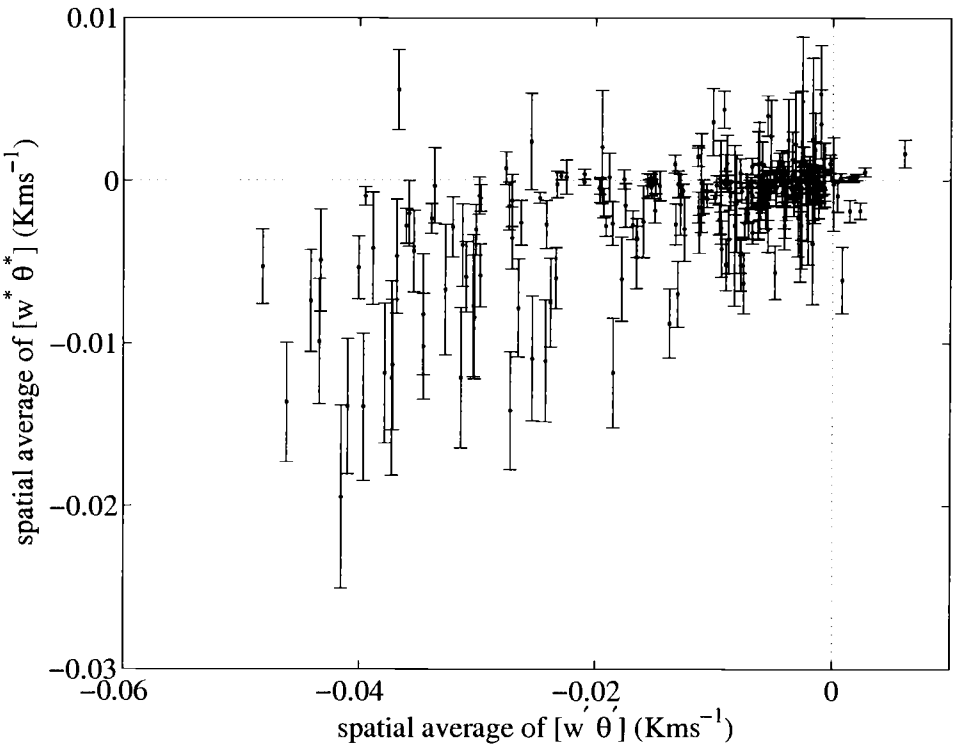

FIGURE 4.8. Comparison of the spatial average of turbulence vertical heat flux, $[w'\theta']$ and that of the mesoscale vertical heat flux, $[w^*\theta^*]$ from individual hourly records. The spatial average is performed over seven 5-m levels across the CASES-99 tower network. Error bars indicate standard errors, which are a measure of the spatial variability of mesoscale vertical heat flux over the seven towers.

$[w'\theta']$ are positively correlated (Fig. 4.8). At large negative values of the spatially-averaged $[w'\theta']$, the spatially-averaged $[w^*\theta^*]$ becomes significantly less than zero, suggesting the potential presence of systematic vertical heat transport by mesocale motions.

The potential significance of the vertical mesoscale heat flux divergence, $\int_{z_1}^{z_2} \frac{\partial[\overline{w^*\theta^*}]}{\partial x} dz$, in the heat budget is examined by averaging $[w^*\theta^*]$ from individual one hour-records over the entire field experiment (Table 4.4). The constancy of the

TABLE 4.4. Statistics of the mean layer mesoscale vertical heat flux divergence (Kh^{-1}) over the entire field experiments. The format is the same as in Table 4.2 except only the standard error is reported in the 'mean' column. The statistics are based on the same hours as those reported for the heat budget analysis in Table 4.2.

Field Experiment	$\frac{\int_{z_1}^{z_2} \frac{\partial[\overline{w^*\theta^*}]}{\partial z} dz}{z_2 - z_1}$		
	mean	abs mean	constancy
CASES-99 (lower)	-0.389 ($\pm$ 0.20)	1.7	-0.23
CASES-99 (upper)	-0.079 ($\pm$ 0.10)	0.9	-0.09
FLOSSII	-0.188 ($\pm$ 0.065)	1.3	-0.14
Microfronts	-0.021 ($\pm$ 0.54)	4.1	-0.005

mesoscale vertical heat flux divergence for the experiment is small, indicating this term is not systematic, probably due to transient mesoscale motions. Nonetheless, the experiment-averaged mesoscale vertical heat flux divergence is larger than its standard error for the CASES-99 lower layer and FLOSSII, suggesting potential importance in the heat budget, depending on the site. The experiment-averaged mesoscale vertical heat flux divergence is too small or has the wrong sign to explain the experiment-averaged residual, R, for CASES-99 upper layer and Microfronts.

The horizontal mesoscale heat flux divergence term, $\int_{z_1}^{z_2}(\frac{\partial[\overline{u^*\theta^*}]}{\partial x} + \frac{\partial[\overline{v^*\theta^*}]}{\partial y})dz$, is estimated for the 5-m level sonic anemometers within the CASES-99 tower network with the LVPF method (Section 4.6.2). The experiment-average of this term, is 0.57 and -0.15 Kh^{-1} for the 100-m and 300-m radius measurements, respectively. The sign and magnitude of the experiment-average of this term remain sensitive to the set of horizontal heat flux measurements used for calculation.

The above estimates of the mesoscale flux divergence were made with the assumption that sonic anemometers can measure the weak vertical motions. It is likely that sonic anemometers are unable to estimate weak low-frequency mesoscale vertical motions adequately for the same reasons they are unable to estimate the vertical motion due to hourly-averaged $[W]$ (Section 4.6.4). In addition, the experiment-averaged mesoscale fluxes mapped across the CASES-99 tower network do not indicate spatially coherent structure, but rather random variation from one station to the next. Since the mesoscale motions are expected to occupy larger spatial scales, this may suggest mesoscale flux estimates at individual towers are subject to errors and their numerical values should be interpreted with caution.

The present data sets are inadequate to estimate potentially important mesoscale flux divergence terms with confidence. Further investigation of these terms requires improved methodologies for estimating the vertical mesoscale wind velocity and improved strategies for assessing the ensemble-average of the mesoscale flux divergence terms in future field experiments.

4.7. Conclusions

We have analyzed data from three field programs to evaluate the one-dimensional vertically-integrated heat budget for stable nocturnal boundary layers . The observed cooling/warming (storage term) approximately balances the vertical heat flux divergence for only 0.5 % to 2.1 % of the one-hour records depending on the site and height of the layer. In the other records, the observed storage tended to be too small or even was the wrong sign to balance the vertical heat flux divergence term.

While no direct estimates of radiative flux divergence are possible from the available data, the residual of the heat budget generally substantially exceeds typical values of the radiative flux divergence reported in the literature. Based on the CASES-99 data set, the magnitude of the horizontal heat flux divergence is also too small to explain the residual. Although instrumentation errors cannot be completely eliminated as a source of the residual, our error analysis suggests that the large residual corresponds to important temperature advection or possibly mesoscale flux divergence.

Independent estimates of the vertical velocity, $[W]$ from the sonic anemometer and from mass continuity with observations of the horizontal divergence often disagreed not only in order of magnitude, but also in sign. As a result, the vertical advection cannot be estimated with confidence. As an exercise, we estimated the order of magnitude of $[W]$ required to balance the heat budget by assuming that the residual can be entirely explained by vertical advection. The inferred $[W]$ is typically on the order of a few cms^{-1}. We repeated a similar exercise to estimate the horizontal temperature gradients required for the horizontal advection term to balance the budget. The inferred horizontal temperature gradients are a few hundredths of a degree per 100 m. Measurement of such small horizontal temperature gradients requires new measurement strategies.

Our analysis of the mesoscale heat flux divergence terms suggests potential significance in the heat budget although reliable estimates of these terms require improved observational strategies.

The experiment-averaged residual of the heat budget remains larger than the typical magnitude of the radiative flux divergence and experimental errors for two of the three sites, but the experiment-averaged residual has different signs for different

experiments. This different systematic behavior of the residual between sites may suggest local effects such as advection induced by surface heterogeneity.

4.8. Appendix

4.8.1. Error Estimates of the Storage Term

In Section 4.5.1, for an individual one-hour record, the storage term was estimated by 1) fitting a linear regression line to the vertically-integrated potential temperature and 2) averaging the vertically-integrated potential temperature over 10-min windows centered at the boundaries of the record.

Comparison of the storage estimates by the two methods (Fig. 4.9) illustrates that their disagreement is approximately random except for some FLOSSII high R-square hours with large positive or negative storage values. In these hours, potential temperature increases or decreases by large amounts semi-linearly in the middle of the hours, leading to high values of R-squared values for the regression lines. Toward the beginning and end of the hours, potential temperature levels off. The large semi-linear trends in the middle of the hours set steep slopes in the regression lines. As a result, the second method estimates smaller absolute values of the storage term than the first method. This type of large systematic difference between the two storage terms is not obvious in other data sets, in which the absolute magnitude of the storage term is generally much smaller than that in FLOSSII.

A measure of the error on the estimated storage term, (Err_{stor}) is defined as

$$Err_{stor} = \frac{|\int_{z_1}^{z_2} \frac{\partial[\theta]}{\partial t} dz_{m1} - \int_{z_1}^{z_2} \frac{\partial[\theta]}{\partial t} dz_{m2}|}{2} \tag{4.16}$$

where $\int_{z_1}^{z_2} \frac{\partial[\theta]}{\partial t} dz_{m1}$ and $\int_{z_1}^{z_2} \frac{\partial[\theta]}{\partial t} dz_{m2}$ indicate the storage term estimated by the first and second methods, respectively.

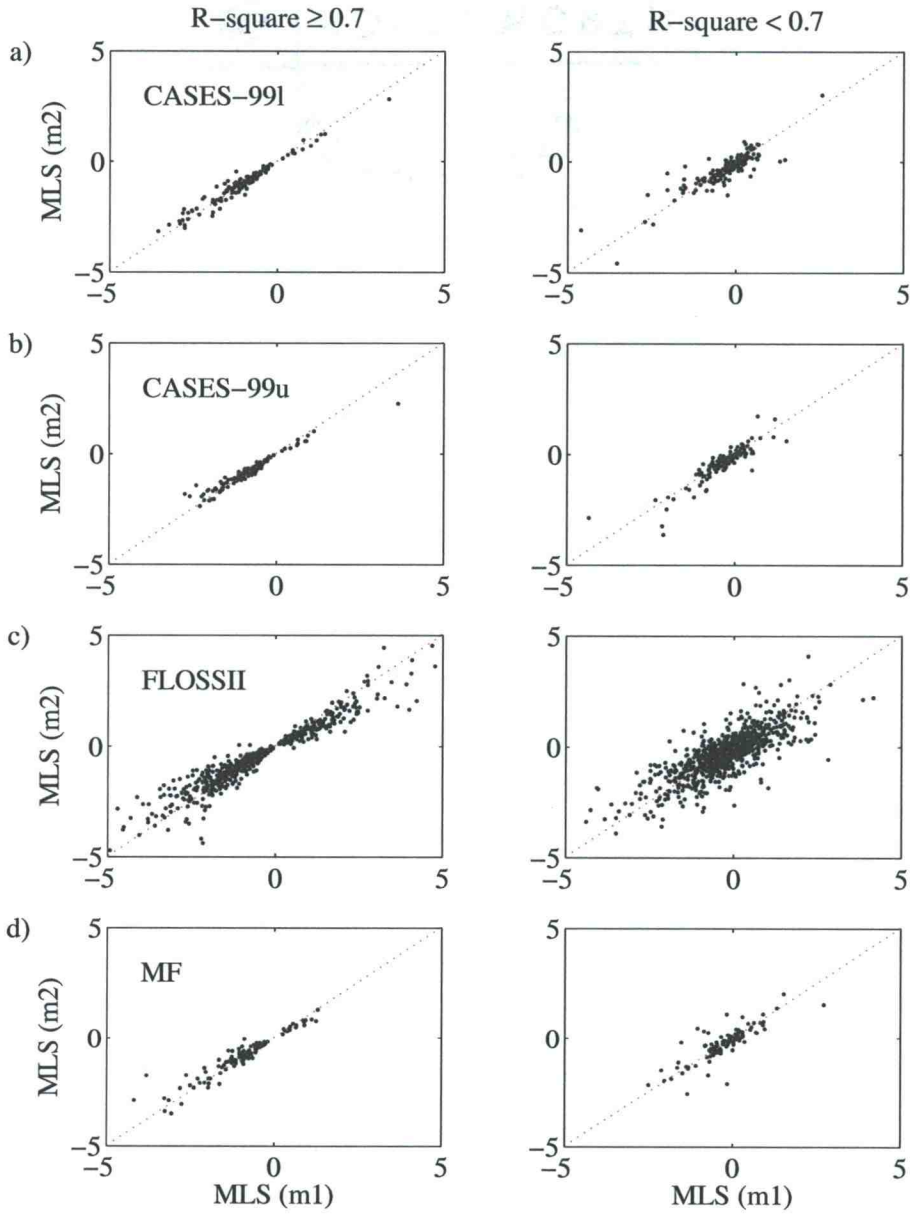

FIGURE 4.9. Comparison of the mean layer storage, $\frac{\int_{z1}^{z2} \frac{\partial \overline{\theta}}{\partial t} dz}{z_2 - z_1}$, (MLS) in Kh^{-1} estimated by two methods for a) CASES-99 lower layer b) CASES-99 upper layer c) FLOSSII and d) Microfronts. m1 (m2) indicates first (second) method. Left (Right) columns for time-series of potential temperature with high (low) R-square values for the fit of the linearly regressed line determined in method 1. Dotted lines indicate 1:1 lines.

Modulation of air temperature by mesoscale motions could also introduce random errors on the estimated storage although we are unable to evaluate the magnitude of such errors on hourly estimates of the storage. However, our analysis suggests that mesoscale motions do not cause significant random errors for the experiment-averaged storage.

4.8.2. Error Estimates of the Vertical Heat Flux Divergence Term

The error of the computed vertical heat flux divergence (Err_{hfd}) is estimated as

$$Err_{hfd} = RSE_{hfxu} + RSE_{hfxl} \tag{4.17}$$

where RSE_{hfxu} and RSE_{hfxl} indicate random sampling errors of vertical heat flux at upper and lower levels of an air layer, respectively. The random sampling errors of the vertical heat flux at an observational height can be estimated as

$$RSE_{hfx} = \frac{\sigma_{\overline{w'\theta'}}}{n^{1/2}} \tag{4.18}$$

where $\sigma_{\overline{w'\theta'}}$ and n indicate the standard deviation of sub-record vertical heat fluxes and the number of sub-record fluxes, respectively. Err_{hfd} in Eq. (4.17) is generally an overestimate of the error on the heat flux divergence estimate for most of the time since 50% of the time, the two terms on the right hand side are opposite in sign. This error estimate assumes that turbulence flux is adequately evaluated at the measurement heights.

4.8.3. Instrumentation Problems

Problems with instrumentation could also cause errors on the vertical heat flux divergence estimates. For example, use of sonic anemometers of different de-

signs at two heights may induce systematic bias on the estimated vertical heat flux divergence. In CASES-99, sonic anemometers of more than one design were deployed on the main tower for capturing the vertical profiles of turbulence fluxes. However, the composite of the vertical profile of turbulence fluxes over the entire experimental period is smooth and shows no bias at individual heights. Therefore, use of different types of sonic anemometers in CASES-99 is an unlikely source of errors on the vertical heat flux divergence estimates.

Another potential source of errors on the vertical flux divergence is path-length averaging of turbulence eddies. Sonic anemometers are unable to capture turbulence motions with length scales on the order of the path-length or smaller. Path-length averaging underestimates turbulence flux mostly in highly stable conditions and in the proximity of the ground where turbulence eddies become small. Based on the comparison of flux estimates by sonic and hot film anemometers in Skelly et al. (2002) and our field studies, we suspect that flux loss due to the path-length averaging is significant only for 1 - 2 m above the ground surface.

4.9. Acknowledgements

This work is supported by the NASA Headquarters under the Earth System Science Fellowship, the Physical Meteorology Program of the National Science Foundation under grant ATM-0107617 and the Army Research Office under grant DAAD19-02-1-0224.

4.10. References

André, J.-C., and L. Mahrt, 1982: The nocturnal surface inversion and influence of clear-air radiative cooling. *J. Atmos. Sci.*, **39**, 864-878.

Anfossi, D., P. Bacci, and A. Longhetto, 1976: Forecasting of vertical temperature profiles in the atmosphere during nocturnal radiation inversions from air tempereature trend at screen height. *Quart. J. Roy. Meteorol. Soc.*, **102**, 173-180.

Brost, R.A., and J.C. Wyngaard, 1978: A model study of the stably stratified planetary boundary layer. *J. Atmos. Sci.*, **35**, 1427-1440.

Brunt, D., 1934: *Physical and Dynamical Meteorology.* Cambridge University Press, 124-146.

Estournel, C., R. Vehil, and D. Guedalia, 1986: An observational study of radiative and turbulent cooling in the nocturnal boundary layer. *Boundary-Layer Meteorol.*, **34**, 55-62.

Garratt, J. R. and R. A. Brost, 1981: Radiative Cooling Effects Within and Above the Nocturnal Boundary Layer. *J. Atmos. Sci.*, **38**, 2730-2746.

Ha, K-J, and L. Mahrt, 2003: Radiative and turbulent fluxes in the nocturnal boundary layer. *Tellus*, **55A**, 317-327.

Howell, J.F., and J. Sun, 1999: Surface-Layer Fluxes in Stable Conditions, *Boundary-Layer Meteorol.* **90**, 495-520.

Mahrt, L., X. Lee, A. Black, H. Neumann, and R.M. Staebler, 2000: Nocturnal mixing in a forest subcanopy. *Ag and For. Meteorol.*, **101**, 67-78.

Mahrt, L., E. Moore, D. Vickers, and N.O. Jensen, 2001: Dependence of turbulent and mesoscale velocity variances on scale and stability. *J. Appl. Meteorol.*, **40**, 628-641.

Mahrt, L. and D. Vickers, 2002: Contrasting vertical structures of nocturnal boundary layers. *Boundary-Layer Meteorol.*, **105**, 351-363.

Mahrt, L., and D. Vickers, 2005: Moisture flux over snow with and without protruding vegetation. *Quart. J. Roy. Meteorol. Soc.* in press.

Nakamura, R., and L. Mahrt, 2005: Air temperature measurement errors in naturally ventilated radiation shields. *J. Atmos. Oceanic Technol.*, in press.

Nieuwstadt, F.T.M., 1980: A rate equation for the inversion height in a nocturnal boundary layer. *J. Appl. Meteorol.*, **19**, 1445-1447.

Poulos, G.S., W. Blumen, D.C. Fritts, J.K. Lundquist, J. Sun, S.P. Burns, C. Nappo, R. Banta, R. Newsom, J. Cuxart, E. Terradellas, B. Balsley, and M. Jensen, 2002: CASES-99: A Comprehensive Investigation of the Stable Nocturnal Boundary Layer, *Bull. Amer. Meteor. Soc.*, **83**, 555-581

Skelly, B.T., D.R. Miller, T.H. Meyer, 2002: Triple-hot-film anemometer performance in CASES-99 and a comparison with sonic anemometer measurements, *Boundary-Layer Meteorol.*, **105**, 275304.

Sun, J., S.P. Burns, A.C. Delany, S.P. Oncley, T.W. Horst, and D.H. Lenschow, 2003: Heat balance in the nocturnal boundary layer during CASES-99. *J. Appl. Meteorol.*, **42**, 1649-1666.

Vickers, D., and L. Mahrt, 1997: Quality control and flux sampling problems for tower and aircraft data, *J. Atmos. Oceanic Technol.*, **14**, 512-526.

Vickers, D., and L. Mahrt, 2003: The cospectral gap and turbulent flux calculations, *J. Atmos. Oceanic Technol.*, **20**, 660–672.

Vickers, D., and L. Mahrt, 2005: A solution for flux contamination by mesoscale motions with very weak turbulence, submitted to *Boundary-Layer Meteorol.*.

Wyngaard, J.C., 1975: Modeling the planetary boundary layer extension to the stable case. *Boundary-Layer Meteorol.* **9**, 441-460.

Zamora, R.J., M.A. Shaprio, C.A. Doswell III, 1987: The diagnosis of upper tropospheric divergence and ageostrophic wind using profiler wind observations. *Mon. Wea. Rev.*, **115**, 871-884.

5. CONCLUSIONS

The research in this dissertation has revealed previously-unknown physical characteristics of the flow field in stable nocturnal boundary layers (SNBLs). At the same time, it has identified problems with the strategies or methodologies in observing the SNBL.

In the first manuscript, we have identified characteristics of intermittent turbulence patches observed within a network of towers of CASES-99. We have defined intermittent turbulence using the variance of the vertical wind velocity and its spectral information. While the disturbance causing intermittent turbulence may be large, the spatial extent of individual intermittent turbulence patches is generally smaller than the tower network of 300 m radius horizontally. The gradient Richardson number analysis, cross-correlation analysis and visual inspection of raw data suggest intermittent turbulence patches evolve and decay rapidly as they are advected between two towers separated by 100 m or more. As a result, tracing a turbulence patch across the tower network becomes tenuous, and neither a single tower nor towers separated by 100 m or more are sufficient for studying the evolution and decay of intermittent turbulence patches. A denser tower network than the one in CASES-99 is desirable for future investigations of the evolution of individual intermittent turbulence patches.

In the second manuscript, we have evaluated and contrasted magnitudes of systematic errors on air temperature estimates due to 1) ambiguity of the standardized measurement height above vegetation and 2) radiative forcing on a temperature sensor-shield system. This study evaluated a sensor-shield system commonly used for observational studies of atmospheric boundary layers. Regarding the first source of errors, use of the zero-displacement height was suggested for standardizing the

measurement height above vegetation. An empirical formula was developed for correcting air temperature errors due to the second source. For stable nocturnal conditions, air temperature errors due to the first source could reach a few tenths of a degree, larger than a typical value due to the second source. An error of a few tenths of a degree on air temperature measurements can cause a significant error in the horizontal advection computed over small distances. The spatial variability of air temperature is difficult to estimate especially over vegetated surfaces in the SNBL. An improved methodology for estimating the zero-plane displacement height is necessary.

In the final manuscript, we have examined the vertically-integrated sensible heat budget in SNBLs using data sets from three field experiments. It has been traditionally assumed that the structure of the SNBL can be described with a one-dimensional approach. This assumption has dictated the design of field experiments, which for example, have not allowed adequate advection estimates, as in our data sets. The analysis shows that the heat budget cannot be generally balanced by the storage, vertical heat flux divergence and vertical radiative flux divergence only. An extensive error analysis suggests that instrumental and sampling errors cannot explain the large imbalance, implying the significance of advection of temperature in the heat budget and possibly mesoscale flux divergence. This finding calls for the necessity of a future observational network adequately designed for directly estimating advection of temperature.

In the present dissertation, advection of turbulence and temperature has been found more significant in SNBLs than previously thought. We have also illustrated that estimates of advection can be challenging due to various sources of errors. Nonetheless, for better understanding of SNBLs, the present work suggests that we need improved observational strategies or methodologies for directly evalu-

ating advection even over surfaces which are considered to homogeneous for daytime convective conditions.

BIBLIOGRAPHY

Abarbanel, H.D.I., D.D. Holm, J.E. Marsden, and T. Ratiu, 1984: Richardson number criterion for the nonlinear stability of three-dimensional stratified flow, *Phys. Rev. Lett.* **52**, 2352-2355.

André, J.-C., and L. Mahrt, 1982: The nocturnal surface inversion and influence of clear-air radiative cooling. *J. Atmos. Sci.*, **39**, 864-878.

Anderson, S.P., and M.F. Baumgartner, 1998: Radiative heating errors in naturally ventilated air temperature measurements made from buoys. *J. Atmos. Oceanic Technol.* **15**, 157-173.

Anfossi, D., P. Bacci, and A. Longhetto, 1976: Forecasting of vertical temperature profiles in the atmosphere during nocturnal radiation inversions from air tempereature trend at screen height. *Quart. J. Roy. Meteorol. Soc.*, **102**, 173-180.

Arck, M., and D. Scherer, 2001: A physically based method for correcting temperature data measured by naturally ventilated sensors over snow. *J. Glaciol.* **47**, 665 - 670.

Atlas, D., J.I. Metcalf, J.H. Richter, and E.E. Gossard, 1970: The birth of "CAT" and microscale turbulence, *J. Atmos. Sci.* **27**, 903-913.

Blackwelder, R.F., and R.E. Kaplan, 1976: On the wall structure of the turbulent boundary layer, *J. Fluid Mech.* **76**, 89-12.

Blumen, W., 1984: An observational study of instability and turbulence in nighttime drainage winds, *Boundary-Layer Meteorol.* **28**, 245-269.

Brost, R.A., and J.C. Wyngaard, 1978: A model study of the stably stratified planetary boundary layer. *J. Atmos. Sci.*, **35**, 1427-1440.

Brunt, D., 1934: *Physical and Dynamical Meteorology.* Cambridge University Press, 124-146.

Brutsaert, W., 1982: *Evaporation into the atmosphere.* Kluwer Academic Publishers, 299pp.

Campbell, G.C., 1969: Measurement of air temperature fluctuations with thermocouples. *ECOM-5273*, Atmospheric Sciences Laboratory, White Sands Missile Range, New Mexico, 10 pp.

Chelton, D.B., 1983: Effects of sampling errors in statistical estimation. *Deep-Sea Res.*, **30**, 1083-1103.

Coulter, R.L., 1990: A case study of turbulence in the stable nocturnal boundary layer, *Boundary-Layer Meteorol.* **52**, 75-91.

Coulter, R.L., and J.C. Doran, 2002: Spatial and temporal occurrence of intermittent turbulence during CASES-99, *Boundary-Layer Meteorol.* **105**, 329-349.

De Bruin, H.A.R., and C. J. Moore, 1985: Zero-plane displacement and roughness length for tall vegetation, derived from a simple mass conservation hypothesis *Boundary-Layer Meteorol.***31**, 39-49.

Drazin, P.G., 1977: On the instability of internal gravity wave, *Proc. R. Soc. Lond. A.* **356**, 411-432.

Edson, J.B., and C.W. Fairall, 1998: Similarity relationship in the marine atmospheric surface layer for terms in the TKE and scalar variance budgets, *J. Atmos. Sci.* **55**, 2311-2328.

Erell, E., V. Leal, E. Maldonado, 2004: Measurement of air temperature in the presence of a large radiant flux: an assessment of passively ventilated thermometer screens. *Boundary-Layer Meteorol.*, **114**, 205-231.

Estournel, C., R. Vehil, and D. Guedalia, 1986: An observational study of radiative and turbulent cooling in the nocturnal boundary layer. *Boundary-Layer Meteorol.*, **34**, 55-62.

Finnigan, J.J., 1988: Kinetic energy transfer between internal gravity waves and turbulence, *J. Atmos. Sci.* **45**, 486-505.

Finnigan, J.J., and F. Einaudi, 1981: The interaction between an internal gravity wave and the planetary boundary layer. part II: effect of the wave on the turbulence structure, *Quart. J. Roy. Meteorol. Soc.* **107**, 807-832.

Fuchs, M., and C.B. Tanner, 1965: Radiation shields for air temperature thermometers. *J. Appl. Meteor.* **4**, 544-547.

Garratt, J. R. and R. A. Brost, 1981: Radiative Cooling Effects Within and Above the Nocturnal Boundary Layer. *J. Atmos. Sci.*, **38**, 2730-2746.

Gill, G.C., 1979: Development of a small rugged radiation shield for air temperature measurements on drifting buoys. NOAA Rep. Contract 01-7-038-827, National Data Buoy Center, Stennis Space Center, MS, 23 pp.

Grisogono, B., 1994: A curvature effect on the critical Richardson number, *Croatian Meteorol. J.* **29**, 43-46.

Ha, K.-J., and L. Mahrt, 2003: Radiative and turbulent fluxes in the nocturnal boundary layer. *Tellus* **55A**, 317-327.

Howell, J.F., and L. Mahrt, 1997: Multiresolution flux decomposition, *Boundary-Layer Meteorol.* **83**, 117-137.

Howell, J.F., and J. Sun, 1999: Surface-layer fluxes in stable conditions, *Boundary-Layer Meteorol.* **90**, 495-520.

Howell, J.R., 1982: *A catalog of radiation configuration factors.* McGraw-Hill Book Company, 243pp.

Hubbard, K.G., X. Lin, and E. A. Walter-Shea, 2001: The effectiveness of the ASOS, MMTS, Gill and CRS air temperature radiation shields. *J. Atmos. Oceanic Technol.* **18**, 851-864.

Incropera, F.P., and D.P. De Witt, 1990: *Fundamentals of heat and mass transfer.* (third edition) John Wiley & Sons, 919pp.

Jones, H.G., 1992: *Plants and microclimate.*, second edition, Cambridge University Press, 299pp.

Kaimal, J.C., and J.J. Finnigan, 1994: *Atmospheric boundary layer flows.* Oxford University Press. 289pp.

Katul, G.G., J. Albertson, M. Parlange, C-R Chu, and H. Stricker, 1994: Conditional sampling, bursting, and the intermittent structure of sensible heat flux, *J. Geophys. Res.* **99**, 22869-22876.

Kim, J., and L. Mahrt, 1992: Simple formulation of turbulent mixing in the stable free atmosphere and nocturnal boundary layer, *Tellus* **44A**, 381-394.

Kondo, J., O. Kanechika, and N. Yasuda, 1978: Heat and momentum transfers under strong stability in the atmospheric surface layer, *J. Atmos. Sci.* **35**, 1012 - 1021.

Kunkel, K.E., and D.L. Walters, 1982: Intermittent turbulence in measurements of the temperature structure parameter under very stable conditions, *Boundary-Layer Meteorol.* **22**, 49 - 60.

Lilly, D.K., 1983: Stratified turbulence and the mesoscale variability of the atmosphere, *J. Atmos. Sci.* **40**, 749 - 761.

Lin, X., K.G. Hubbard, and G.E. Meyer, 2001a: Airflow characteristics of commonly used temperature radiation shields. *J. Atmos. Oceanic Technol.* **18**, 329-339.

Lin, X., G. Hubbard, and E.A. Walter-Shea, 2001b: Radiation loading model for evaluating air temperature errors with a non-aspirated radiation shield. *Transactions of the ASAE.* **44**, 1229-1306.

Lyons, R., H.A. Panofsky, and S. Wollaston, 1964: The critical Richardson number and its implications for forecast problems, *J. Appl. Meteorol.* **3**, 136 - 142.

Mahrt, L., 1985: Vertical structure and surbulence in the very stable boundary layer, *J. Atmos. Sci.* **42**, 2333-2349.

Mahrt, L., 1989: Intermittency of atmospheric turbulence, *J. Atmos. Sci.* **46**, 79-95.

Mahrt, L., and S. Larsen, 1982: Small scale drainage front, *Tellus* **34**, 579-587.

Mahrt, L., X. Lee, A. Black, H. Neumann, and R.M. Staebler, 2000: Nocturnal mixing in a forest subcanopy. *Ag and For. Meteorol.*, **101**, 67-78.

Mahrt, L., E. Moore, D. Vickers, and N.O. Jensen, 2001: Dependence of turbulent and mesoscale velocity variances on scale and stability. *J. Appl. Meteorol.*, **40**, 628-641.

Mahrt, L., and D. Vickers, 2002: Contrasting vertical structures of nocturnal boundary layers, *Boundary-Layer Meteorol.* **105**, 351-363.

Mahrt, L., and D. Vickers, 2005: Moisture flux over snow with and without protruding vegetation. *Quart. J. Roy. Meteorol. Soc.* in press.

Majda, A.J., and M.G. Shefter, 1998: Elementary stratified flows with instability at large Richardson number, *J. Fluid Mech.* **376**, 319-350.

Monteith, J.L., and M. Unsworth, 1990: *Principles of environmental physics.* (second edition) Edward Arnold. 291pp.

Nakamura, R., and L. Mahrt, 2005: Air temperature measurement errors in naturally ventilated radiation shields. *J. Atmos. Oceanic Technol.*, in press.

Nappo, C.J., 1991: Sporadic breakdowns of stability in the PBL over simple and complex terrain, *Boundary-Layer Meteorol.* **54**, 69-87.

Nappo, C.J., 2002: *An introduction to atmospheric gravity waves* Academic Press. pp. 276.

Nappo, C.J., and P-E Johansson, 1999: Summary of the Lövånger international workshop on turbulence and diffusion in the stable planetary boundary layer, *Boundary-Layer Meteorol.*, **90**, 345-374.

Narasimha, R., and S.V. Kailas, 1990: Turbulent bursts in the atmosphere, *Atmos. Environ.* **24A**, 1635-1645.

Nieuwstadt, F.T.M., 1980: A rate equation for the inversion height in a nocturnal boundary layer. *J. Appl. Meteorol.*, **19**, 1445-1447.

Parlange, M.B., W. Brutsaert, 1989: Regional roughness of the Landes Forest and surface and shear stress under neutral conditions, *Boundary-Layer Meteorol.*, **48**, 69-80.

Poulos, G.S., W. Blumen, D.C. Fritts, J.K. Lundquist, J. Sun, S.P. Burns, C. Nappo, R. Banta, R. Newsom, J. Cuxart, E. Terradellas, B. Balsley, and M. Jensen, 2002: CASES-99: a comprehensive investigation of the stable nocturnal boundary layer, *Bull. Amer. Meteor. Soc.*, **83**, 555-581

Raupach, M.R., 1994: Simplified expressions for vegetation roughness length and zero-plane displacement as functions of canopy height and area index. *Boundary-Layer Meteorol.*, **71**, 211-216.

Richardson, S.J., F.V. Brock, S.R. Semmer and C. Jirak, 1999: Minimizing errors associated with multiplate radiation shields. *J. Atmos. Oceanic Technol.* **16**, 1862-1872.

Riley, J.J., R.W. Metcalfe, and M.A. Weissman, 1981: Direct numerical simulations of homogeneous turbulence in density-stratified fluids, In *Nonlinear Properties of Internal Waves.*, West, B.J., Editor, American Institute of Physics, New York, 79-112.

Skelly, B.T., D.R. Miller, T.H. Meyer, 2002: Triple-hot-film anemometer performance in CASES-99 and a comparison with sonic anemometer measurements, *Boundary-Layer Meteorol.*, **105**, 275304.

Stull, R. B, 1988: *An introduction to boundary layer meteorology.* Kluwer Academic Publishers, 666pp.

Sun, J., S.P. Burns, A.C. Delany, S.P. Oncley, T.W. Horst, and D.H. Lenschow, 2003: Heat balance in the nocturnal boundary layer during CASES-99. *J. Appl. Meteorol.*, **42**, 1649-1666.

Sun, J., S.P. Burns, D.H. Lenschow, R. Banta, R. Newsom, R. Coulter, S. Frasier, T. Ince, C. Nappo, J. Cuxart, W. Blumen, X. Lee, and X-Z Hu, 2002: Intermittent turbulence associated with a density current passage in the stable boundary layer, *Boundary-Layer Meteorol.* **105**, 199-219.

Tanner, B.D., E. Swiatek, C. Maughan, 1996: Field comparisons of naturally ventilated and aspirated radiation shields for weather station air temperature measurements. Preprints, *22nd Conf. On Agricultural and Forest Meteorology.* Atlanta, GA, Amer. Meteor. Soc., 227 230.

Tanner, C.B., 1979: Temperature: critique I. *controlled environment guidelines for plant research.*, T.W. Tibbitts and T.T. Kozlowski, Eds., Academic Press, 117 130.

Thorpe, S.A., 1973: Turbulence in stably stratified fluids: a review of laboratory experiments, *Boundary-Layer Meteorol.* **5**, 95-119.

Vickers, D., and L. Mahrt, 1997: Quality control and flux sampling problems for tower and aircraft data, *J. Atmos. Oceanic Technol.*, **14**, 512-526.

Vickers, D., and L. Mahrt, 2003: The cospectral gap and turbulent flux calculations, *J. Atmos. Oceanic Technol.* **20**, 660-672.

Vickers,D., and L. Mahrt, 2004: Evaluating formulations of stable boundary-layer height. *J. Appl. Meteor.*, **43**, 1736-1749.

Vickers, D., and L. Mahrt, 2005: A solution for flux contamination by mesoscale motions with very weak turbulence, submitted to *Boundary-Layer Meteorol.*.

Whiteman, C.D., J.M. Hubbe, and W.J. Shaw, 2000: Evaluation of an inexpensive temperature data logger for meteorological applications. *J. Atmos. Oceanic Technol.* **17**, 77-81.

Woods, J.D., 1969: On Richardson's number as a criterion for laminar-turbulent-laminar transition in the ocean and atmosphere', *Radio Science* **12**, 1289 - 1298.

Wyngaard, J.C., 1975: Modeling the planetary boundary layer extension to the stable case. *Boundary-Layer Meteorol.* **9**, 441-460.